Universidade Federal do Rio Grande – FURG

Instituto de Oceanografia

Programa de Pós-Graduação em Oceanologia

A circulação de revolvimento meridional do Atlântico em 8,2 ka AP: Forças e respostas

Wilton Aguiar Carvalho Silva Filho

Orientador: *Prof. Dr.* Mauricio Magalhães Mata

Universidade Federal do Rio Grande (FURG), Brasil.

Coorientadora: *Prof. Dr.* Ilana Wainer

Universidade de São Paulo (USP), Brasil.

Rio Grande, RS, Brazil

Maio 2021

Universidade Federal do Rio Grande – FURG

Instituto de Oceanografia

Programa de Pós-Graduação em Oceanologia

A circulação de revolvimento meridional do Atlântico em 8,2 ka AP: Forças e respostas

Wilton Aguiar Carvalho Silva Filho

Tese apresentada ao Programa de Pós-Graduação em Oceanologia, como parte dos requisitos para a obtenção do Título de Doutor.

Orientador: *Prof. Dr.* Mauricio Magalhaes Mata
Universidade Federal do Rio Grande (FURG), Brasil.

Coorientadora: *Prof. Dr.* Ilana Wainer
Universidade de São Paulo (USP), Brasil.

Rio Grande, RS, Brazil

Maio 2021

A circulação de revolvimento meridional do Atlântico em 8,2 ka AP: Forças e respostas

Tese apresentada ao Programa de Pós-Graduação em Oceanologia, como parte dos requisitos para a obtenção do Título de Doutor

por

Wilton Aguiar Carvalho Silva Filho

Rio Grande, RS, Brazil

Maio 2021

Aguiar Carvalho Silva Filho, Wilton

A circulação de revolvimento meridional do Atlântico em 8,2 ka AP: Forças e respostas./ Aguiar Carvalho Silva Filho, Wilton. – Rio Grande: FURG, 2021.

Número de páginas p.139

Tese (Doutorado) – Universidade Federal do Rio Grande-FURG. Doutorado em Oceanologia.

1. 8,2 ka AP. 2. América do Sul. 3. Atlântico Sul. 3. AMOC.

UNIVERSIDADE FEDERAL DO RIO GRANDE - FURG
IO – INSTITUTO DE OCEANOGRAFIA
PROGRAMA DE PÓS-GRADUAÇÃ0 EM OCEANOLOGIA
E-mail: ccpofqg@furg.br – home-page: www.ppgo.furg.br

ATA ESPECIAL DE DEFESA DE TESE DE DOUTORADO – 04/2021

Às 13h e 30min. do dia 28 de maio do ano de dois mil e vinte e um, por videoconferência, reuniu-se a Comissão Examinadora da Tese de **DOUTORADO** intitulada "**A circulação de revolvimento meridional do Atlântico em 8,2 ka AP: Forças e respostas**", do Acad. **Wilton Aguiar Carvalho Silva Filho**. A Comissão Examinadora foi composta pelos seguintes membros: Prof. Dr. Mauricio M. Mata – Orientador (IO/FURG), Profa. Dra. Ilana Wainer – Coorientadora (USP), Prof. Dr. Rodrigo Kerr (IO/FURG), Profa. Dra. Juliana Marini Marson (*University of Manitoba*/CANADÁ) e Prof. Dr. Álvaro Montenegro (*Ohio State University*/EUA). Dando início à reunião, o Orientador e Presidente da sessão, Prof. Dr. Mauricio M. Mata, agradeceu a presença de todos e fez a apresentação da Comissão Examinadora. Logo após esclareceu que o Candidato teria um tempo de 45 a 60 min para explanação do tema, e cada membro da Comissão Examinadora, um tempo máximo de 30 min para perguntas. A seguir, passou à palavra ao Candidato que apresentou o tema e respondeu às perguntas formuladas. Após ampla explanação, a Comissão Examinadora reuniu-se em reservado para discussão do conceito a ser atribuído ao Candidato. Foi estabelecido que as sugestões de todos os membros da Comissão Examinadora, que seguem em pareceres em anexo, foram aceitas pelo Orientador/Candidato para incorporação na versão final da Tese. Finalmente, a Comissão Examinadora considerou o candidato APROVADO, por unanimidade. Nada mais havendo a tratar, foi lavrada a presente ATA que após lida e aprovada, será assinada pela Comissão Examinadora, pelo Candidato e pelo Coordenador do Programa de Pós-Graduação em Oceanologia.

Prof. Dr. Mauricio M. Mata
Presidente

Profa. Dra. Ilana Wainer

Prof. Dr. Rodrigo Kerr

Profa. Dra. Juliana Marini Marson

Prof. Dr. Álvaro Montenegro

Prof. Dr. Rodrigo Kerr
Coordenador PPGO

Acad. Wilton Aguiar Carvalho Silva Filho

When problems overwhelm us and sadness smothers us, where do we find the will and the courage to continue? Well, the answer may come in the caring voice of a friend, a chance encounter with a book or from a personal faith.

For Janet help came from her faith but it also came from a ***squirrel.***

Shortly after her divorce Janet lost her father. Then she lost her job, she had mounting money problems. But Janet not only survived. She worked her way out of despondency and now she says life is good again. How could this happen? She told me that late one autumn day when she was at her lowest, she watched a squirrel storing up nuts for the winter. One at a time he would take them to the nest. And she thought if that squirrel can take care of himself with the harsh winter coming on, so can I. Once I broke my problems into small pieces I was able to carry them, just like those acorns, one at a time.

Little Acorns. Escrito por Jack White e Mort Crim. Interpretado por *The White Stripes*

"Gray squirrels may devour many acorns, but by storing and ***failing*** *to recover up to* ***74 percent*** *of them, these rodents aid regeneration and dispersal of oaks"*

Steele, M. and P. Smallwood. 1994. What are squirrels hiding? Natural History, 10:40-46.

"'Mistakes is the word you're too embarrassed to use. You ought not to be. You're a product of a trillion of them. Evolution forged the entirety of sentient of life on this planet using one tool – the mistake…
… it also means you must indulge me the occasional mistake."

Dr. Robert Ford. Personagem fictício interpretado por Anthony Hopkins na série *Westworld*

Índice

Agradecimentos

Agradeço a minha mãe. Mulher guerreira que lutou para nos fornecer uma boa educação. Que trabalhou durante feriados, carnaval, *operação chuva*, e sempre que podia para nos fornecer o que era necessário para viver. Que me ensinou a batalhar pelo que eu quero. Que me ensinou a persistência e a resistência, e que acreditou nos meus sonhos, ainda que eu mesmo não acreditasse neles. Mãe, se hoje eu faço ciência, é porque mesmo sem diploma você me ensinou a ser cientista desde criança. Saiba que esta tese é tão minha quanto sua.

Agradeço imensamente também ao meu orientador, Mauricio! Obrigado por investir academicamente e financeiramente em mim e por estar sempre disposto a resolver dúvidas, a discutir idéias! Obrigado por lançar nossa pesquisa e a mim para o mundo. Dizem que um bom caminho no doutorado depende fortemente do ajuste entre orientador e orientando - e eu vejo agora que isto é 100% verdade! Sou imensamente agradecido pela sua orientação!

Vó, eu nunca vou esquecer como você caiu de joelhos quando descobriu que eu entrei na universidade publica! Isto por que vi naquele momento que esta conquista não era somente minha, mas nossa também! Agradeço por todo investimento feito em mim. Agradeço todo o cuidado em casa, e os cachorros-quentes esperando por mim quando eu chegava da minha jornada diária de graduação e trabalho. Agradeço por todo amor e cuidado!

Evilásio, obrigado por ser um padrasto e pai para mim, e por investir em mim. Você me apoiou em momentos extremamente difíceis da minha vida (talvez sem mesmo saber), e me aceitou antes mesmo de eu me aceitar. Lembra quem comprou o vôo para Rio Grande, para eu começar o mestrado? Você! Se estou aqui terminando o doutorado hoje é porque você acreditou e investiu em mim, sem pedir nada em troca. Se a política brasileira tivesse 10% de "Evilásios" não estaríamos no caos pandêmico que estamos hoje.

Mady, obrigado por ser um espelho que sigo desde criança. Sua inteligência, sagacidade é uma fonte de inspiração pra mim, e sempre foi.
Pai, hoje eu sei o que é ser um homem negro na sociedade brasileira. Sei as dificuldades que você passou, e que você entregou o máximo de si para nossa criação. Ainda que não sejamos tão próximos hoje em dia, quero que saibas que te amo (e sei que é recíproco).

Pipo, você apareceu na minha vida no momento perfeito. Obrigado por suportar minhas crises de ansiedade, e por me elevar. Nós trazemos à tona o melhor do outro, e nos puxamos para sermos mais fortes cada dia. Mal posso esperar pelo resto das nossas vidas juntos <3.

Bel, se tem alguém que devo agradecer, esta é você. Obrigado por me estimular a tentar o mestrado, e me alojar quando cheguei a Rio Grande. Obrigado pelos 13 anos de amizade, e pelos 2 anos morando juntos. Obrigado pelas incontáveis horas de fofoca com lanches. Obrigado por ser uma inspiração acadêmica e pessoal pra mim.

Megeras (a.k.a Rods, Mabia e Tuxo e Bel), vocês me acolheram e passaram por todo o meu processo de crescimento. Os acarajés na Dinha durante as nossas seções de *shade* (... ou catarse?) fazem parte de quem eu sou, e me ajudaram a aguentar as pressões do doutorado! Obrigado por suportarem minhas reclamações e sempre elevarem meu espírito. Mal posso esperar para a pandemia terminar para a gente se esbaldar em acarajé e calabresa frita com aipim no Rio Vermelho!

Álvaro e Eunice, obrigado pela cooperação científica, pelas aulas e ensinamentos sobre modelagem e pelas conversas na cozinha (do *Geography Department* e na de vocês também, :D). Sua influência foi importantíssima no curso do meu doutorado. Você e a Eunice me acolheram na sua casa mesmo sem me conhecer, e sou extremamente grato por isto!

Katrin, thank you for trusting me and my science, and for the several email exchanges. Working alongside you and Álvaro changed the course of my doctorate, and I am incredibly grateful for that. I hope we continue doing science together in the future!

Ilana, agradeco imensamente pela co-orientação, pelos recursos, pelas discussões e ensinamentos científicos. Minha jornada na modelagem não seria mesma sem você. Obrigado por me ensinar e por estar sempre disponível para discussões de resultados! Obrigado por sempre me desafiar a ir além.

Luciana, você esteve presente em toda minha jornada do doutorado também. Da proposta de pesquisa, passando pelas reuniões e análises científicas, e até mesmo nos resultados finais. Existem pessoas que chegam no nosso caminho do doutordo para nos inspirar, e você foi uma dessas para mim. Obrigado por tudo!

Iole, não é todo dia que a gente encontra alguém tão parecido. Não sei se é por causa das conjunções planetárias do dia 8 de Maio, ou pela marca da constelação de Touro, mas uma coisa é fato. Tu sempre vais ser minha irmã de outra mãe, e alguém especial pra mim!

Camila, Mariah e Nina. Ter vocês na minha jornada de mestrado e doutorado foi imensamente prazeroso! Sei que dificilmente dividirei sala com um grupo tão harmonioso e de bom astral quanto vocês. Espero daqui a uns anos encontrar vocês todas juntas, pra fazer uma aula de zumba e montar uns quebra cabeças.

Ju, obrigado pelas incontáveis *mock interviews* e seções de conferência. É louco que nós nos mantivemos amigos por tanto tempo, mesmo você estando a *n* fusos horários de distância. Obrigado por sempre me encorajar a me preparar para entrevistas de posdoc mesmo quando eu estava exausto. Obrigado por ajudar a edit down meus slides de entrevista caóticos! Danke, dass du mein Freund bist!

Agradeço a minha família também. Todos vocês contribuíram para uma partezinha de quem sou, de onde estou, e da ciência que faço. Obrigado por me apoiar e me ajudar!

Agradeço também aos membros da banca de avaliação, Prof. Dr. Rodrigo Kerr e Prof. Dra. Juliana Marson, pela disposição em avaliar e corrigir esta tese, e por contribuírem para a minha jornada científica.

Mauriuvs, obrigado por me manter vivo nos momentos *off-conference* na Califa! Mal posso esperar para juntarmos o mesmo grupo para o próximo Ocean Science em San Diego (sabe-se lá quando!).

Agradeço imensamente ao LEOC (ao laboratório e aos membros). A estrutura física, computacional, pessoal e de relacionamento lá foi uma peça chave para um caminho mais agradável no meu doutorado!

Agradeço imensamente também aos professores do PPGO que tive contato! Vocês me provaram que aulas não são um protocolo, mas uma facilitador do caminho da ciência - e me provaram ao darem aula com amor. Obrigado por isto!

Luiza and Catherine, thank you so much for being my friends and support network in Columbus! I will NEVER forget our brunches, deep philosophical discussions, halloween costumes and travels. Soon enough I will see you both in person again - I know it.

Maite, te conheço a tão pouco tempo, mas com essa quarentena parece 10 anos de amizade! Obrigado pela companhia, e por suportar viver comigo e Ricardo no final do Doutorado- eu sei que não é pra qualquer um! Obrigado por sempre me cobrar pra fazer as coisas o quanto antes quando eu tentava procrastinar. Mal posso esperar para te ver no futuro como a grande profissional que serás!

Catherine (Fitzpatrick), in that day that I walked pass you and Fiamma coming from the beach, I would have never imagined that I just found a inspiring workmate and a lifelong friend! Our foodie nights, wino behaviour and True Detective sections made the cold winters something to look forward! Thank you so much for being part of my academic and personal journey my friend, and I can't wait to see you again soon!

Agradeço ao meu filho, Salém (=^.^=)! Obrigado por me confortar deitando no meu colo quando eu estava exausto de tanto revisar texto, e por me acompanhar desde que cheguei em Rio Grande. A você prometo um fornecimento eterno de Whiskas Sachê!

Lista de Figuras

Lista de Tabelas

Lista de Acrônimos e Abreviações

A

AABW – Água de Fundo Antártica (*Antarctic Bottom Water*)

AMOC- Célula de Revolvimento Meridional do Atlântico (*Atlantic Meridional Overtuning Ciculation*)

AP – Antes do Presente

C

CCSM3 – *Community Climate System Model Version 3*

E

ENSO – El Niño/Oscilação Sul (*El Niño/ Southern Oscillation*)

G

GIS – Plataforma de Gelo da Groenlandia (*Greenland Ice Sheet*)

K

Ka – Kiloanos, i.e. 1000 anos

L

LGM – Último Máximo Glacial (*Last Glacial Maximum*)

LIS – Plataforma de Gelo Laurentide (*Laurentide Ice Sheet*)

M

MLD – Anomalia na profundidade da camada de mistura (*Mixed Layer Depth anomaly*)

MOM – Modelo Oceâmico Modular (*Modular Ocean Model*)

N

NADW – Água Profunda do Atlântico Norte (*North Atlantic Deep Water*)

NCEP – *National Center for Environmental Prediction*

R

RMSE – Erro Médio Quadrático (*Root Mean Square Error*)

RCP8.5 – Projeção de emissões de dióxido de carbono baseados no cenário mais intenso de emissões (*Representative concentration Pathway 8.5*)

S

SACZ – Zona de Convergência do Atlântico Sul (*South Atlantic Convergence Zone).*

SAMS – Sistema de Monções da América do Sul (*South American Monsoon System).*

SASD – Dipolo Subtropical do Atlântico Sul (*South Atlantic Subtropical Dipole).*

SLR – Metros equivalentes ao aumento do nível do mar (*Sea Level Rise equivalent*)

SST – Temperatura da Superfície do Mar (*Sea Surface Temperature*)

T

TraCE21ka – Simulação Transiente do Clima dos últimos 21 mil anos (*Simulation of the Transient Climate of the Last 21,000 Years).*

U

UVic – Modelo do sistema terrestre da Universidade de Victoria (*University of Victoria Earth System Model).*

Abstract

The northern hemisphere experienced an abrupt cold event ~8200 years ago (the 8.2 ka event) that was triggered by the release of meltwater into the Labrador Sea, resulting in a weakening of the Atlantic poleward oceanic heat transport. Although this event has been considered a possible analogue for future ocean circulation changes due to the projected Greenland Ice Sheet (GIS) melting, large uncertainties in the amount and rate of freshwater released during the 8.2 ka event make such a comparison difficult. In this thesis, sea surface temperatures and oxygen isotope ratios from 28 isotope-enabled model simulations were compared with 35 paleoproxy records to constrain the meltwater released during the 8.2 ka event. The results suggest that a meltwater flux of 7.5 m in sea level rise equivalent (SLR) released over a thousand years best reproduces the 8.2 ka proxy anomalies. Our meltwater flux estimate is of the same order of magnitude as future GIS melting rates under the high CO_2 emission scenario RCP8.5 (~7.2 m in SLR). Considering this similarity, we further analyzed one of the largest uncertainties in the climate expression of the 8.2 ka event, i.e. the response of the South American climate to the weaker Atlantic Ocean Meridional Overturning Circulation (AMOC). We find that the reconstructed sea surface temperatures and precipitation indicate an AMOC-driven strengthening of the South American Monsoon System (SAMS). Therefore, these results support that a strengthening of the SAMS could happen as a response to a weaker AMOC under the RCP8.5 scenario.

Resumo

O Hemisfério Norte passou por um evento extremo de resfriamento 8200 anos antes do presente, chamado de evento de 8,2 ka. Este evento foi iniciado pela liberação de grandes quantidades de água de degelo no mar do Labrador, diminuindo assim a convecção profunda no Atlântico Norte e o transporte meridional de calor do Atlântico. Ainda que o evento e 8,2 ka AP seja comumente associado como um análogo para a resposta climática do potencial futuro derretimento do manto de gelo da Groenlândia, incertezas relativas à magnitude dos fluxos de água de degelo e a expressão destes no Hemisfério Sul dificultam comparações mais diretas com projeções climáticas futuras. Nesta tese, campos e séries temporais de temperatura da superfície do mar (SST) e de razão isotópica de oxigênio ($\delta^{18}O$) derivadas de 28 simulações do sistema terrestre foram comparadas com 35 reconstruções paleoclimáticas das mesmas variáveis a fim de se estimar os fluxos de água doce responsáveis por iniciar o evento de 8,2 ka. As simulações feitas neste trabalho apontam que um fluxo de água equivalente a 7,5 m de aumento do nível do mar liberado durante 1000 anos (9 ka – 8 ka) representa melhor as anomalias nas reconstruções de SST e $\delta^{18}O$, sendo potencialmente o fluxo de água doce gerador do 8,2 ka. A estimativa feita nesta tese para o fluxo de água doce gerador do 8,2 ka é da mesma ordem de magnitude que os fluxos de degelo estimados para o potencial descongelamento do manto de degelo da Groenlândia no cenário de altas emissões de CO_2 (7,2 m em SLR, RCP8.5). Considerando esta similaridade entre os dois cenários de descarga de água doce, foi efetuada uma análise adicional das anomalias climáticas do 8,2 ka no Atlântico Sul e América do Sul baseando-se em reconstruções de SST e precipitação para o Hemisfério Sul. As reconstruções apontam que a desaceleração na Circulação de Revolvimento Meridional do Atlântico durante o 8,2 ka aumentou a evaporação sobre o Atlântico Tropical, intensificando o Sistema de Monções da América do Sul (SAMS). A similaridade das descargas de água doce durante o 8,2 ka e no RCP8.5, quando interpretada juntamente com o sinal de intensificação do SAMS durante o evento passado, aponta que uma intensificação do SAMS é uma possível consequência do potencial futuro derretimento da Groenlândia.

Prefácio

A Paleoceanografia, ao aproximar a visão dinâmica e mecanística da oceanografia com a clássica lógica geológica de entendimento do passado para compreensão do futuro, fornece um campo de estudo único. Isto porque esta junção cria uma área de estudo intrinsecamente interdisciplinar e com ampla possibilidade de teste de hipótese (devido às grandes incertezas do passado climático do planeta). Ademais, estudos paleoceanográficos têm a capacidade de criar conhecimento sobre o sistema terrestre que é largamente aplicável para previsões climáticas futuras, tornando esta área da ciência não somente útil, mas também fascinante!

Meu fascínio com estudos paleoceanográficos se iniciou no meu primeiro contato com estes na disciplina de Oceanos e Clima cursada durante meu mestrado. Este interesse então cresceu mais ainda ao entender que a Circulação Meridional de Revolvimento do Atlântico (AMOC) é uma peça chave para a compreensão de eventos

paleoclimáticos, motivando-me então a entrar no doutorado para entender como eventos passados de circulação da AMOC alteraram o clima global.

O leque de possibilidades de tópicos para estudo dentro da paleoceanografia é enorme, mas um destes tópicos se mostrou particularmente interessante: O evento de 8,2 ka AP. Isto porque a hipótese deste evento ser uma análogo para desaceleração futura da AMOC devido ao potencial derretimento do manto de gelo da Groenlândia faz dele um caso clássico de *estudo do passado para compreensão do futuro.* Aliado a isto, uma robusta e recente base de reconstruções climáticas e simulações deste evento me foram fornecidas no início do meu doutorado.

A análise destas reconstruções e simulações demonstrou que o 8,2 ka AP pode sim ser pensando como um análogo para a resposta da AMOC ao futuro derretimento do manto de gelo da Groenlândia. Ademais as anomalias climáticas do 8,2 ka AP podem ser utilizadas como ponto de exploração para sinais climáticos futuros, como é o caso da intensificação do Sistema de Monções da América do Sul, encontrado nesta tese.

Capítulo I: Introdução

A evolução climática do Quaternário (últimos 2,6 Milhões de anos) é marcada por intensos ciclos glaciais e interglaciais, gerados por oscilações em parâmetros orbitais terrestres e instabilidades de componentes internas do clima [Hays et al., 1976]. Os mecanismos geradores dessas oscilações têm o oceano como peça-chave para sua modulação, especialmente durante a transição do último máximo glacial (LGM: ~21 ka antes do presente - AP) para o interglacial presente (~ 12 ka AP, Holoceno).

Durante a transição do LGM para o Holoceno, o hemisfério norte recebia maiores quantidades de radiação solar incidente (Fig 1a), causando um gradual aquecimento na sua superfície [Kaufman, 2004]. Esse lento aumento na radiação solar incidente no hemisfério norte gerou uma transição de um clima glacial para o atual interglacial (*i.e.* Holoceno). No entanto, essa transição para o Holoceno foi interrompida por eventos rápidos e extremos de resfriamento. Este é o caso dos eventos *Younger Dryas* e *Oldest Dryas* [Clark et al., 2002, 2012], que trouxeram o planeta para condições similares às glaciais durante poucos séculos (Fig. 1c), causando um rápido resfriamento de até 10^{o}C sobre a Groenlândia [Alley, 2000].

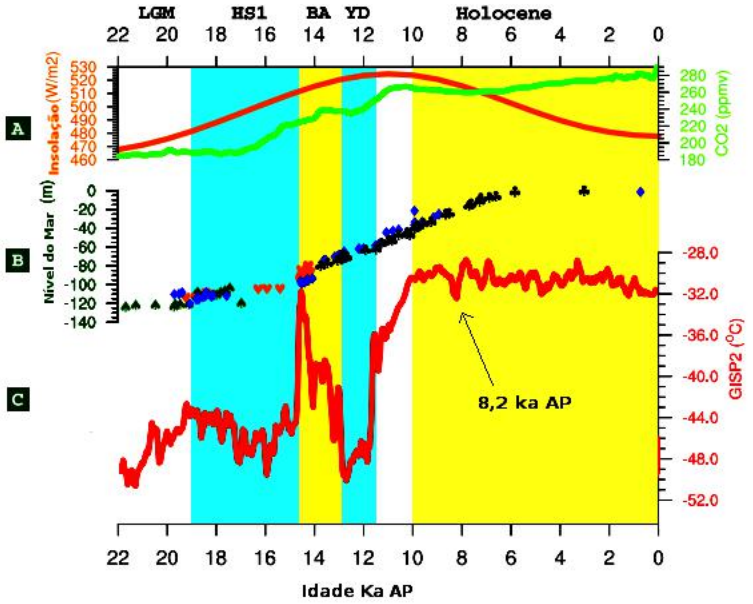

Figura I.1- Transição do UMG para o Holoceno, através de registros sedimentares. Em (A), a linha laranja corresponde à radiação solar incidente sobre 60ºN, reconstruída para o verão Boreal (Junho), e a linha verde corresponde à concentração de CO_2 na atmosfera, obtida através de testemunhos de gelo da Groenlândia. (B) Reconstrução do nível relativo do mar em Barbados. (C) Corresponde à paleotemperatura reconstruída para a Groenlândia com base no testemunho sedimentar *Greenland Ice Sheet Project 2* - GISP2. LGM corresponde ao Último Máximo Glacial, HS1 ao evento Heinrich 1, BA ao *Bolling-Allerod* e YD ao *Younger Dryas*. Adaptado de: He [2011].

Apesar da maior parte dos eventos frios desde o LGM ocorrerem antes do Holoceno, um desses eventos interrompeu o período de clima estável do presente interglacial: o evento de resfriamento de 8200 anos antes do presente (8.2 ka AP, Fig 1c/2a). Embora os eventos *Younger Dryas* e *Older Dryas* sejam mais largamente estudados e tenham produzido um maior resfriamento no hemisfério norte, o evento de 8,2 ka tem sido foco da comunidade científica por ocorrer durante o presente interglacial, portanto apresentando condições climáticas similares às presentes (i.e., clima estável interglacial). Esta similaridade de condições climáticas frequentemente leva o 8,2 ka AP a ser pensado como um possível análogo para mudanças na circulação oceânica, devido ao potencial futuro derretimento do manto de gelo da Groenlândia (GIS - [Schmidt and LeGrande, 2005])

A cadeia de eventos responsável por iniciar o 8,2 ka se iniciou ainda na transição do LGM para o Holoceno, quando parte da América do Norte era recoberta pelo manto de gelo *Laurentide* (LIS). Com o aumento da radiação solar incidente durante o Holoceno inferior (11,7 ka AP - 8,2 ka AP) [Kaufman, 2004], o LIS começou a derreter e sofrer *calving*[1] [Clarke et al., 2003], gerando diversos processos de liberação de água doce para o mar de Labrador. O primeiro processo de descarga de água doce no mar de Labrador, próximo ao 8,2 ka AP, deve-se ao próprio derretimento do LIS (1, na Fig I.2). Parte da água de degelo do LIS foi liberada diretamente sobre a baía de Hudson e regiões costeiras do Atlântico Norte, eventualmente chegando ao mar de Labrador [Carlson et al., 2008].

O segundo processo de diminuição da salinidade no mar de Labrador deve-se ao colapso do lago Agassiz-Ojibway (2, na Fig I.2). Parte das águas do derretimento do LIS fluíram para dentro do continente, se acumulando sobre baixos relevos. Juntamente com o escoamento devido à precipitação, estas águas formaram o lago pró-glacial Agassiz-Ojibway há aproximadamente 8,5 ka AP [Barber et al., 1999; Klitgaard-Kristensen et al., 1998], limitado ao norte pelos reminiscentes do LIS (Figura 2b). Neste lago, o derretimento do LIS devido às condições quentes do Holoceno causou um contínuo aumento da pressão da água sobre a plataforma de gelo. Após aproximadamente 50 anos da formação do lago, o LIS sucumbiu à pressão exercida pela água, colapsando violentamente e liberando abruptamente seu conteúdo de água doce no Atlântico Norte [Clarke et al., 2003], via Mar do Labrador [Barber et al., 1999].

[1] *Calving* = Separação de um pedaço de gelo a partir de uma geleira flutuante, frente de gelo ou Iceberg

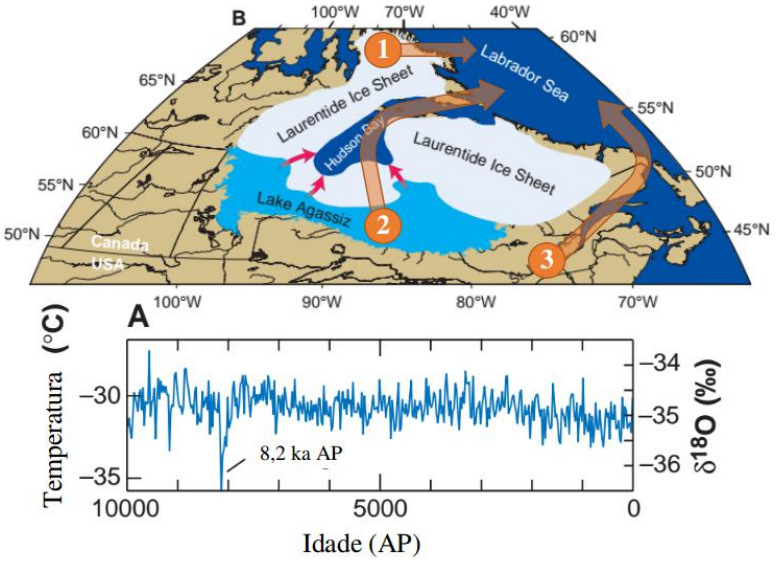

Figura I.2 - Forçantes e registro isotópico do 8,2 ka AP. Em A, tem-se a evolução da razão isotópica de oxigênio e a temperatura média na Groenlândia durante o Holoceno, baseados no registro de Dansgaard et al., [1993] do *Greenland Ice Sheet Project*. Em B estão esquematizados a localização do Lago Agassiz-Ojibway e os três possíveis processos de adição de água doce no mar de Labrador durante o início do Holoceno. Estes processos são (1) o derretimento direto do LIS, (2) o colapso do lago Agassiz-Ojibway e (3) a transposição da descarga continental do rio *St. Lawrence*. Adaptado de Clarke et al. [2003].

Não obstante, o derretimento e a diminuição da massa do LIS permitiu uma diminuição da pressão do gelo sobre o continente [Peltier, 2004], consequentemente permitindo um ajuste isostático do relevo. Este ajuste glacio-isostático, juntamente com mudanças no regime de precipitação durante o Holoceno inferior, eventualmente foi responsável por transpor a desembocadura do rio *St. Lawrence* para o Mar de Labrador (3, na Fig I.2) por um período de 100 há 300 anos [Carlson et al., 2009]. Estes processos de derretimento (1), colapso lacustres (2) e transposição (3) então liberaram uma imensa quantidade de água doce sobre o Mar de Labrador, afetando a Circulação de Revolvimento Meridional do Atlântico (AMOC).

A AMOC pode ser definida como a circulação de larga escala do Atlântico integrada zonalmente [Broecker et al., 1992; Broecker, 1998] e pode ser dividida numa

estrutura de duas células de circulação: uma superior, dirigida pelo transporte de *Ekman* e pela convecção profunda no Hemisfério Norte, e uma célula inferior dirigida principalmente pela convecção profunda ao redor do oceano Austral [Stommel, 1961; Visbeck, 2007]. A célula superior da AMOC se inicia com o fluxo de águas tropicais quentes sobre a termoclina em direção ao Atlântico Norte e Ártico (Fig I.3A). Ao chegarem em altas latitudes do Atlântico Norte, estas águas quentes e salinas de superfície perdem calor para a atmosfera fria polar (Fig I.3B), resfriando, perdendo flutuabilidade e assim gerando convecção profunda [Talley, 2013]. Este processo ocorre principalmente nos Mares de Labrador [Hein et al., 2002], da Escócia e Islândia [García-Ibáñez et al., 2015] e é responsável pela formação da Água Profunda do Atlântico Norte (NADW). O aporte de *momentum* no oceano profundo gerado pela convecção profunda e formação da NADW alimenta toda célula superior da AMOC, que então transporta a NADW em direção ao hemisfério sul. Estas águas então ressurgem ao sul da frente polar, divergindo em superfície, com parte do seu volume fechando a célula superior de revolvimento e outra parte se encaminhando para as proximidades do continente Antártico para alimentar a célula inferior [Talley, 2013].

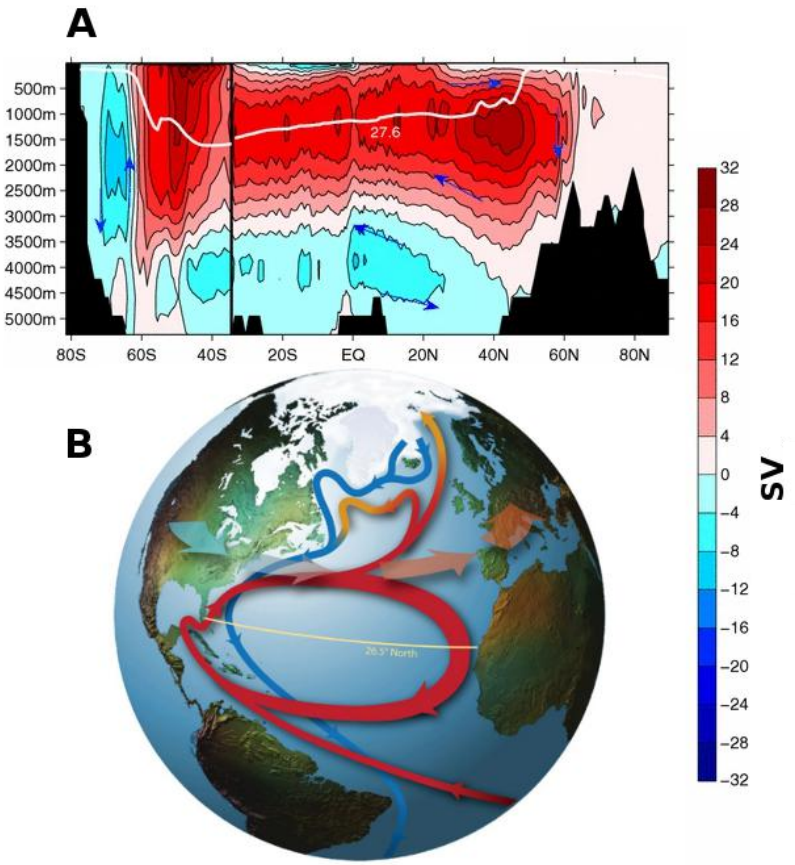

Figura I.3 Circulação da AMOC. Em (A), os contornos ao norte de 35ºS representam a função de corrente da AMOC integrada zonalmente no Atlântico, em Sverdrups (Sv= 10^6 m^3 s^{-1}), enquanto os contornos ao sul de 35ºS representam a função de corrente para o revolvimento global. Valores positivos (negativos) de função de corrente denotam circulação horária (anti-horária). Contornos de função de corrente obtidos de Zhang et al., [2017]. O desenho em (B) representa a circulação da célula superior da AMOC, no ramo superficial (vermelho) e profundo (azul), obtido de Srokosz & Bryden [2015].

A circulação *interstadial*[2] da AMOC, durante o Holoceno, tem como efeito principal a transferência de calor de baixas latitudes subtropicais para altas latitudes subpolares, garantindo invernos com temperaturas mais amenas no Hemisfério Norte [Broecker, 1998]. Consequentemente, uma desaceleração do fluxo da AMOC diminui o transporte meridional de calor para o Hemisfério Norte, estabelecendo condições frias e secas localmente [Broecker et al., 1992], enquanto o oposto ocorre quando a

[2] *Interstidial* = Estágio de circulação intensa da AMOC que ocorre durante períodos interglaciais.

flutuabilidade das águas do Atlântico Norte diminui (Fig I.4). Tal desaceleração pode ocorrer devido aos fluxos de calor ou degelo em latitudes subpolares do Atlântico Norte, aumentando a estratificação vertical e diminuindo a convecção profunda local que alimenta o ramo superior da AMOC [Bond et al., 1993]. Este mecanismo de transporte de calor dependente da convecção profunda é um dos principais causadores do da reversão de anomalias de temperatura entre o Hemisfério Sul e Norte em resposta a alterações da AMOC, padrão este chamado de *gangorra de calor bipolar* [Stocker and Johnsen, 2003] e é um dos principais mecanismos utilizados para explicar as anomalias climáticas dos eventos *Younger Dryas* e 8,2 ka AP.

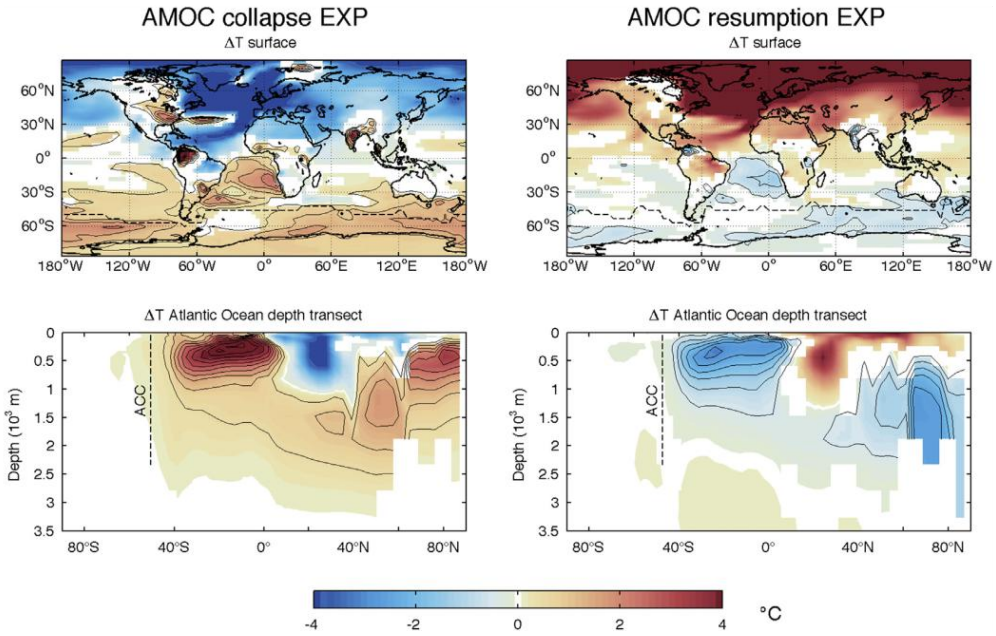

Figura I.4 Anomalias de temperatura atmosférica na superfície (acima) e em médias zonais para o Atlântico (abaixo) em fases de desaceleração (esquerda) e aceleração da AMOC (direita). Gráficos derivados de experimentos de colapso (esquerda) e aceleração (direita) da AMOC, simulados com o *Community Climate System Model version 3*. Imagem obtida de Pedro et al. [2018]

Apesar de eventos de descarga de água doce no Atlântico Norte serem utilizados para explicar a desaceleração da AMOC no passado e o estabelecimento de eventos frios no Hemisfério Norte, ainda existem incertezas substanciais quanto à

magnitude das forçantes e à expressão espacial destes eventos frios, especialmente para o 8,2 ka AP. Especificamente, a diversidade de processos de liberação de água doce no Hemisfério Norte durante o Holoceno inferior (Fig. I.2, processos 1-3), dificulta a quantificação do volume de água doce responsável por desacelerar a AMOC e iniciar o 8,2 ka AP [Clarke et al., 2003, Carlson et al., 2008]. Ainda que as primeiras evidências apontassem o colapso do lago Agassiz-Ojibway como o fluxo causador do 8,2 ka [Barber et al., 1999], recentes evidências sedimentares [Carlson et al., 2008] e de modelagem numérica [Wagner et al., 2013; Morrill et al., 2014] apontam que os processos de transposição de descarga (3) e derretimento (1) tiveram importante papel em estabelecer a duração e intensidade do evento 8,2 ka. Adicionalmente, estimativas da magnitude e duração dos fluxos de água doce devido aos processos de transposição do rio *St. Lawrence* (3) e derretimento do LIS (3) variam grandemente, somando aportes totais de água doce que variam entre 1,5 m [Li et al., 2012] e 9 m [Carlson et al., 2008] em metros equivalentes de elevação do nível do mar (SLR). Considerando que o 8,2 ka é o único evento de oscilação da AMOC no Holoceno, saber qual o volume de água doce responsável por desestabilizar a AMOC se torna extremamente importante para o estudo da estabilidade da AMOC no presente interglacial e, principalmente, no Antropoceno[3].

Uma segunda fonte de incerteza do 8,2 ka é a assinatura espacial deste evento. Testemunhos de gelo da Groenlândia mostram o estabelecimento de condições secas e um resfriamento de até 6°C devido ao evento de 8,2 ka AP [Alley et al., 1997; Thomas et al., 2007]. Reconstruções climáticas baseadas em registros de pólen e diatomáceas

[3] Antropoceno: Era geológica atual, i.e. período em que as atividades humanas exercem influência primária sobre o clima e meio ambiente. Traduzido do dicionário *Oxford*.

mostram uma diminuição de 1° - 2°C na temperatura superficial atmosférica sobre a Europa [Seppä & Birks, 2001; Seppä & Poska, 2004; Wagner et al., 2013], Canadá [Yu & Eicher, 1998] e nos Estados Unidos [Dean & Karlén, 1973; Kneller & Peteet, 1999; Dean & Schwalb, 2000]. No entanto, poucas reconstruções climáticas com *proxies* coletados no hemisfério sul focam em analisar os efeitos do evento 8,2 ka AP neste hemisfério [Arz et al., 2001; Ljung et al., 2008]. Ainda assim, uma análise *multiproxy* de efeitos do 8,2 ka AP encontrou valores similares de taxa de detecção de sinais climáticos do 8,2 ka ao norte e ao sul do trópico de câncer e conclui que a falta de evidência de alterações climáticas no hemisfério sul deve-se à baixa densidade de *proxies* climáticos nesta área [Morrill and Jacobsen, 2005]. Talvez a maior evidência de alterações climáticas no hemisfério sul esteja no registro sedimentar das Ilhas Cariaco – Venezuela [Hughen et al., 1996]. Análises das concentrações de titânio em testemunhos sedimentares da bacia das ilhas Cariaco registram um rápido aumento na velocidade dos ventos alísios relacionado com a migração para sul da Zona de Convergência Intertropical (ITCZ) [Hughen et al., 1996]. As migrações da ITCZ têm o potencial de alterar os gradientes meridionais de precipitação e de ventos, consequentemente afetando diretamente a transferência de *momentum* para os oceanos e o clima do hemisfério sul. Portanto, os registros das ilhas Cariaco apontam para a possibilidade de que os efeitos da diminuição da AMOC em 8,2 ka AP tenham se estendido para o hemisfério sul. Ainda assim, não há uma ideia precisa da comunidade científica de quais foram os efeitos de larga escala do 8,2 ka no Atlântico Sul e na América do Sul.

Responder qual a magnitude das forçantes de água doce e quais as alterações climáticas no hemisfério sul durante o evento de 8,2 ka AP se torna ainda mais importante atualmente devido às previsões de derretimento do GIS e desaceleração da

AMOC para os próximos séculos [Bintanja and Selten, 2014; Davies et al., 2014]. De fato, modelagens do derretimento do GIS em diferentes cenários de emissão de dióxido de carbono demonstram que os fluxos de água doce do GIS para o Atlântico Norte podem aumentar em mais de 20 vezes em relação ao valor atual, alcançando aportes de água doce acima de 7 m em SLR no presente milênio [Aschwanden et al., 2019]. Adicionalmente, o resfriamento persistente nas águas do Atlântico Norte de 1970 até os dias de hoje já é reportado como uma das consequências da possível diminuição da AMOC e de seus fluxos de calor na superfície [Rahmstorf et al., 2015; Sévellec et al., 2017]. Considerando que o contexto interglacial atual de desaceleração da AMOC é similar ao do evento de 8,2 ka AP, decifrar qual o processo causador e as consequências da desaceleração da AMOC no hemisfério sul durante o 8,2 ka se torna ainda mais importante pois ajuda a compreender futuras alterações climáticas devido à possível desaceleração da AMOC durante o século 21.

Capítulo II: Hipótese

Considerando a desaceleração da AMOC durante o 8,2 ka AP, a similaridade das condições climáticas do início do Holoceno com o clima presente e as incertezas na expressão do 8,2 ka AP no hemisfério sul, a seguinte hipótese foi testada:

Hipótese: a desaceleração da AMOC durante o 8,2 ka foi causada por descargas de água doce similares àquelas projetadas para o derretimento do manto de gelo da Groenlândia no presente milênio, causando alterações climáticas de larga escala no Atlântico Sul e na América do Sul.

Capítulo III: Objetivos

III.1 - Objetivo geral

Estimar a magnitude da descarga de água doce geradora do evento de 8,2 ka AP e as consequências deste evento no Atlântico Sul e América do Sul.

III.2 - Objetivos específicos:

- Estimar magnitude e duração dos fluxos de água doce liberados no mar de Labrador e responsáveis por gerar o 8,2 ka AP.
- Avaliar se a magnitude dos fluxos de água doce geradores do 8,2 ka AP são comparáveis às estimativas futuras de descarga de água de degelo do manto de gelo da Groenlândia.
- Investigar como a desaceleração da AMOC durante o 8,2 ka AP influenciou os padrões climáticos e oceanográficos no Atlântico Sul e na América do Sul.

Capítulo IV: Conceitos e Teorias

Diversos conceitos teóricos ligados às análises paleoceanográficas e aos mecanismos de interação entre oceano e atmosfera são explorados nesta tese. Este capítulo tem como objetivo esclarecer esses conceitos, fornecendo ao leitor a base teórica necessária para o entendimento dos resultados da tese. Na seção IV.1 serão explicados os conceitos de *paleoproxies*, seus métodos de obtenção e os mecanismos pelos quais eles registram alterações climáticas. Na seção IV.2 será definido o Sistema de Monções da América do Sul (SAMS). Finalmente, na seção IV.3 será definido o conceito de Dipolo Subtropical do Atlântico Sul (SASD) e sua relação com o SAMS.

IV.1 Paleoproxies, cronologia e funções de transferência.

A análise de eventos climáticos dos últimos milênios difere das análises oceanográficas do presente, principalmente pela impossibilidade de medição direta de variáveis clássicas utilizadas para entender o clima (e.g. temperatura, precipitação, salinidade). No entanto, reconstruções paleoclimáticas de traçadores oceânicos são possíveis através de análises geoquímicas de tecidos duros de fósseis de organismos

aquáticos. Tais reconstruções são comumente chamadas na comunidade paleoceanográfica de *proxies (ou paleoproxies)*. Um exemplo clássico de *paleoproxies* são as reconstruções da temperatura da superfície do mar (SST) baseadas na razão isotópica de oxigênio ou na razão Magnésio/Cálcio em depósitos de conchas de foraminíferos planctônicos [Cronin, 2009].

A variável biogeoquímica mais utilizada para reconstruções de parâmetros físicos oceânicos é a razão entre os isótopos de oxigênio estável de ^{18}O e ^{16}O ($\delta^{18}O$), que pode ser calculada de acordo com a seguinte equação:

$$\delta^{18}O = \left(\frac{\left(\frac{^{18}O}{^{16}O}\right)_{Amostra}}{\left(\frac{^{18}O}{^{16}O}\right)_{Padrão}} - 1 \right) 1000\ [‰] \qquad \textbf{Eq.IV.1}$$

onde a razão padrão entre os isótopos $\left(\frac{^{18}O}{^{16}O}\right)_{Padrão} \approx 0.0020052\ ‰$ é constante e baseada no padrão médio da água do mar de Vienna (*Vienna Standard Mean Ocean Water* -VSMOW) [Gonfiantini, 1984].

A viabilidade da utilização da $\delta^{18}O$ para o cálculo de variáveis oceanográficas deve-se, principalmente, aos seus padrões de fracionamento dentro do sistema terrestre, através da molécula de água. Dentro do sistema terrestre, o isótopo de oxigênio mais leve é mais abundante do que o mais pesado (composição média terrestre: $^{16}O \cong 99{,}8\%$; $^{18}O \cong 0{,}2\%$) e, portanto, a razão isotópica é reportada em partes por mil [Epstein & Mayeda, 1953]. Como átomos de oxigênio se associam com o hidrogênio, formando a água, estes isótopos se tornam abundantes tanto nos organismos vivos como na atmosfera, criosfera e oceanos, portanto, interagindo com o clima e registrando alterações neste [Craig, 1961]. Além da sua abundância, os isótopos de oxigênio são

capazes de registrar diferentes variáveis climáticas, como por exemplo alterações no nível do mar, temperatura no momento de calcificação e salinidade [e.g Zeebe,1999].

A capacidade da $\delta^{18}O$ de registrar alterações no nível do mar está ligada à maior retenção dos isótopos leves em mantos de gelo polares. Devido ao maior peso molecular do isótopo ^{18}O e menor energia vibracional (menor peso do ^{16}O, maior energia vibracional), este isótopo tende a precipitar mais facilmente (^{16}O a evaporar mais facilmente), fazendo com que processos de evaporação e precipitação concentrem ^{18}O nas águas e ^{16}O nas massas de ar (Fig IV.1), processo este chamado de fracionamento isotópico [Epstein & Mayeda, 1953]. Visto que a circulação atmosférica transporta massas de ar em direção às regiões polares, à medida em que estas massas de ar se movem para altas latitudes isótopos pesados precipitam primeira e progressivamente, reduzindo sua concentração em relação aos isótopos leves, diminuindo a $\delta^{18}O$ (Fig IV.2). Assim, ao chegar nas regiões polares, o vapor d'água presente nas massas de ar está enriquecido em ^{16}O. Deste modo, a maior abundância do ^{16}O nas massas de ar polares e o fracionamento adicional devido à precipitação local faz com que as águas presentes nos mantos de gelo polares tenham uma baixa razão isotópica.

Durante períodos glaciais os mantos de gelo polares expandem estocando ^{16}O e assim aumentando a razão ^{18}O:^{16}O no oceano [Jouzel et al., 1994]. Esta maior abundância de ^{18}O no oceano favorece então a calcificação do carbonato de cálcio ($CaCO_3$) com altas $\delta^{18}O$. Assim, altas $\delta^{18}O$ em organismos calcificadores, e baixas $\delta^{18}O$ em registros de testemunho de gelo são associados a períodos frios e glaciais e com menores níveis eustáticos do mar. O oposto ocorre durante eventos quentes do hemisfério norte e períodos interglaciais, devido ao derretimento dos mantos de gelo polares e consequente aporte de ^{16}O no oceano [e.g., Jouzel et al., 1994]. Usando-se esta

relação entre a dinâmica das $\delta^{18}O$ nos mantos de gelo e as razões medidas em conchas de organismos calcificadores, é possível então estimar variações no nível do mar.

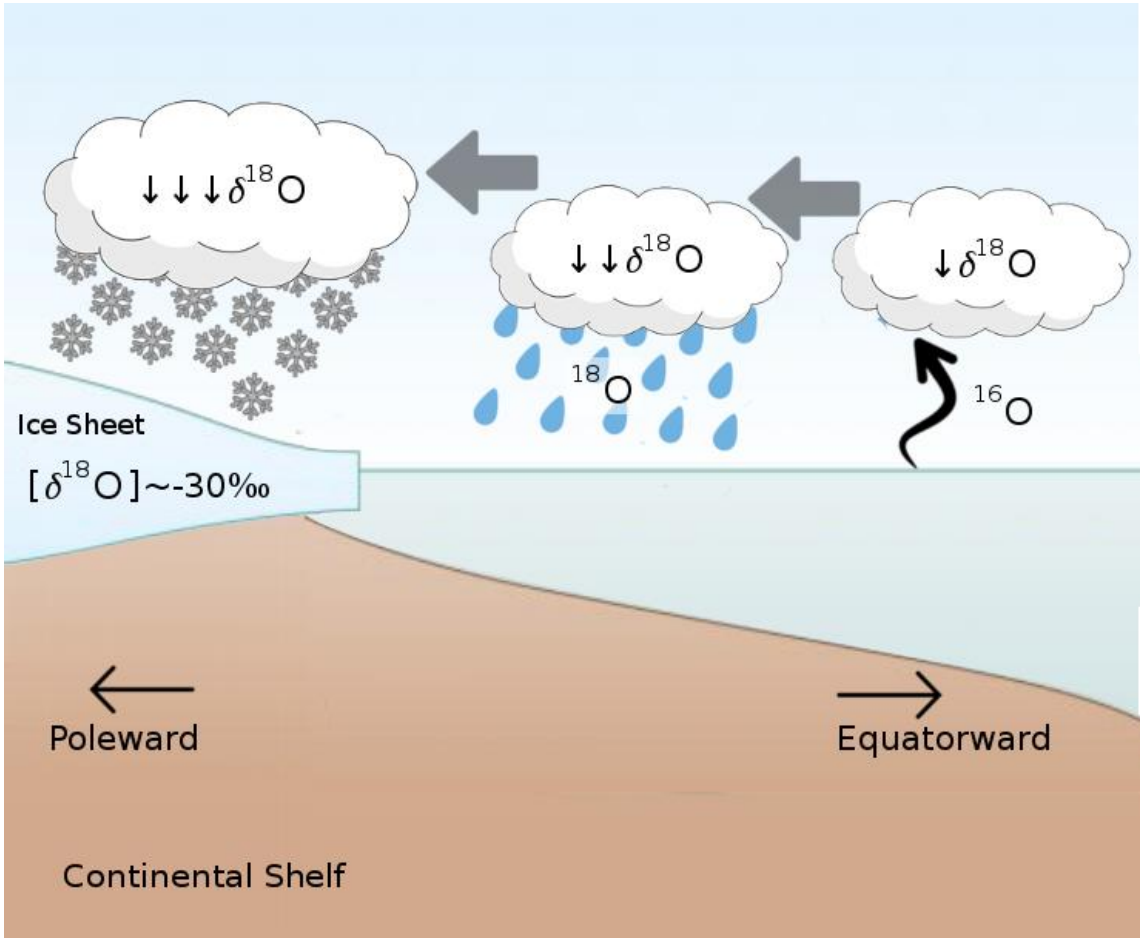

Figura IV.1 Esquema de transporte de isótopos de oxigênio e diminuição da $\delta^{18}O$ do equador para os pólos. [$\delta^{18}O$] representa a razão média isotópica de mantos de gelos polares (~30‰) , e as setas apontando para baixo representam a progressiva diminuição da $\delta^{18}O$ a médida que as massa de ar se movem para os pólos e precipitam o isótopo mais pesado (^{18}O).

A razão isotópica de oxigênio também tem a capacidade de registrar variações na temperatura do mar durante o processo de criação de conchas de $CaCO_3$ por organismos calcificadores. À medida que os organismos planctônicos calcificam eles registram uma determinada $\delta^{18}O$ no $CaCO_3$ que irá depender da disponibilidade dos isótopos mais leve e pesado de oxigênio na água e da temperatura no momento de calcificação. Isso acontece porque o fracionamento isotópico durante a calcificação

depende da temperatura ambiente [Bemis et al., 1998]. Assim, sabendo como a preferência isotópica do organismo é alterada pela temperatura, pode-se reconstruir a temperatura ambiente no momento de calcificação, através de funções empíricas de transferência [Kim and O'Neil, 1997; Bemis et al., 1998].

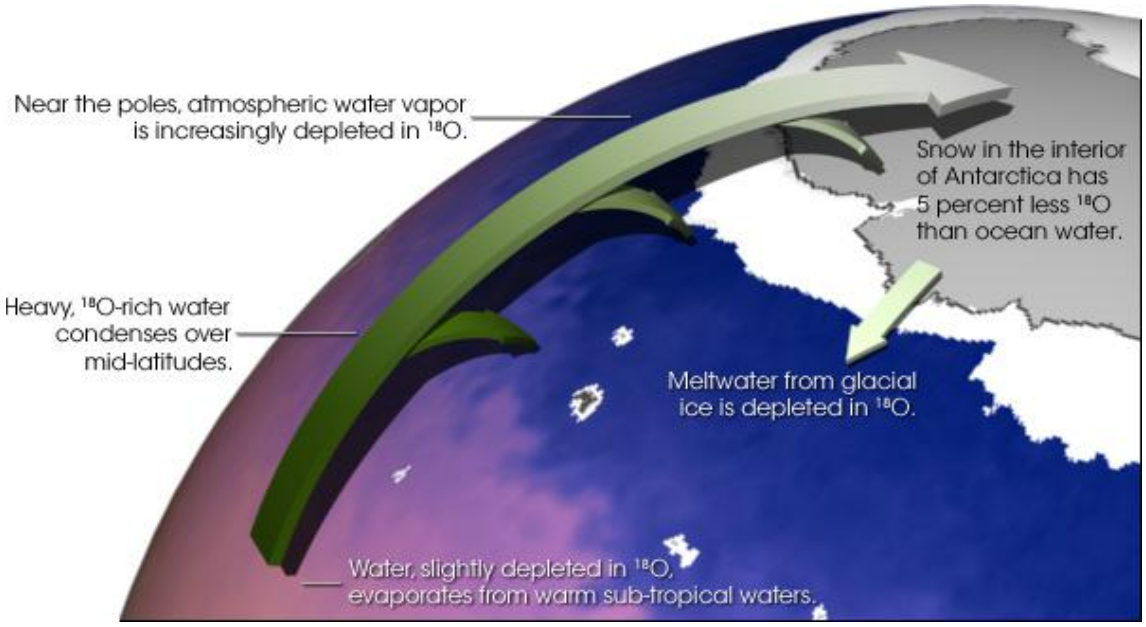

Figura IV.2 Esquema de transporte de isótopos de oxigênio no sistema terrestre, em resposta à circulação de massas de ar e ao fracionamento devido a precipitação e evaporação. Fonte: *Earth Observatory*, acesso: earthobservatory.nasa.gov/features/Paleoclimatology_OxygenBalance

Após sua morte, os foraminíferos calcificadores afundam na coluna d'água e são eventualmente enterrados nos sedimentos, assumindo que não haja dissolução. Portanto, a partir da coleta de testemunhos sedimentares ricos em organismos calcificadores, análise de constituição isotópica e datação do carbono presente no $CaCO_3$, é possível reconstruir a evolução da SST com base em testemunhos sedimentares.

Apesar dos métodos de reconstrução de SST baseados em $\delta^{18}O$ serem largamente utilizados, ainda existem grandes incertezas nestas reconstruções devido à empiricidade das funções de transferência da $\delta^{18}O$ para paleotemperatura, e devido ao erro inerente às medidas de $\delta^{18}O$ (~0,1 ‰, o que se traduz em um erro de ~0,4ºC em

temperatura [Kim and O'Neil, 1997]). Estes erros de reconstrução de SST, juntamente com as baixas resoluções e grandes desvios padrões nas datações dificultam a reconstrução da SST em eventos climáticos rápidos e abruptos, como o 8,2 ka AP. Uma forma de contornar estas incertezas é através da comparação direta das $\delta^{18}O$ medidas no fitoplâncton com razões isotópicas simuladas em modelos do sistema terrestre que representem processos de fracionamento isotópico.

Finalmente, uma última variável registrada pela $\delta^{18}O$ é a intensidade de precipitação continental e temperatura do ar. Isto ocorre principalmente em estalactites (i.e., espeleotemas), devido ao fracionamento durante a calcificação depender das condições de precipitação continental e umidade na caverna [Broecker et al., 1960; Hendy & Wilson, 1968].

IV.2 - Sistema de Monções da América do Sul - SAMS

Sistemas de monções são comumente definidos como sistemas de reversão dos ventos gerados por um aquecimento sazonal diferenciado de massas oceânicas e continentais [e.g. Webster et al., 1998]. Apesar dos cinturões dos ventos alísios e de oeste sobre a América do Sul não apresentarem uma reversão sazonal na sua direção como classicamente apresentado no sistema de monções asiático, oscilações sazonais na intensidade destes estão intrinsecamente ligadas à precipitação continental sobre a América do Sul [Zhou & Lau, 2001; Vera et al., 2006]. Este sistema acoplado de oscilação sazonal na intensidade dos ventos e da precipitação continental sobre a América do Sul é chamado de Sistema de Monções da América do Sul - SAMS [Liebmann et al., 2004].

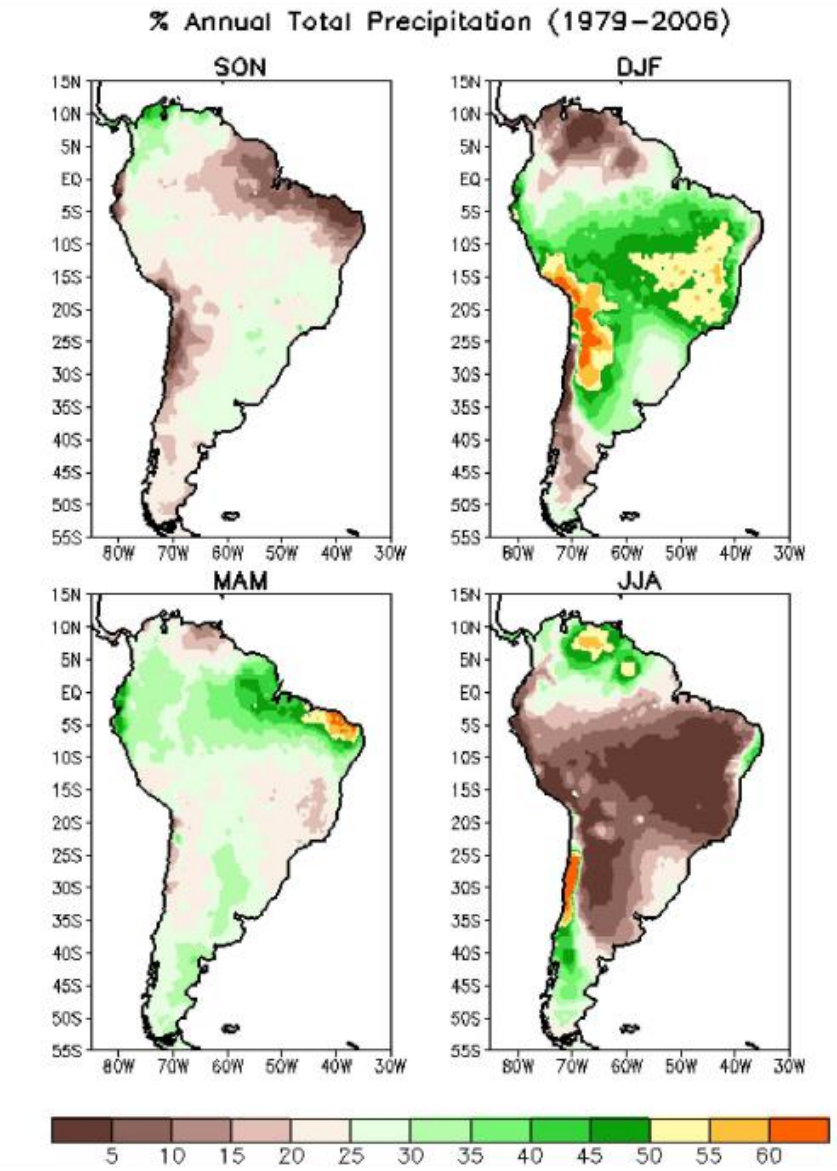

Figura IV.3 Padrões de precipitação na América do Sul gerados pelo SAMS. Valores de precipitação em percentual da precipitação total anual. Fonte:Silva & Kousky [2012]

O SAMS é um dos padrões climáticos mais importantes para a América do Sul, apresentando-se através de intensa convecção atmosférica e precipitação sobre a região tropical da América do Sul durante o verão austral e arrefecimento durante o inverno austral [Liebmann & Marengo, 2001; Gan et al., 2005]. A evolução deste sistema de precipitação se inicia durante a primavera austral, quando a ITCZ move-se para sul, intensificando a convecção sobre o nordeste do Brasil e sobre o centro da Amazônia [Liebmann & Marengo, 2001]. Parte desta faixa de alta precipitação se propaga para sul

através da Zona de Convergência do Atlântico Sul (SACZ) [Liebmann et al., 2004]. O pico de precipitação associado ao SAMS ocorre durante o verão austral a partir de quando as anomalias positivas de precipitação começam a diminuir, eventualmente levando ao total arrefecimento da precipitação durante o inverno austral (Fig IV.2) [Liebmann & Mechoso, 2011].

Apesar do modo de variabilidade principal do SAMS ser sazonal, sua intensidade varia consideravelmente em escalas interanuais e decenais. Em especial, alterações no Pacífico equatorial associadas ao *El Niño*/Oscilação Sul (ENSO) e anomalias de SST no Atlântico tropical e subtropical têm o poder de modular a intensidade e expressão espacial do SAMS [Cavalcanti, 2012]. Durante os eventos de *El Niño*, o aquecimento do Pacífico equatorial induz convecção atmosférica sobre esta região e, consequentemente, anomalias na célula de *Walker* (Fig IV.4). Como consequência da alteração na célula de *Walker*, o nordeste do Brasil durante o *El Niño* apresenta movimento descendente de massas de ar, impondo condições locais extremamente secas, diminuição intensa na precipitação devido ao SAMS [Andreoli & Kayano, 2007] e na drenagem continental [Silva et al., 2013]. O oposto ocorre durante os eventos *La Niña*, com intensificação da precipitação sobre o nordeste brasileiro e eventual ocorrência de enchentes. Enquanto isso, o sudeste do Brasil apresenta condições mais úmidas durante o *El Niño* [Marengo et al., 2018]. Anomalias de SST do Atlântico também influenciam o SAMS, especialmente as anomalias sobre o Atlântico Subtropical (estas serão discutidas na Seção IV.3).

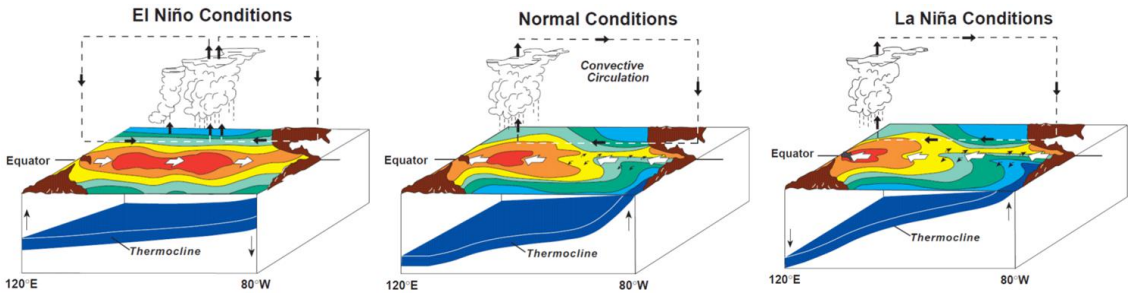

Figura IV.4 Esquema demonstrando a circulação da célula de *Walker* durante condições neutras no Pacífico equatorial (meio), eventos *El Niño* (esquerda) e *La Niña* (direita). Fonte: reefresilience.org/pt/climate-and-ocean-change/el-nino-southern-oscillation/

A modulação interanual do SAMS tem grande importância para a agricultura e fornecimento de energia elétrica [Silva & Kousky, 2012], especialmente devido à grande contribuição hídrica para a matriz energética nacional. Esta modulação interanual do SAMS pelo ENSO e pelas anomalias de SST no Atlântico Sul tem especial impacto social e econômico sobre o nordeste brasileiro devido à sua precipitação média anual ser a menor do país [Silva et al., 2013]. Especialmente, secas severas no nordeste do Brasil são comumente associadas às anomalias de SST negativas na região tropical do Atlântico Sul e Pacífico Equatorial [Rodrigues et al., 2011; Marengo et al., 2018]. Por outro lado, no sudeste brasileiro, eventos de intensificação do SAMS são associados a fortes enchentes, causando altas mortalidades e degradação da infraestrutura urbana [Silva & Kousky, 2012; Cai et al., 2020].

IV.2 - Dipolo Subtropical do Atlântico Sul - SASD

O SASD é um dos maiores modos de variabilidade de SST do Atlântico Sul Subtropical [Venegas et al., 1997]. Especialmente, Venegas et al. [1997] e Taschetto & Wainer [2008] atribuíram 20% da covariância de SST do Atlântico Sul às variações do SASD. O SASD apresenta-se, espacialmente, através de anomalias positivas (negativas)

de SST no nordeste (sudoeste) do Atlântico Sul em sua fase negativa, com o oposto durante sua fase positiva (Fig IV.5) [Venegas et al., 1996].

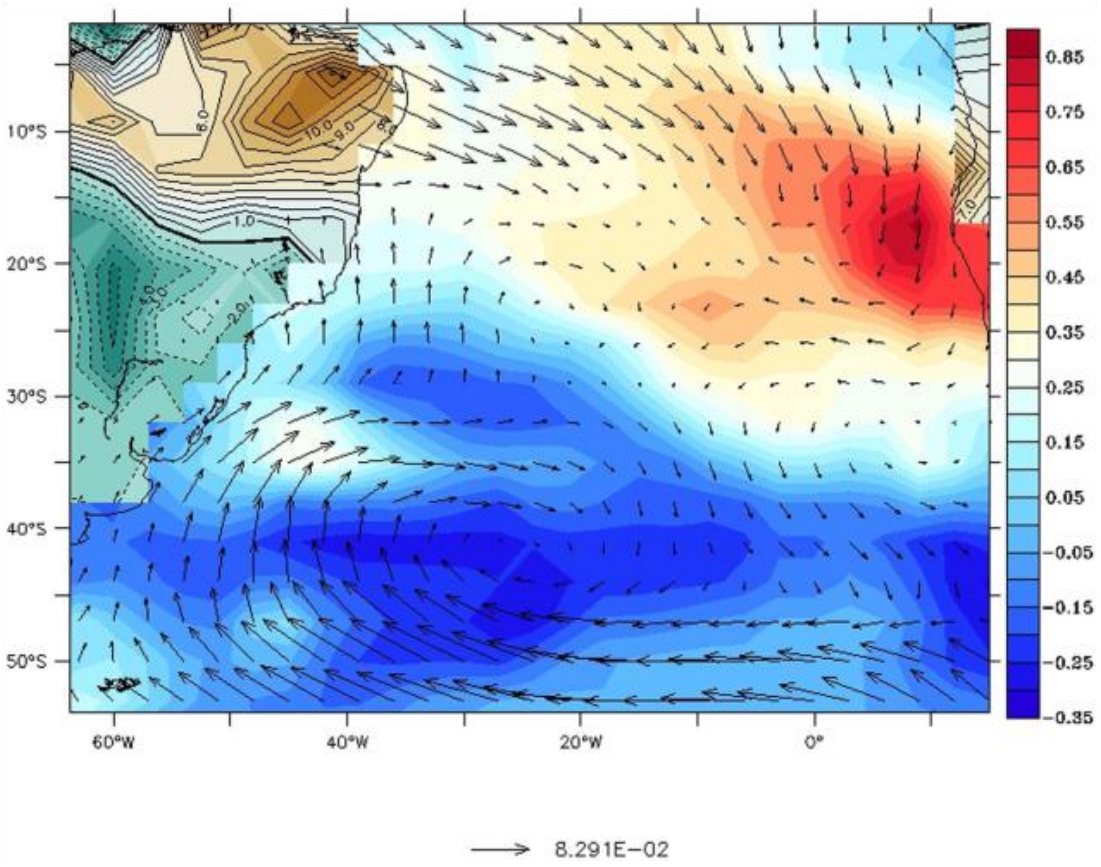

Figura IV.5 Padrão espacial de SASD negativo, e resposta na precipitação continental. Os contornos oceânicos em azul e vermelho representam anomalias de SST, enquanto os contornos continentais em ciano e marrom representam anomalias de precipitação continental. As setas são anomalias de direção e intensidade do vento em dyne cm^{-2}. Fonte: Wainer et al. [2014].

Dois mecanismos principais são utilizados para explicar o estabelecimento do SASD: [*A*] alterações na pressão no nível do mar devido ao fortalecimento da Alta Subtropical [Fauchereau et al., 2003] e [*B*] mudanças no bombeamento de *Ekman* e na ressurgência associada a este [Sterl and Hazeleger, 2003]. O mecanismo *A* se inicia com uma migração para sul e intensificação da Alta Subtropical durante a primavera austral, intensificando o fluxo de calor latente sobre o pólo sudoeste do SASD e diminuindo este fluxo, sobre o polo nordeste [Fauchereau et al., 2003]. Devido às alterações no

fluxo de calor latente, a camada de mistura sobre o polo sudoeste (nordeste) fica mais rasa (profunda), permitindo rápido aquecimento do polo sudoeste pela radiação incidente de onda curta, enquanto o pólo nordeste (camada de mistura mais profunda) não aquece na mesma proporção [Morioka et al., 2011]. O rápido (lento) aquecimento da SST no polo sudoeste (nordeste) permite então o desenvolvimento das anomalias de SST referentes a um SASD positivo (Fig IV.6).

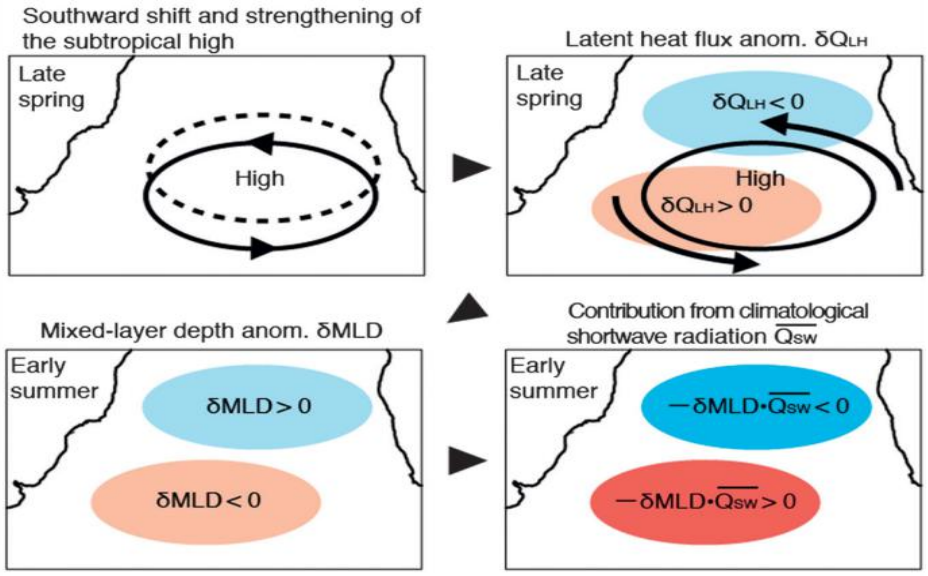

Figura IV.6 Esquema de evolução do SASD positivo de acordo com o mecanismo [*A*]. As linhas e setas pretas representam o deslocamento para sul e fortalecimento da Alta Subtropical. Os contornos vermelhos (azul) representam anomalias positivas e negativas de SST. Q_{LH} e MLD representam anomalias nos fluxos de calor latente (Q_{LH}) e na profundidade da camada de mistura (MLD). Q_{sw} representa a anomalias no fluxo de radiação curta incidente. Fonte: Morioka et al. [2011].

No mecanismo *B*, uma diminuição na intensidade dos ventos alísios de sudeste enfraquece o bombeamento de *Ekman* e diminui a intensidade da ressurgência na costa da África. Uma aceleração dos ventos de Oeste ocorre concomitantemente à desaceleração dos Alísios, fortalecendo a ressurgência costeira na costa do Brasil [Morioka et al., 2011]. A alteração diferencial na ressurgência costeira, então, favorece um aquecimento (resfriamento) da superfície do nordeste (sudoeste) do Atlântico Sul

devido à diminuição (aumento) da mistura com águas mais frias de subsuperfície, formando as anomalias de SST durante o dipolo negativo [Hermes & Reason, 2005].

O SASD exerce controle sobre o SAMS especialmente através de alterações na evaporação sobre o Atlântico Sul. Durante a fase negativa, o aquecimento da superfície do pólo nordeste do SASD potencializa a evaporação no Atlântico tropical, aumentando a advecção de vapor d'água para o nordeste da América do Sul e assim intensificando a precipitação sobre o nordeste brasileiro, associada ao SAMS [Wainer et al., 2015]. Ao mesmo tempo, as menores temperaturas sobre o sudoeste do Atlântico Sul diminuem a evaporação na região subtropical e consequentemente o transporte atmosférico de vapor d'água para o sudeste do Brasil. O menor transporte de vapor na região subtropical então favorece condições secas sobre o sudeste do Brasil (Fig IV.5).

Durante o presente, oscilações do SASD explicam até 20% da variância na precipitação devido ao SAMS, portanto tendo efeito secundário sobre a intensidade do SAMS [Taschetto & Wainer, 2008]. No entanto, simulações paleoclimáticas e *proxies* de SST apontam que durante o início do Holoceno, o SASD possivelmente exerceu controle primário na modulação da precipitação continental devido ao SAMS [Wainer et al., 2015].

Capítulo V: Dados e Métodos

V.1 Dados *paleoproxies*

Para os estudos apresentados nesta tese, foram utilizadas reconstruções de SST baseadas em diversos *proxies* biogeoquímicos obtidos através de Morrill et al. [2013] e, também, por busca através do banco de dados paleoceanográficos da *National Oceanic and Atmospheric Administration* - NOAA. A localização dos *proxies* utilizados nos capítulos VI e VII está demonstrada na figura V.1.

À medida em que os métodos de datação isotópica evoluem, as curvas base de razão isotópica utilizadas para corrigir datações são atualizadas. Desta forma, estudos que utilizam *paleoproxies* obtidos em décadas diferentes precisam ser re-calibrados para uma única curva isotópica atualizada, a fim de garantir que a cronologia destes coincida.

Assim, os *paleoproxies* utilizados neste estudo foram recalibrados com base na curva isotópica marinha mais recente e utilizando o *software bacon* para R [Blaaw & Christen., 2011]. *Bacon* se utiliza de interações de cadeia do tipo Markov Monte-Carlo para atualização da datação de *proxies*, sendo um dos métodos mais largamente utilizados na comunidade científica.

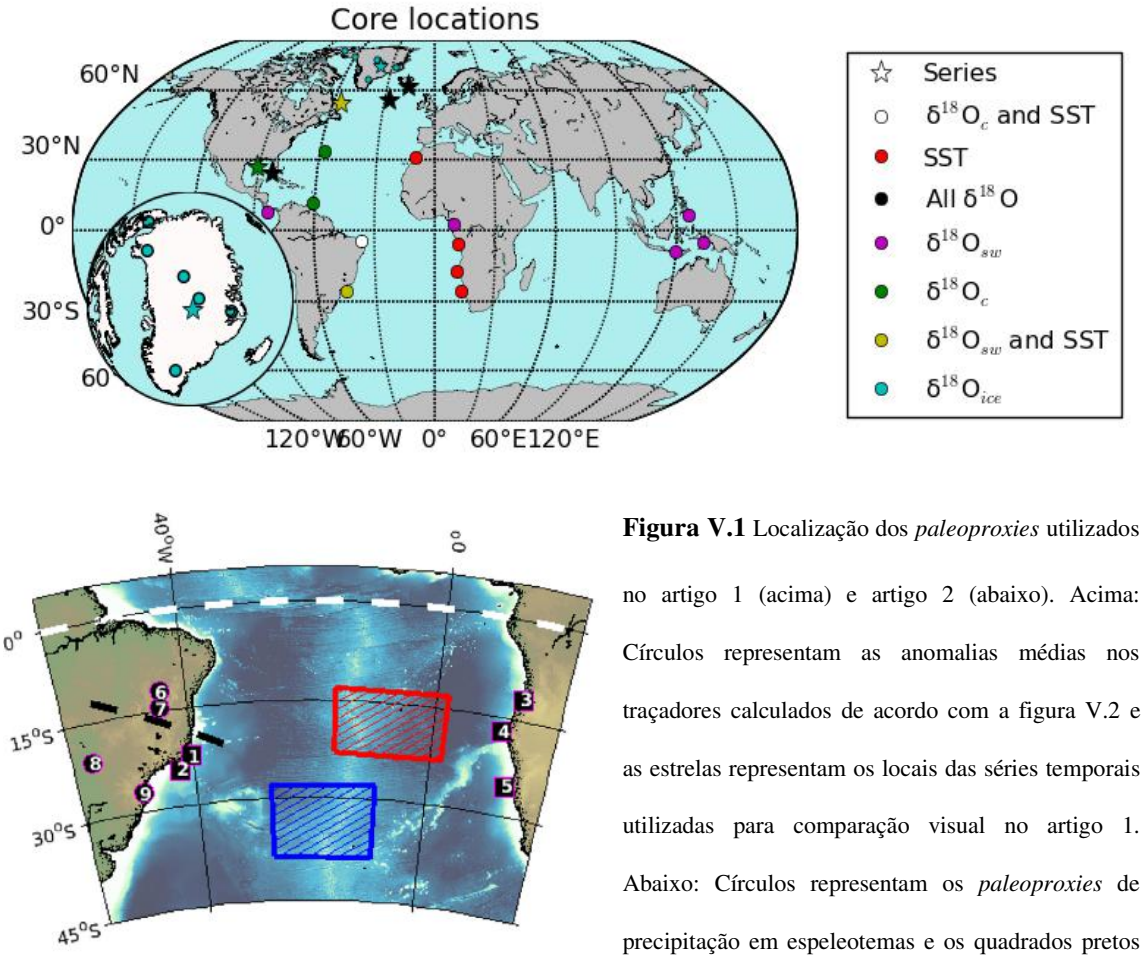

Figura V.1 Localização dos *paleoproxies* utilizados no artigo 1 (acima) e artigo 2 (abaixo). Acima: Círculos representam as anomalias médias nos traçadores calculados de acordo com a figura V.2 e as estrelas representam os locais das séries temporais utilizadas para comparação visual no artigo 1. Abaixo: Círculos representam os *paleoproxies* de precipitação em espeleotemas e os quadrados pretos as reconstruções de SST. Os quadrados vermelho e azul hachurados representam os polos nordeste e sudeste do SASD.

No capítulo VI, foram utilizados 35 *paleoproxies* diferentes, obtidos de 27 testemunhos de gelo e de sedimento, obtendo registros de razão isotópica de oxigênio na água ($\delta^{18}O_{sw}$), no gelo ($\delta^{18}O_i$), em $CaCO_3$ ($\delta^{18}O_c$), além de reconstruções de SST. Anomalias nos *proxies* foram calculadas de acordo com Morrill et al. [2014], sendo elas

a diferença entre as medições de $\delta^{18}O$ (ou SST) e suas média utilizando os intervalos de tempo [7 - 7,9] ka AP e [8,5 - 9] ka AP. Estas anomalias são calculadas somente para valores fora do intervalo de média ± 2 desvios padrões a fim de detectar eventos anômalos, e por isto os intervalos de tempo utilizados para a média, propositalmente, não incluem o período entre 7,9 ka AP e 8,5 ka AP, que engloba o evento de 8,2 ka AP (Fig V.2).

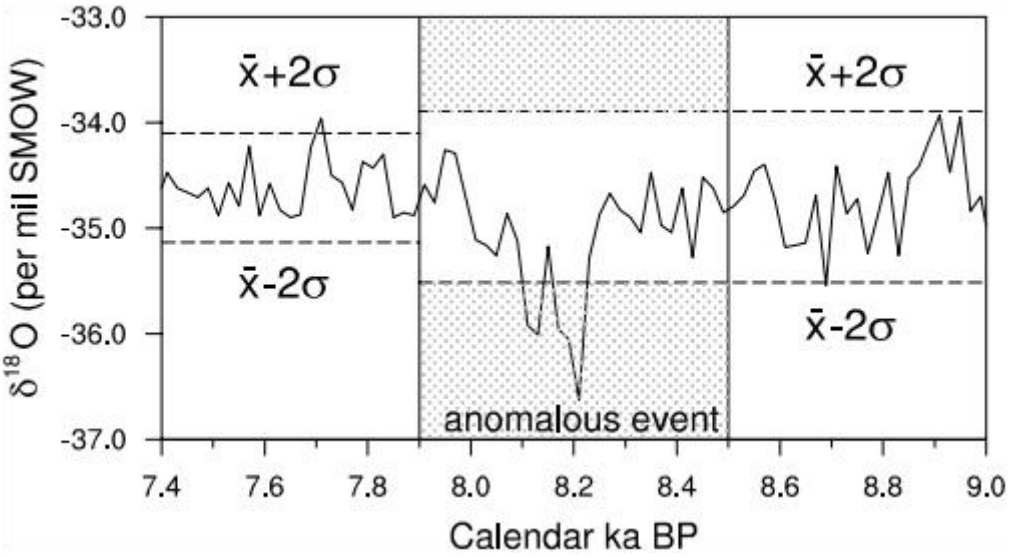

Figura V.2 Esquema de cálculo de anomalias médias do 8,2 ka AP. A média é calculada somente para valores na região hachurada, i.e., 2 desvios padrões acima ou abaixo da média entre 9 ka AP e 7,4 ka AP. Fonte: Morrill et al., [2013]

V.2 - Modelos Numéricos

Ainda que os dados *paleoproxy* sejam uma das formas mais comuns de entender o clima do passado, a baixa cobertura espacial e temporal destes dados torna extremamente difícil a interpretação de mecanismos de mudanças climáticas. Para contornar tal problema, simulações paleoclimáticas, utilizando os parâmetros orbitais dos ciclos de *Milankovitch* (excentricidade, obliquidade e precessão), como forçantes

em modelos numéricos do sistema terrestre foram utilizadas nesta tese. Em conjunção com os *proxies*, estas simulações fornecem a possibilidade de avaliação de mecanismos dinâmicos capazes de explicar as alterações vistas nos registros sedimentares. Nesta seção, serão descritos os modelos utilizados e as simulações feitas.

V.2.1 *Community Climate System Model version 3* - Descrição

Duas das simulações presentes neste trabalho utilizam o modelo *Community Climate System Model version 3* - CCSM3. O CCSM3 é distribuído pelo *National Center for Atmospheric Research* (NCAR [Collins et al., 2006]) e simula a atmosfera, o gelo marinho, o oceano e a superfície terrestre. O componente oceânico do modelo é simulado pelo *Parallel Ocean Program (POP*-[Smith & Gent., 2002]*)*, enquanto o componente atmosférico do CCSM3 é baseado no *Community Atmospheric Model versão 3* [CAM3 - Collins et al., 2006]. Uma vegetação dinâmica é simulada no CCSM3 com base no *Dynamic Vegetation Model*. Por fim, alterações no gelo marinho são simuladas utilizando o *Community Sea Ice Model* [Boville & Gent, 1998].

V.2.1.1 *Simulation of the Transient Climate of the Last 21,000 Years* – TraCE-21ka.

A primeira simulação utilizada é a *Simulation of the Transient Climate of the Last 21,000 Years – TraCE21ka*. A TraCE21ka consiste em uma rodada transiente com condições iniciais do LGM obtidas de Otto-Bliesner et al. [2006], e concentração de gases estufa transientes [Joos & Spahni, 2008]. Partindo do LGM (22 ka AP) o modelo é rodado continuamente até 0 ka AP. No TraCE21ka, a descarga devido ao derretimento do LIS é inserida na simulação através de um fluxo de água doce para o Atlântico Norte e Ártico de 8,31 m/ka de 8 a 9 ka AP, com 7,47 m/ka (em SLR) advindo da Baía de Hudson [Clarke et al., 2004]. Este fluxo totaliza 0,086 Sv de descarga contínua de água

doce entre 8 a 9 ka BP. Para simular o colapso do Lago Agassiz, 5 Sv de água doce foi inserido abruptamente em 8,5 ka durante seis meses, com base em Barber et al. [1999]. Os valores de descarga de água doce do LIS inseridos no TraCE21ka são obtidos de reconstruções de Clark et al. [2012]. O TraCE21ka tem 2,8° de resolução espacial, com 25 níveis verticais e profundidade máxima de 5500m [He, 2011]. A evolução transiente das plataformas de gelo continentais utilizada nesta simulação se baseia nas reconstruções de Peltier [2004].

V.2.1.2 Simulação não transiente

Um segundo conjunto de simulações utilizando uma configuração do CCSM3 com alta resolução foi utilizada nesta tese, com o modelo oceânico possuindo uma resolução latitudinal de 0,5° e longitudinal de 1°, além de 40 níveis verticais [Wagner et al., 2013 ;Morrill et al., 2014]. Esta é uma simulação de equilíbrio que, portanto, utiliza os parâmetros orbitais obtidos por Berger, [1978] fixos em 8,5 ka AP. Duas rodadas foram usadas com essa configuração, uma com descarga de água doce no mar de Labrador (chamada de FWF) e outra sem (controle). A forçante de água doce utilizada simula o colapso do Lago Agassiz-Ojibway através de um fluxo de 2,5 Sv no mar de Labrador durante o primeiro ano da rodada. Para simular a descarga de água de degelo referente ao derretimento do domo de gelo da Baía de Hudson, 0,13 Sv de água doce foi adicionado continuamente no mar de Labrador do ano 2 ao 99 da simulação. Por fim, a simulação segue do ano 100 ao ano 150 sem adição de água doce [Morrill et al., 2014]. A simulação controle também é rodada por 150 anos a fim de permitir a comparação com a FWF e se poder separar os efeitos da mudança de flutuabilidade no mar de Labrador devido à água de degelo.

V.2.2 *University of Victoria Earth System Model* - Descrição

Simulações adicionais foram feitas utilizando o *University of Victoria Earth System-Climate Model* versão 2.9 [Weaver et al., 2001; Brennan et al., 2012 - Modelo UVic]. O Modelo UVic simula a atmosfera, o oceano, a superfície terrestre, a vegetação dinâmica, o gelo marinho [Hibler III, 1979] e fluxos sedimentares [Archer, 1996]. O componente oceânico é simulado pelo *Modular Ocean Model versão* 2 [MOM2 - Pacanowski, 1996], com 19 níveis verticais de resolução vertical, variando entre 50 metros na superfície e 500 metros no fundo, e com resolução latitudinal (longitudinal) de 1,8º (3,6º). A molécula da água nos componentes atmosféricos, oceânicos, de gelo marinho e superfície terrestre do modelo da UVic é compartimentalizada entre $H_2{}^{18}O$ e $H_2{}^{16}O$ a fim de calcular, prognosticamente, a razão isotópica de oxigênio em diferentes componentes do sistema terrestres [Meissner et al., 2003; Brennan et al., 2012, 2013; Yeung et al., 2019].

V.2.2.1 UVic - Simulação

Para simular o 8,2 ka AP, o modelo da UVic foi forçado utilizando os campos de ventos atuais da reanálise do *National Center for Environmental Prediction-NCEP* [Kalnay et al., 1996]. Todas as simulações com o modelo UVic foram forçadas com parâmetros orbitais fixos referentes a 9 ka AP, i.e., excentricidade= 0.0167, obliquidade= 23,45º, longitude do periélio= 102,04º, e concentração de CO_2 pré-industrial [280 ppm -Berger, 1978]. Inicialmente uma rodada de equilíbrio de 10 mil anos foi feita a fim de garantir que os traçadores e circulação oceânicos estejam em equilíbrio, com os últimos 2 mil anos desta rodada sendo a simulação controle.

Para o capítulo VI, 28 simulações com o modelo UVic foram rodadas, com diferentes forçantes de água doce (Capítulo VI, tabela 1). As descargas de água doce para estas simulações são feitas através de fluxos virtuais equivalentes de sal. Todos os experimentos deste capítulo adicionaram água doce sobre o mar do Labrador (50º-65ºN, 35º-70ºW). A variação na magnitude e duração das descargas utilizadas para forçar o modelo UVic foi feita com o objetivo de testar a melhor forçante para representar as alterações isotópicas nos *paleoproxies*.

Para o capítulo VII, uma simulação foi feita em que a descarga de água doce referente ao derretimento do LIS foi adicionada através de um fluxo de 0,086 Sv para o mar de Labrador, na mesma localização das simulações anteriores. A fim de permitir que os oceanos alterem a circulação atmosférica, o mecanismo de *feedback* dinâmico e geostrófico foi ativado para esta simulação. Para simular o colapso do lago Agassiz-Ojibway, 2,5 Sv de água doce foram liberados na mesma região do mar do Labrador durante o ano 8,5 ka AP. Um fluxo virtual de sal decrescendo de -0,2 Sv até -0,05 Sv entre 8 ka e 7,5 ka foi adicionado, a fim de iniciar a AMOC em sua fase colapsada.

V.3 - Métodos Analíticos

V.3.1 - Comparação entre modelo e *proxy*

A comparação entre *proxies* e modelo no capítulo VI foi feita através de cálculos de erros médios quadráticos (RMSE). Além disso, uma regressão linear entre as razões isotópicas simuladas e obtidas nos *proxies* foi feita. Assume-se que o modelo representou bem as anomalias nos *proxies* quando o coeficiente de regressão linear é ~1. Os parâmetros estatísticos de RMSE, desvio padrão e correlação linear de *Pearson* foram calculados para as séries temporais de $\delta^{18}O$ e avaliados através de diagramas de

Taylor [Taylor, 2001]. Para garantir que a diferença entre os RMSEs das simulações sejam representativos, o teste de Diebold-Mariano foi feito em todos os RMSEs derivados das séries temporais [Diebold & Mariano, 2002], e os resultados do teste de hipótese são apresentados no Apêndice 2 (Material suplementar 2 do capítulo VI).

V.3.2 Gangorra Bipolar, Dipolo Subtropical do Atlântico Sul e a AMOC.

O efeito da gangorra bipolar de calor nas anomalias de SST no capítulo VII foi avaliado através do primeiro modo de variabilidade da função ortogonal empírica de SST global nos modelos utilizados. Como a gangorra de calor é afetada diretamente pela intensidade do revolvimento da AMOC, o índice da AMOC foi calculado através do valor máximo da função de corrente da AMOC entre 20ºN e 70ºN e entre 200 m e 3000 m [Yang et al., 2015].

A fim de avaliar a variabilidade do SASD nos dados *paleoproxy*, o índice $SASD_{proxy}$ foi calculado com base na diferença de anomalias de SSTs reconstruídas nas costas leste e oeste do Atlântico Sul (Fig. V.1). O método utilizado para este cálculo baseia-se em Wainer et al. [2015]. Já para os modelos utilizados no capítulo VII, foram calculados dois índices diferentes, o $SASD_{coast}$ e o $SASD_{model}$. O $SASD_{model}$ foi obtido pela diferença de anomalias de SST entre o sudoeste (30º-40ºS, 30º-10ºW) e nordeste do Atlântico Sul (15º-25ºS, 0º-20ºW), de acordo com a abordagem de Morioka et al., [2011] (Quadrados azul e vermelho, Fig. V.1, abaixo). Para garantir comparabilidade com os índices calculados para o modelo e para os *proxies,* o $SASD_{coast}$ foi calculado através da diferença de anomalias de SST das células na costa leste e oeste do Atlântico Sul, entre os contornos latitudinais do índice $SASD_{model.}$

V.3.3 Profundidade das isotermas

Os mecanismos de controle do SASD explicados no capítulo VII se baseiam em deslocamentos verticais das isotermas do Atlântico Sul. Para poder separar a ação do vento em promover movimentos verticais nas isotermas no Atlântico Sul, uma derivação do modelo de 1,5 camada no Atlântico Sul foi feita, obtendo-se a seguinte equação:

$$h^2(x, y) = \frac{2f^2(y)}{\beta(y)\gamma} w_e(x - x_e) + H^2(y) \qquad \textbf{Eq V.1}$$

onde $h^2(x, y)$ é a profundidade da isoterma de 17ºC prevista em resposta ao efeito do vento, em função da longitude (x) e latitude (y). $H^2(y)$ é a profundidade da isoterma de 17ºC medida na costa leste do Atlântico Sul no modelo, e $D(x, y) = \sqrt{\frac{2f^2(y)}{\beta(y)\gamma} w_e(x - x_e)}$ é o incremento da profundidade da isoterma sobre a bacia oceânica, onde $(x - x_e)$ representa a distância da costa leste. Os fatores γ e w_e, representam a estratificação da densidade e o bombeamento de *Ekman*. Mais informações sobre a derivação da equação V.1 estão presentes no Apêndice 3 (Material suplementar do capítulo VII).

Capítulo VI: Pulsos de degelo associados ao evento de 8,2 ka AP

Este capítulo traz o primeiro artigo científico publicado a partir desta tese, de autoria de Wilton Aguiar, Katrin J. Meissner, Álvaro Montenegro, Luciana Prado, Ilana Wainer, Anders E. Carlson e Mauricio M. Mata e intitulado "***Magnitude of the 8.2 ka event freshwater forcing based on stable isotope modelling and comparison to future Greenland melting***". O mesmo encontra-se publicado no periódico "*Scientific Reports*", volume 11 (2021), que pode ser encontrado em https://doi.org/10.1038/s41598-021-84709-5. O formato de citação do artigo foi alterado para melhor indexação e compreensão da tese.

VI.1 Síntese do capítulo

A quantificação dos fluxos de água doce responsáveis por desacelerar o revolvimento oceânico durante o início do Holoceno é uma peça-chave para garantir a comparabilidade das anomalias climáticas do 8,2 ka AP com os efeitos do futuro derretimento do manto do GIS. Este capítulo tem como objetivo principal reconstruir a

magnitude e duração dos fluxos de água doce responsáveis por diminuir a convecção profunda no Atlântico Norte e a circulação da AMOC, iniciando o evento de 8,2 ka AP. Além disso, faz-se uma comparação entre os valores dos fluxos de água doce reconstruídos para o 8,2 ka AP e as estimativas de derretimento do GIS no cenário de altas emissões de dióxido de carbono para este milênio *(Representative Concentration Pathway 8.5* - RCP8.5).

Os resultados demonstram que os fluxos de água doce para o mar do Labrador durante o 8,2 ka AP são semelhantes às projeções de derretimento do GIS para o milênio entre os anos 2000 e 3000 tanto em duração (~1000 anos) como em intensidade de descarga e água doce (~7.5 m em SLR). Este resultado traz à luz novamente a hipótese de que o evento de 8,2 ka AP pode ser utilizado para entender as anomalias climáticas devido à futura desaceleração da AMOC.

VI.2 Artigo científico 1

VI.2.1 Abstract

The northern hemisphere experienced an abrupt cold event ~8200 years ago (the 8.2 ka event) that was triggered by the release of meltwater into the Labrador Sea, and resulting in a weakening of the poleward oceanic heat transport. Although this event has been considered a possible analogue for future ocean circulation changes due to the projected Greenland Ice Sheet (GIS) melting, large uncertainties in the amount and rate of freshwater released during the 8.2 ka event make such a comparison difficult. In this study, we compare sea surface temperatures and oxygen isotope ratios from 28 isotope-

enabled model simulations with 35 paleoproxy records to constrain the meltwater released during the 8.2 ka event. Our results suggest that a combination of 5.3 m of meltwater in sea level rise equivalent (SLR) released over a thousand years, with a short intensification over ~130 years (an additional 2.2 m of equivalent SLR) due to routing of the Canadian river discharge, best reproduces the proxy anomalies. Our estimate is of the same order of magnitude as projected future GIS melting rates under the high emission scenario RCP8.5.

VI.2.2 Introduction

Greenland ice-sheet melting is one of the major responses to the rising atmospheric greenhouse gas concentrations and global mean temperature (Cazenave, 2006; Fettweis et al., 2017; Tedesco and Fettweis, 2012). The addition of ice-sheet meltwater to the North Atlantic will potentially have a destabilizing effect on the Atlantic Meridional Overturning Circulation (AMOC), which could weaken by more than 70% within the next few centuries (Bakker et al., 2016; Golledge et al., 2019; Swingedouw et al., 2007). Past meltwater-driven AMOC slowdowns have repeatedly led to millennia-long cold events in the Northern Hemisphere: for example, the Oldest and Younger Dryas (~19 to 14.7 kiloyears and 12.9 to 11.7 kiloyears before the present, respectively)(Clark et al., 2012, 2002; Marson et al., 2014). However, the cold event 8.2 kiloyears before present (8.2 ka event hereafter) differs from previous cold events due to its short, century-long duration (Alley and Agustsdottir, 2005; Morrill and Jacobsen, 2005). The 8.2 ka event also took place in the current interglacial period under

boundary conditions that were closer to pre-industrial conditions than earlier cold events (Schmidt and Legrande, 2005).

Several freshwater forcing hypotheses involving the Laurentide Ice Sheet (LIS) have been suggested for the 8.2 ka event. These scenarios include three freshwater sources: the drainage of Lake Agassiz (Barber et al., 1999), the change in North American continental freshwater routing from LIS retreat (Carlson et al., 2009; Clark, 2001), and the on-going retreat of the LIS and its associated meltwater production (Carlson et al., 2008; Gregoire et al., 2012; Ullman et al., 2016). The first two sources have relatively well-constrained discharge rates and volumes (Carlson et al., 2009; Clarke et al., 2004) when compared to the direct ice-sheet meltwater source (Carlson et al., 2009; Carlson et al., 2008; Clarke et al., 2004; Gregoire et al., 2012). Even though the outburst of Lake Agassiz is commonly considered the main trigger for the 8.2 ka event (Barber et al., 1999), recent studies have found that both the LIS retreat and change in the routing of continental discharge might have had a significant role in causing the climate event's anomalies (Carlson et al., 2009; Carlson et al., 2008; Meissner and Clark, 2006), thus raising uncertainties on the role of each of the three meltwater sources in triggering the 8.2 ka event.

The range of estimates of the magnitude of total freshwater release during the 8.2 ka event is also large (Alley and Agustsdottir, 2005; Morrill and Jacobsen, 2005), ranging from 1.5 m to 9 m in equivalent sea-level rise (SLR) (Carlson et al., 2008; Li et al., 2012). Some of these scenarios were previously used to simulate the cold event with numerical climate models in an attempt to estimate the climatic impacts of the freshwater discharge (Morrill et al., 2014; Wagner et al., 2013; Wiersma et al., 2006), and simulation skill was evaluated by comparison with sea surface temperature (SST)

reconstructions. Such a large range of meltwater volume is enough to create scenarios ranging from a small change in circulation to a total collapse of the AMOC (Aguiar et al., 2020). Furthermore, due to a model-dependent stability of ocean overturning, location of deep convection sites and meridional heat transport, the simulated SST response to freshwater forcing varies significantly between distinct simulations (Cheng et al., 2013; Weaver et al., 2012). This model dependency makes it difficult to test which freshwater source played the dominant role in triggering the 8.2 ka based on the comparison between the simulated SST response and reconstructed SST changes. However, these uncertainties can be reduced by using a combination of active and non-active tracers, such as oxygen isotopes as well as SSTs.

Constraining the amount of freshwater involved in the 8.2 ka event, and the role of each freshwater source in creating the climate anomalies of the event, will enhance our understanding of the sensitivity of the climate system to freshwater fluxes, which is of obvious importance for future scenarios given the observed recent acceleration of Greenland ice-sheet (GIS) mass loss (Cazenave, 2006; Fettweis et al., 2017; Golledge et al., 2019). In this study, we aim to constrain the magnitude and length of freshwater flux that caused the 8.2 ka event. We explore this question by using numerical simulations that calculate both oxygen isotopes, in seawater, in carbonates, and in ice cores, and SSTs prognostically and by comparing the simulations with paleoclimate records of the same variables.

VI.2.3 Methods

VI.2.3.1 Model and data

Simulations were performed using the University of Victoria Earth System Climate Model version 2.9 (UVic Model - Weaver et al., 2001), with the addition of oxygen isotopes (Brennan et al., 2013, 2012). Water in the ocean, atmosphere, sea-ice, and on land is compartmentalized into ^{18}O and ^{16}O to allow the estimation of $\delta^{18}O$ distribution (Bagniewski et al., 2017, 2015; Brennan et al., 2013, 2012; Yeung et al., 2019). A detailed description of the experimental setup is given in the Supporting Information. We compared simulated $\delta^{18}O$ and SSTs to paleoclimate record mean anomalies for the 8.2 ka event (averaged between 7.9 ka and 8.5 ka – Supplementary) and time series from six locations (Fig. S1-stars). Mean anomalies of oxygen isotope ratios in seawater ($\delta^{18}O_{sw}$), carbonate ($\delta^{18}O_c$), ice ($\delta^{18}O_{ice}$), and SSTs, were taken from (Morrill et al., 2013). These proxy anomalies are based on data from 27 cores (Fig. S1), some recording more than one paleoclimate proxy. Overall, our analysis includes ten SST records, ten $\delta^{18}O_{sw}$ records, seven $\delta^{18}O_c$ records and eight $\delta^{18}O_{ice}$ records. The mean anomalies in the simulations are calculated following the methodology by (Morrill et al., 2013). They are defined as the difference between SST (or $\delta^{18}O$) values averaged between 7.9 ka and 8.5 ka and their climatological mean, only for values above (or below) the mean plus (minus) two standard deviations. The climatological mean is defined as the average between 9 and 7 ka, excluding the period between 7.9 ka and 8.5 ka.

For most records, the simulated values were taken at the model's grid cell closest to the geographical coordinates of each core, at the surface level of the ocean model (17.5 m). The tracers reconstructed from *Globorotalia inflata* were compared to the simulated ocean tracers averaged between 82.5 m and 177.5 m, due to the wide range of vertical migration inherent to this species. Thus, time series for the RAPiD

core based on *Globigerina bulloides* reflect surface changes, while those based on *G. inflata* reflect changes in the upper thermocline. The UVic model does not simulate isotopic fractionation during foraminiferal calcification. Thus, model $\delta^{18}O_c$ was estimated by an SST-based transfer function (Bemis et al., 1998; Kim and O'Neil, 1997).

In order to evaluate the simulations' skill in reproducing the reconstructed $\delta^{18}O$, the linear regression's slope (α) and Root Mean Square Errors (RMSE) were calculated for the model anomalies using proxy anomalies as reference. Equality between model and proxy happens when $\alpha=1$. For the time series, centered RMSE, normalized standard deviations and Pearson's correlations were compared in a Taylor diagram in order to evaluate the performance of the simulations in reproducing the proxy time series. To assure that the difference of the RMSEs for the time series of $\delta^{18}O_{sw}$ and $\delta^{18}O_c$ are significant, we performed a Diebold-Mariano test between each of the experiments in Part B (Diebold and Mariano, 2002). We then report the Diebold-Mariano test results and its significance level for the simulations with the best performances. All remaining values of the Diebold-Mariano test and its critical confidence percentages are presented in the Supplementary Information (Supplementary S2). More information on the experimental setup and core data can be found in the Supplementary Material.

VI.2.3.2 **Freshwater forcing for the simulations based on earlier reconstructions**

There are four main estimates of freshwater input into the North Atlantic close to the time of the 8.2 ka event. A glacial isostatic adjustment model by Peltier (2004) estimates that 27.1×10^5 km^3 of freshwater were added to the North Atlantic from LIS retreat from 9 ka to 8 ka. The meltwater from LIS estimated by Peltier (2004) in reality

did not flow entirely into the Labrador Sea, so this estimate can be used as an upper constraint for total meltwater discharged in the Labrador Sea in the period. Carlson et al., (2009) estimate a 0.13 Sv ± 0.03 Sv increase in the inflow of freshwater into Labrador Sea after the collapse of Hudson Bay that ended ~8.2 ka (Ullman et al., 2016) due to the routing of the western Canadian Plains runoff ($8.2x10^5$ km^3 in volume). Although the routing event does not contribute to SLR, it would still alter the oxygen isotope ratios and surface water buoyancy in the Labrador Sea, thus potentially affecting deepwater formation rates. Li et al. (2012) found a 1.5 ± 0.7 m of eustatic SLR between 8.31 ka and 8.18 ka ($5.3x10^5$ km^3 in volume) from a SLR reconstruction, which includes the freshwater release from the lake outburst. Ullman et al. (2016) estimate that additional melting of the LIS after its collapse contributed to 3.6 ± 0.4 m of SLR that began ~8.2 ka and ended 7.6 ± 0.6 ka (~$9.5x10^5$ km^3 in volume). The estimated Antarctic Ice Sheet contribution to SLR during the early-Holocene is lower than 3 cm, i.e. substantially smaller than LIS (Briggs and Tarasov, 2013), so no meltwater was added in the Southern Hemisphere in the simulations. Using these estimates, we derived four main freshwater release experiments running from 9 ka until 7 ka (Table 1, (I) Reconstructions).

It is important to highlight that the four freshwater release estimates refer to different processes, and thus each simulation will represent the effect of a specific process in creating proxy anomalies of the 8.2 ka event: FWca represents the Canadian Plains routing event, FWul represents the effect of meltwater from the remaining LIS after its collapse, FWli represents the effect of the total freshwater addition to the ocean surrounding the 8.2 ka event (not accounting for routing events), and FWpe represents

the total early-Holocene meltwater from the LIS. By simulating these separately, we estimate the signature of each process on the $\delta^{18}O$ and SST records.

In our simulations, all freshwater was added to the Labrador Sea (50°N-65°N; 70°W-35°W). Meltwater from the LIS and Lake Agassiz are estimated to have had a $\delta^{18}O$ varying from -24‰ to -25‰ during the early-Holocene (Fisher et al., 1998; Remenda et al., 1994) ; we therefore added freshwater with a $\delta^{18}O$ of -25‰. Overturning in FWpe collapsed after 8 ka; to restart the North Atlantic deep convection smoothly a virtual salt flux decreasing from -0.2 Sv to -0.05 Sv (8 ka until 7.5 ka) with no isotopic signature was added.

VI.2.3.3 **Freshwater forcing of the hybrid scenarios**

In addition to this first set of simulations, which are based on earlier geological reconstructions and described in Section 6.2, we also integrated additional sensitivity simulations.

Twenty-four experiments were performed based on the uncertainty ranges of the Peltier (2004), Li et al. (2012), and Carlson et al. (2009b) estimates (Table 1). The 7.5 m in SLR equivalent estimated by Peltier (2004) was not fully released into the Labrador Sea. In turn, Li et al. (2012) estimated the date of the meltwater outburst within 8.245 ± 0.065 ka and their flux estimate has a 0.06 Sv uncertainty. Additionally, the Canadian continental basin routing event from Carlson et al., (2009b) likely contributed to an enhancement of freshwater flow to the Labrador Sea of 0.13 Sv lasting up to 300 years. Together, these result in potential freshwater fluxes varying between 0.046 Sv and 0.26 Sv and lasting between 200 and 1000 years. With these experiments, called “hybrid”, we test a more complex meltwater flux scenario, based on a

background freshwater forcing over a longer time period, a rerouting event and a shorter pulse, more intensive, drainage event. Both the magnitude of the meltwater fluxes (Part A), and their duration (Part B) are tested.

Tabela VI.1 - Publication's Table 1. Details of simulations used in this study. The reconstructions table (I) describes the meltwater volumes, fluxes and durations for the homogeneous forcing experiments described in Section 3. Experiments with hybrid freshwater forcing are separated into Part A and B (II and III). The long meltwater flux in the hybrid experiments in Part A have a fixed duration of 1000 years (9-8 ka), and the short flux is fixed at 130 years (8.31-8.18 ka). FW06 is the simulation in best agreement with proxy data in Part A, so the flux magnitudes of FW06 were used in Part B to test flux duration of the short flux. Note that FW06 is the same simulation as FW61. Volume (*) is in 10^5 km^3.

(I) Reconstructions				
Experiment	**Volume***	**Duration**	**Flow (Sv)**	**Reference**
FWpe	**27.1**	9 -8 ka	0.086	Peltier (2004)
FWca	**8.2**	8.5 - 8.2 ka	0.13	Carlson et al., (2009)
FWli	**5.3**	8.31 - 8.18 ka	0.13	Li et al., (2012)
FWul	**9.5**	8.2 - 7.6 ka	0.05	Ullmann et al., (2016)
Duration	**(II) Flux magnitude (Part A)**			
9-8 ka	**Sv**	**0.046**	**0.066**	**0.086**
8.31- 8.18 ka	**0.26**	FW10	FW11	FW12
	0.19	FW09	FW06	FW03
	0.13	FW07	FW04	FW01
	0.07	FW08	FW05	FW02
Flux	**(III) Flux duration (Part B)**			
0.066 Sv	**Duration**	**200 yrs**	**600 yrs**	**1000 yrs**
0.19 Sv	**300 yrs**	FW610	FW611	FW612
	130 yrs	FW67	FW64	FW61
	90 yrs	FW68	FW65	FW62
	50 yrs	FW69	FW66	FW63

Finally, a 2.5 SV freshwater flow to the Labrador Sea was added at year 8.47 ka in all simulations in order to simulate the Lake Agassiz outburst (Clarke et al., 2004). The exact date of the Lake Agassiz collapse is uncertain due to uncertainties on

reservoir ages of marine cores, which precludes further exploration of the date of the collapse in the simulations in this study.

VI.2.3 **Simulations based on earlier reconstructions**

The simulations presented in this section are based on different freshwater release processes that have been suggested in previous studies (Carlson et al., 2009; Li et al., 2012; Peltier, 2004; Ullman et al., 2016). FWpe simulates a scenario where the estimated LIS melting is released exclusively into the Labrador Sea (Peltier, 2004); FWca represents a scenario where the Canadian continental runoff discharges into the Labrador Sea (Carlson et al., 2009); FWul simulates the melting of the remaining LIS after the collapse of the Hudson Bay's ice saddle (Ullman et al., 2016), and FWli simulates a fast rise in sea level surrounding the 8.2 ka event due to prolonged drainage from Lake Agassiz (Li et al., 2012) (see methods, Section 6.2). SSTs and $\delta^{18}O$ anomalies from these simulations are then compared with proxy data from 27 locations, at the model's grid cell closest to the geographical coordinates of each core.

Linear regression slopes and RMSEs for simulated tracers (Fig VI.1) show that FWpe and FWca yield the best estimate of $\delta^{18}O_{sw}$ and $\delta^{18}O_{ice}$ (α_{sw}^{pe} =0.89, α_{sw}^{ca}=0.99, α_{ice}^{pe}=0.86, α_{ice}^{ca}=0.85). However, FWpe overestimates SST anomalies and estimates a decrease in δ18Oc while proxy records point to an increase during this period (α_{sst}^{pe}=1.43, α_{c}^{pe}=-0.4). The FWpe simulation represents the total amount of LIS melting during this period of time, however this flow did not go entirely into the Labrador Sea (Peltier, 2004). Thus, the overestimation of the SST response could be a result of an overestimation of the total freshwater forcing. Since the model calculates $\delta^{18}O_{sw}$ prognostically, and obtains $\delta^{18}O_{c}$ using a SST-based transfer function, the

misrepresentation of $\delta^{18}O_c$ is likely due to the SST overestimation. In turn, FWca yields the lowest RMSEs and best slopes across most tracers, with the exception of $\delta^{18}O_{sw}$. FWli and FWul have the lowest regression slopes (α_{all}^{ul} <0.3, α_{all}^{li} <0.5) and highest RMSEs of the four simulations.

The time series of the tracers confirm that FWpe overestimates both the long-term decrease in $\delta^{18}O$ prior to 8 ka (Fig VI.1b,f-i) and the cold SST anomalies (Fig VI.1c-e). Analysis of the $\delta^{18}O$ time series for the remaining simulations show the effect of each discharge in the early-Holocene proxy signal. The routing event in FWca reproduces most of the early-Holocene anomalies recorded between 8.5-8.3 ka, especially in the Labrador Sea SST and $\delta^{18}O_{sw}$ (Fig VI.1d,j), Gardar drift $\delta^{18}O_c$ (Fig VI.1h) and RAPiD core subsurface (Fig VI.1f). The magnitude of the short negative excursion in $\delta^{18}O_{ice}$ at 8.2 ka in the GISP2 record is also best reproduced by FWca when compared to the other simulations (Fig 1b). FWli also reproduces a sharp decrease in $\delta^{18}O_{ice}$ at 8.2 ka (Fig 1b), and in SST and $\delta^{18}O_{sw}$ at Gardar drift (Fig VI.1d,h), although it underestimates the magnitude of $\delta^{18}O_{ice}$ anomalies at 8.2 ka. Finally, the remaining melting of LIS after its collapse simulated in FWul reproduces the stable low $\delta^{18}O_c$ values at subsurface in the RAPiD core (Fig VI.1f).

Thus, simulated $\delta^{18}O$ shows that FWpe, FWca, FWli, and FWul reproduce different parts of the early Holocene signal. This suggests that a realistic freshwater flow for prompting the 8.2 ka event anomalies requires a combination of a long-term meltwater flux with a short-term flux intensification, possibly due to a change in routing of continental runoff and draining of Lake Agassiz (Meissner and Clark, 2006).

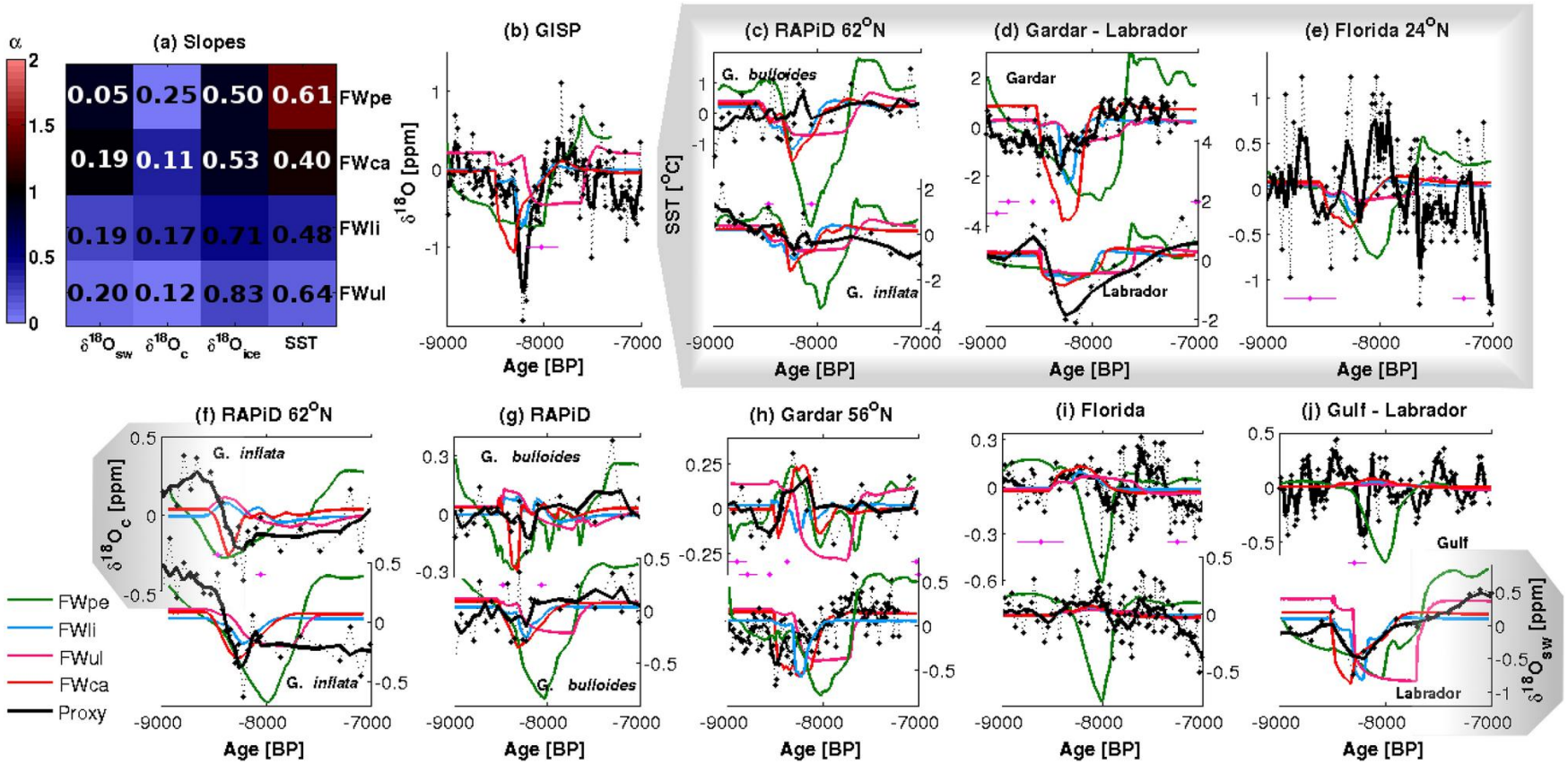

Figura VI.1 - Publication's Figure 1. Comparison between time series of proxies and simulations for $^{18}O_{sw}$, $^{18}O_{ice}$, $^{18}O_c$ and SST for RAPiD (c,f,g), Gardar Drift (d,h), Florida Strait (e,i), GISP and Gulf cores (b,j), and slopes and RMSEs (a) in all simulations (locations in Fig S1 and Table S1). Black dashed and full lines are core values and 2-point moving averages, respectively. Green, blue, magenta and red lines are time series for FWpe, FWli, FWul and FWca. The pink horizontal crosses are the dating (|) and dating errors (—) for the proxies. In (a) RMSE values are plotted in the center of the image while the colors of the squares indicate the values of the slopes. From f-j, top series are for $^{18}O_c$, while bottom series are for $^{18}O_{sw}$.

VI.2.4 **Hybrid simulations**

The simulations analyzed in this section (called hybrid hereafter) follow more complex freshwater release scenarios, testing the range of uncertainties in freshwater flux magnitude and duration as well as changes in freshwater forcing over time. In one set of the hybrid simulations (Table 1, Part A), the freshwater forcing is separated into two components: one lasts longer (1000 years background flux) with relatively low magnitudes (0.086 Sv, 0.066 Sv, and 0.046 Sv), while the other is shorter (130 year-long flux intensification) with relatively high magnitudes (0.13 Sv, 0.07 Sv, 0.19 Sv and 0.26 Sv). A comparison between the short fluxes in the Part A simulations (Fig VI.2a-d) shows that a flux intensification of 0.19 Sv achieves the lowest RMSEs in $\delta^{18}O_{sw}$, $\delta^{18}O_c$ and $\delta^{18}O_{ice}$ when compared with simulations with the same background flux but different short fluxes (Table S2). In turn, when comparing the long fluxes in the Part A simulations (Fig VI.2a-d, columns), it is noticeable that the simulations with 0.066 Sv of background flux have the lowest RMSEs and slopes closest to 1 for SST, $\delta^{18}O_c$ and $\delta^{18}O_{ice}$. Thus, the comparisons based on RMSEs and slopes suggest that a background flux of 0.066 Sv and a short flux of 0.19 Sv best represent the tracer anomalies (simulation FW06 - Table S2).

The Part B experiments were aimed at evaluating model sensitivity to the duration of the freshwater forcing. This was accomplished by adopting freshwater flux magnitudes from FW06, the experiment that best represented 8.2 ka event anomalies in Part A, and varying the durations of the individual phases of freshwater addition. The length of the shorter flux in this set of simulations varies from 50 years to 300 years, while the longer flux varies from 200 years to 1000 years (Table 1).

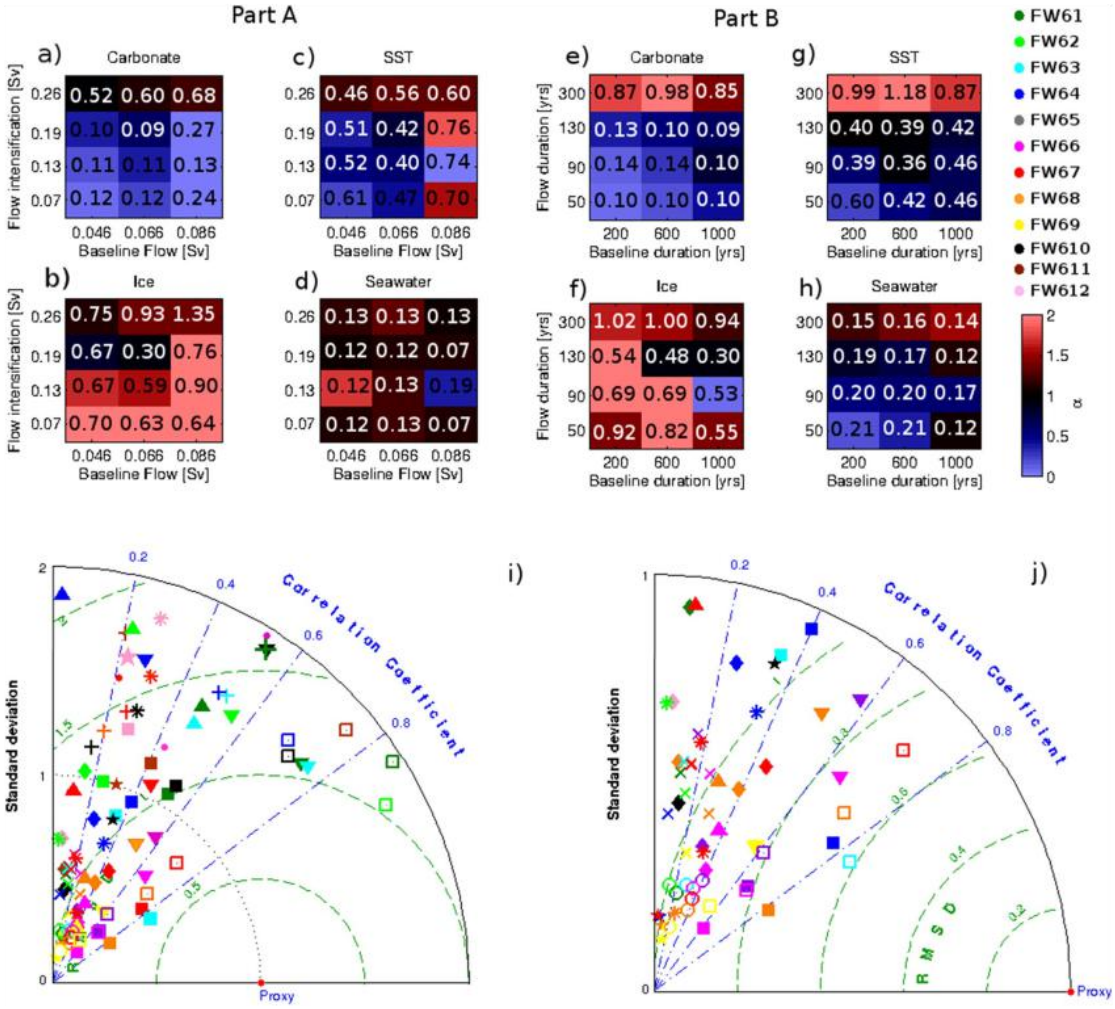

Figura VI.2 - Publication's Figure 2. Analysis of simulations in Table 1- Parts A and B. a to h are the slope and RMSE values for each experiment. Plots a-d are for experiments in part A, while plots e-h are for experiments in part B. The colour of the squares represents the slopes according to the color bar, and RMSE values are indicated in the center of each cell. i) Taylor diagram for comparison between proxy and simulated time series of ^{18}O anomalies: GISP ice core (■), Rapid Core $^{18}O_c$ in G. *inflata* (◆) and G. *bulloides* (+), Gardar Drift core $^{18}O_c$ for G. *bulloides* (●), Florida Strait core $^{18}O_c$ for G. *ruber* (X), Gulf core $^{18}O_c$ for G. ruber (★), Rapid Core $^{18}O_{sw}$ in G. *inflata* (*) and G. *bulloides* (▲), Gardar Drift core $^{18}O_{sw}$ (▼), Florida Strait core $^{18}O_{sw}$ (o), and $^{18}O_{sw}$ in Labrador Sea core (❑). The colors represent different simulations. Taylor diagram j is the same as i, but zoomed in closer to the 0. Standard deviations are normalized by the core value, while RMSE is centered.

Simulations FW61 and FW63 show the best match with proxy data with slopes closest to 1 and consistently low RMSEs (Fig VI.2e-h, Table S3). Further testing the

similarity between the simulated and core time series of $\delta^{18}O$ in a Taylor diagram allows for a more detailed comparison between simulations. All correlation values in the Taylor diagram are statistically significant ($p<0.05$, $n>1000$- Fig VI.2i, j). The highest correlations for $\delta^{18}O_{sw}$ are for the Labrador Sea cores and simulations FW61 (0.84), FW62 (0.88), and FW63 (0.83). In the Gardar Drift time series of $\delta^{18}O_{sw}$, FW61 and FW63 have the strongest correlation with the core (both 0.75), but the lowest RMSE value is achieved by FW66 (0.76‰). FW61 and FW63 also have the highest positive correlations for $\delta^{18}O_{sw}$ at the RAPiD core based on G. bulloides (0.47 and 0.48 respectively), for *G. bulloides* $\delta^{18}O_c$ in the RAPiD core (0.54 for FW61). According to the Diebold-Mariano test, RMSEs for FW61, FW63 and FW66 in $\delta^{18}O_c$ and $\delta^{18}O_{sw}$ are significantly different with confidence varying from 85% to 99%. The exceptions are $\delta^{18}O_c$ errors between FW61 and FW63, which are equal with 90% confidence. These results suggest that errors in $\delta^{18}O_{sw}$ for simulations FW61, FW63 and FW66 are statistically different and possibly not random. Simulations FW61, FW63 and FW66 are the ones that best reproduce $\delta^{18}O$ mean anomalies in most proxies and locations and have the best correlations and RMSEs for the whole time series. As a last step, and in an effort to determine the most realistic freshwater forcing, we will compare the time series produced by the three best fitting simulations with the proxy reconstructions at the six locations with high resolution data (Figure 3).

Simulated $\delta^{18}O_{sw}$ and $\delta^{18}O_c$ for FW61/62/63 at the location of the RAPiD core now capture the magnitude of proxy anomalies for *G. bulloides* (Fig VI.3f). FW61 and FW63 also reproduce the magnitude of the anomalies at the Gardar Drift core in the *G. bulloides* time series of $\delta^{18}O_c$ and $\delta^{18}O_{sw}$ (Fig VI.3g), and the SST time series at the RAPiD location (Fig VI.3b-top), and Gardar Drift (Fig VI.3c-top).

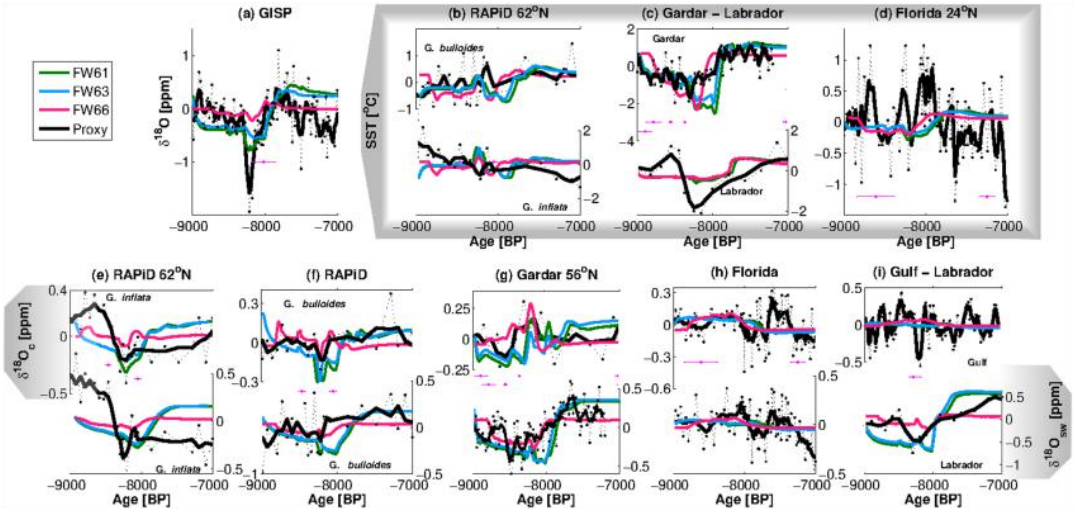

Figura VI.3 - Publication's Figure 3. Comparison of simulated and reconstructed $^{18}O_{sw}$, $^{18}O_c$, $^{18}O_{ice}$ and SST time series for the three best fitting hybrid models: RAPiD (b,e,f), Gardar Drift (c,g), Florida Strait (d,h), GISP $^{18}O_{ice}$ (a), Gulf Strait $^{18}O_c$ (i-top) and Labrador Sea $^{18}O_{sw}$ (i-bottom) and SST (c-bottom). Black dashed and full lines are core values and 2-points moving average. Green , cyan, and magenta lines show FW61, FW63, and FW66 simulations, respectively. The pink horizontal crosses are the dating (|) and dating errors (–) for the proxies.

GISP2 $\delta^{18}O_{ice}$ is best simulated by FW61, which reproduces both the long-term oxygen isotope decrease and the timing of the short-lived decrease at 8.2 ka (Fig. VI.3a-top). Neither simulated $\delta^{18}O_c$ in the Gulf of Mexico or SSTs in the Strait of Florida show significant variability (Fig VI.3d,h and Fig VI.3i-top). Taking into account that FW61 exhibits the best match to SST and $\delta^{18}O$ in the proxy record, while also reproducing the GISP2 $\delta^{18}O_{ice}$, we conclude that this simulation is the best representation of the 8.2 ka event in our study.

VI.2.5 **Discussion**

Our first set of simulations evaluate how well different freshwater sources to the North Atlantic reproduce ocean anomalies associated with the 8.2 ka event. Although

FWca represents only one of these sources, i.e., a runoff routing event (Carlson et al., 2009), it yields the lowest RMSEs, best slopes and the best representation of most cores time series. This points to the routing event being one of the main contributors to the changes captured by the proxies during the early Holocene. Given that the regression slopes for FWul are significantly lower than for FWca, melting of the remaining LIS after its collapse (FWul) likely only played a background role in creating the climate anomalies at the 8.2 ka, while the routing event (FWca) had much more impact.

We then conducted several additional meltwater flux experiments in order to answer the following question: What magnitudes and rates of freshwater fluxes are most consistent with the 8.2 ka event proxy anomalies? The short 8.2 ka event anomalies recorded in $\delta^{18}O$ climate archives are best reproduced with a simulation forced by a freshwater flux intensification of 0.19 Sv lasting for 130 years. This is in line with earlier simulations performed with the Community Climate System Model version 3, which reproduced the 8.2 ka SST anomalies with 0.13 Sv of freshwater discharge for 99 years (Wiersma et al., 2006). Here, we show that a higher discharge estimate of 0.19 Sv embedded in a background flux of 0.066 Sv is able to reproduce $\delta^{18}O$ anomalies in addition to SST anomalies.

Based on 35 $\delta^{18}O$ and SST records from 27 different locations, we consider that our FW61 simulation was able to accurately reproduce the major trends and anomalies recorded in the proxy records for the 8.2 ka event and early-Holocene (Fig VI.3). The FW61 simulation suggests that anomalies similar to those associated with the event could have been caused by a total meltwater addition of 7.5 m in SLR equivalent between 9-8 ka, with a short period of intensified flooding, equivalent to a SLR of 2.2 m (included in the 7.5m estimate), between 8.31-8.18 ka (Fig VI.4a,b, Fig S2). This short

intensification of the freshwater flux in FW61 has similar magnitude as the relative SLR in Southwest Scotland (1.45 m within 300 and 500 yrs) (Lawrence et al., 2016), but the absolute value for our estimate is 0.75 m higher. This discrepancy could be explained by either local land uplift due to glacial isostatic adjustment over Scotland (Bradley et al., 2011), or by a combination of LIS melting and Canadian basin routing, since the routing would not contribute to eustatic SLR. The intensification in freshwater input of 2.2 m also matches previous eustatic SLR estimates from the Netherlands (3 ± 1.2 m within 200 yrs) (Hijma and Cohen, 2010) and Mississippi delta (0.8-2.2 m within 130 yrs) (Li et al., 2012). Estimates of SLR rates on longer time-scales for the early-Holocene however differ considerably from ours. Rates of 17.9 mm yr^{-1} (8600 - 7100 BP), and 24 mm yr^{-1} (extending up to 8948-8206 BP) are recorded on the coast of Germany (Streif, 2004) and Norway (Smith et al., 2013), much higher than our 7.5 mm yr^{-1} estimate. Because the melting of Antarctic Ice Sheet contributed to less than 3 cm of SLR in early-Holocene (Fisher et al., 1998), this difference in meltwater fluxes likely derives from LIS additional melting. This is expected since the meltwater volume in this study is an estimate of the meltwater that was added to the Labrador Sea, part of which was then advected to deep water formation sites, thus affecting large-scale ocean circulation and climate. Additionally, meltwater from the LIS in the early-Holocene was discharged into wide regions in the Arctic and North Atlantic and thus account for a total volume higher than the one we find here (Peltier, 2004). Therefore, our estimate does not represent the total LIS melting and corresponding SLR for this time span. Neither FW61 nor the proxy records show a clear 8.2 ka response in the Florida Strait (SST). The 8.2 ka event might therefore not have had a significant and far-reaching impact on the Florida Strait region, causing a climate response within model or proxy

data background variability. A simulation of the 8.2 ka event with the Hadley Centre Coupled Model, version 3 (HadCM3) also did not reproduce any measurable SST anomalies in the Gulf of Mexico (Matero et al., 2017), thus suggesting that the core SST signal in that location is likely not due to meltwater forcings involved in the 8.2 ka event. The AMOC response to the 8.2 ka freshwater forcing is still debated in the scientific community. In our best-fitting FW61 simulation, AMOC weakens by 62% (13 Sv, Fig 4b) without collapsing, supporting earlier evidence of substantial AMOC weakening without a collapse during the 8.2 ka event (Kleiven et al., 2008; LeGrande et al., 2006). Matero et al. (2017) find that AMOC weakens by 55% of its initial overturning, similar to our estimate, based on simulations with the HadCM3.

VI.2.6 **Implications**

The magnitude of the simulated climate change during the 8.2 ka event offers a pertinent reference point for future climate trends (Schmidt and Legrande, 2005). The Greenland Ice Sheet is undergoing considerable melting and this is likely to continue well into the future (Fettweis et al., 2017; van den Broeke et al., 2016). Greenland melting scenarios for the next millennium project SLR of 7.28 m for the RCP8.5 scenario of the Intergovernmental Panel on Climate Change (Aschwanden et al., 2019). Current meltwater fluxes from the Greenland Ice Sheet are estimated to be ~0.005 Sv (van den Broeke et al., 2016). Even though this flux is considerably smaller than the ones used in our experiments, projections of freshwater flux intensification for the next centuries are similar to the FW61 baseline flows. For example, Golledge et al. (2019) found an increase in freshwater flux from Greenland ice-sheet melting of 0.015 Sv by

2100 in the RCP8.5 scenario. Lenaerts et al., (2015) project an acceleration of the meltwater flux from Greenland up to 0.08 ± 0.003 Sv by 2200, while the maximum melting scenario of Aschwanden et al., (2019) projects a flux exceeding 0.17 Sv by 2300 (15 mm of SLR yr^{-1}). Bakker et al. (2016) found a median discharge higher than 0.08 Sv by the year 2300. The projected input of freshwater into the North Atlantic associated with the RCP8.5 scenario is therefore of the same magnitude as those in the FW61 simulation in terms of total SLR contribution (7.5 m), duration (1000 years) and flux magnitude (0.066 Sv to 0.19 Sv).

However, it is important to highlight that future emission scenarios also include intensive surface radiative warming, which will add to the stratification effect and thus intensify the future overturning weakening (Weaver et al., 2012). Additionally, future GIS meltwater will likely flow into the coastal areas surrounding the ice sheet, instead of exclusively into the Labrador Sea (Aschwanden et al., 2019), and thus, its impact on the ocean overturning will potentially differ from the focused meltwater injection in the Labrador during the 8.2 ka event. Moreover, the climate response to an increase in meltwater will be in addition to the much greater warming response due to increasing greenhouse gas concentrations, as well as changes due to topography and albedo changes over Greenland. Nevertheless, the estimated meltwater flux from the GIS in the not too distant future is comparable to the fluxes we find as the forcing behind the 8.2 ka event.

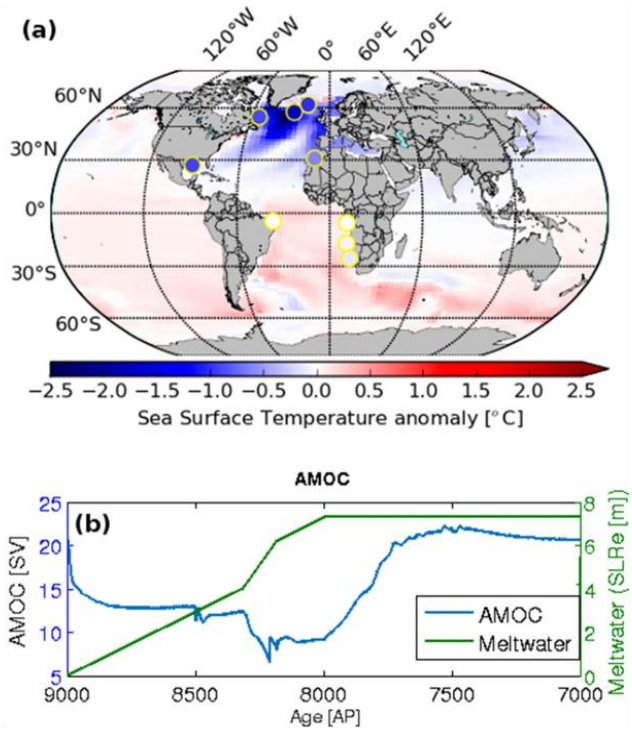

Figura VI.4 - Publication's Figure 4. Climate impacts for the hybrid simulation FW61. (a) Proxy and model SST anomalies for the FW61 simulation. The color of the circles is plotted according to the anomaly value of the reconstructed SSTs. (b) Simulated maximum overturning streamfunction for the North Atlantic as a measurement for the Atlantic Meridional Overturning Circulation (right, blue line), and meltwater added in the FW61 experiment, in Sea Level Rise equivalent (SLRe, green line). Map (a) drawn by Wilton Aguiar on Python v2.7 (https://www.python.org/download/releases/2.7/)

VI.2.8 **Acknowledgments, Samples, and Data**

This work is a part of the activities from the Brazilian High Latitudes Oceanography Group (GOAL) and the Brazilian National Institute of Science and Technology of the Cryosphere (INCT-CRIOSFERA; 573720/2008-8, 465680/2014-3, FAPERGS 17/2551-0000518-0). The GOAL is currently funded by the Brazilian Antarctic Program (PROANTAR) through the Brazilian Ministry of the Environment (MMA), the Brazilian Ministry of Science, Technology, Innovation and Communication (MCTIC), and the Council for Research and Scientific Development of Brazil (CNPq;442628/2018-8, CAPES AUXPE 1995/2014). W. Aguiar acknowledges the financial support from the CAPES Foundation, and the Fulbright association for promoting the scientific interchange required by this work. M. M. Mata acknowledges CNPq grant nos. 306896/2015-0. K. J. Meissner acknowledges funding from the

Australian Research Council (DP180100048, DP18012357). L. Prado acknowledges the INCT-CRIOSFERA (88887.495715/2020-00), and I. Wainer acknowledges the São Paulo Research Foundation (2018/14789-9; 2019/08247-1) and CNPq (300970/2018-8). All authors acknowledge Dr. James Scourse for the valuable review.

VI.2.11 **Data Availability**

Simulated data for this research is available in the Zenodo database (https://doi.org/10.5281/zenodo.4282563) and by contact to the first author. The core data used is available in these in-text data citation references: Morrill et al., (2005)10, Peltier (2004)29, Carlson et al. (2009)14, Li et al. (2012)21, Ullmann et al. (2016)17. Remaining data not present in these sources are available in the supplementary material.

Capítulo VII: Respostas climáticas no Atlântico Sul e América do Sul durante o 8,2 ka AP

Este capítulo traz o segundo artigo científico publicado a partir desta tese, de autoria de Wilton Aguiar, Luciana Prado, Ilana Wainer, Zhengyu Liu, Alvaro Montenegro, Katrin J. Meissner e Mauricio M. Mata é intitulado *"**Freshwater forcing control on early-Holocene South American monsoon**"* e encontra-se publicado no periódico *"Quaternary Science Reviews"*, volume 245 (2020), e pode ser acessado em: https://doi.org/10.1016/j.quascirev.2020.106498.

VII.1 Síntese do capítulo

Previsões da evolução climática do planeta em diferentes cenários de aumento de concentração de dióxido de carbono atmosférico apontam que a AMOC provavelmente sofrerá uma desaceleração no século 21. Portanto, entender a resposta da América do Sul para eventos de desaceleração da AMOC em períodos interglaciais torna-se extremamente importante para se poder prever as consequências climáticas da

futura desaceleração da AMOC. O evento de 8,2 ka, por ser o último evento de desaceleração da AMOC registrado em *paleoproxies* é um estudo de caso ideal para tal tipo de análise. No entanto, existe uma grande incerteza na expressão climática do evento 8,2 ka AP no Hemisfério Sul. Isto se deve, especialmente, à escassez de reconstruções climáticas de alta resolução temporal no Hemisfério Sul durante o Holoceno. Este capítulo propõe-se então a entender qual a expressão climática do 8,2 ka no Atlântico Sul e na América do Sul através de uma análise *multiproxy* e de simulações do sistema terrestre.

A análise *multiproxy* feita neste capítulo demonstra que o Atlântico Sul desenvolveu uma tendência à fase negativa do SASD como resposta à descarga de água doce no hemisfério norte entre 9 e 8 ka AP. Este dipolo negativo então foi capaz de intensificar o SAMS, através de um aumento da intensidade de precipitação no nordeste do Brasil. Os padrões de SST gerados pelo SASD negativo foram capazes de explicar até 50% da variância na precipitação devido ao SAMS, sendo um mecanismo secundário, porém importante na modulação da precipitação continental na América do Sul. Adicionalmente, o capítulo propõe um mecanismo de controle do SASD pela AMOC, através da modulação dos ventos alísios sobre a profundidade das isotermas no Atlântico Sul.

Este capítulo complementa os resultados inovadores de Wainer et al., (2014), que demonstraram uma forte influência do SASD sobre o SAMS durante o início do Holoceno.

VII.2 Artigo científico 2

Freshwater forcing control on early-Holocene South American Monsoon

Wilton Aguiar[a], Luciana F. Prado[b], Ilana Wainer[c], Zhengyu Liu[d], Alvaro Montenegro[d], Katrin J. Meissner[e], Mauricio M. Mata[a]

[a] *Laboratório de Estudos dos Oceanos e Clima, Instituto de Oceanografia, Universidade Federal do Rio Grande – FURG. Rio Grande, RS, 96203-900, Brazil*
[b] *Instituto de Geociencias,Universidade de Brasilia, Campus Darcy Ribeiro, Brasilia, Distrito Federal, 70910-900, Brazil*
[c] *Instituto Oceanografico da Universidade de Sao Paulo, Sao Paulo, 05508-120, Brazil*
[d] *Atmospheric Sciences Program, Department of Geography, The Ohio State University, Columbus, Ohio*
[e] *Climate Change Research Center, University of New South Wales, Sydney, Australia*

Abstract

Climate anomalies due to Lake Agassiz outbursts and Hudson Bay ice dome melting are commonly considered triggers of North American atmospheric cooling. However, in the Southern Hemisphere, these freshwater fluxes are mostly associated with increased precipitation and a possible intensification of the South American Monsoon System (SAMS). Here, we tested how the SAMS responded to early-Holocene meltwater events. Based on both proxy data and simulations, we find that sea surface temperatures (SSTs) and precipitation indicate a freshwater-driven strengthening of the SAMS due to a weakening of the South Atlantic subtropical dipole. Simulated SAMS strengthening accounts for up to 50% of the variance in early-Holocene precipitation in South America. In turn, changes in the South Atlantic Subtropical Dipole accounts for up to 31% of the variance in South Atlantic SSTs. Additionally, we propose that the stronger SAMS in the early Holocene might have been due to a freshwater-driven weakening of the southeasterly trade winds. Slower trade winds weaken the zonal and meridional surface water transport, concentrating warm waters in the northeastern South Atlantic.

Keywords: 8.2 ka event, Lake Agassiz, SAMS, SASD, Early Holocene

Email address: aguiar.wilton@gmail.com (Wilton Aguiar)

1. Introduction

The transition from the early to the middle Holocene (11.7 ka to 4.2 ka) is characterized by the final collapse of North American ice sheets and the reorganization of the North Atlantic freshwater budget (Walker et al., 2012, 2018). An orbitally forced increase in the summer insolation is thought to have accelerated Laurentide Ice Sheet melting (Kaufman et al., 2004; Jansen et al., 2008; Bartlein et al., 2011), resulting in instability and the eventual outburst of proglacial Lakes Agassiz and Ojibway at approximately 8,200 calendar years before the present (Clarke et al., 2004, 8.2 ka). Because freshwater anomalies in the North Atlantic trigger disruptions in the Atlantic meridional overturning circulation (AMOC), the large increase in lake discharges in 8.2 ka is an important component of early-Holocene climate anomalies. Widespread evidence points to diminished North Atlantic deep convection (Oppo et al., 2003; Hall et al., 2004) and AMOC weakening during the 8.2 ka event and early Holocene (Ellison et al., 2006; Kleiven et al., 2008), but uncertainties still exist regarding the propagation, intensity, timing, and spatial extent of the climate anomalies associated with the weakening of the overturning.

In the Northern Hemisphere, the 8.2 ka event is associated with widespread cold and dry conditions over North America and Europe and drier conditions over Africa and central Asia (Alley and Ágústsdóttir, 2005). Proxy data coming mostly from the northern tropical Atlantic and Western Asia indicate a decrease in the tropical precipitation associated with the 8.2 ka event (Morrill and Jacobsen, 2005). Southern Hemisphere proxy data link the 8.2 ka event to spatially heterogeneous temperature anomalies (Morrill et al., 2013) and anomaly signals in particular areas such as stronger precipitation areas over Madagascar (Voarintsoa et al., 2019) and accelerated sea-level rise and high sediment deposition rates along the Brazilian shelf (Boski et al., 2015; dos Santos-Fischer et al., 2018).

Proxy-based anomalies from South America and the South Atlantic covering the period of interest are scarce. Multiproxy reconstructions (Morrill et al., 2013) and speleothem records (Cheng et al., 2009) associate the 8.2 ka event with increased precipitation over South America. There are indications of a sharp transition from a cooling to a warming trend centered at the 8.2 ka event in the western subtropical South Atlantic sea surface temperatures

(SSTs) (Pivel et al., 2013). Like most Southern Hemisphere reconstructions, the above studies describe regional responses to the 8.2 ka event. Impacts at broader spatial scales have been connected to a strengthening of South American precipitation in speleothems and attributed to the South American monsoon system (SAMS) in the early Holocene (Cheng et al., 2009). The SAMS is one of the most important large-scale features of South America (Carvalho and Cavalcanti, 2016). In a strong SAMS regime, precipitation during austral summer increases along the Intertropical and South Atlantic Convergence Zones due to increased moisture transport (Kodama, 1992; Nieto-Ferreira and Rickenbach, 2011). The interannual variability of the SAMS is associated with the El Niño–Southern Oscillation and with the South Atlantic subtropical dipole (SASD) since those patterns induce anomalies in the wind circulation and moisture delivery to South America. (Venegas et al., 1996, 1997; Nogués-Paegle and Mo, 1997). More details on the SASD can be found in the supplementary material.

A reconstruction of the SASD has been used in conjunction with modeled precipitation to suggest an SASD-induced enhancement of the SAMS during meltwater events in the early Holocene (Wainer et al., 2014). Although the SASD signal evaluated by Wainer et al. (2014) has longer timescales than expected for the Lake Agassiz outburst, other longer-lasting freshwater fluxes in the early Holocene, such as the melting of the Hudson Bay ice dome (Gregoire et al., 2012) and rerouting of Canadian river discharge (Carlson et al., 2009), could have affected the South Atlantic in the same manner.

Here, we test the proposed relationship between the SASD, the SAMS, and precipitation over South America for the early-Holocene and evaluate the potential link between freshwater forcing from the 8.2 ka event and the SASD. Given the paucity of proxy information from the South Atlantic and South America during the period of interest, our analysis will be based on both numerical simulations and proxy data. More specifically, we plan to answer the following three questions: (1) Does the spatial pattern of reconstructed South American precipitation points to a strengthening of the SAMS around 9-8 ka? (2) Was the Early Holocene SASD shift caused by freshwater addition in the North Atlantic, i.e., a warmer northeastern South Atlantic, and if so, (3) what was the chain of mechanisms by which the increase in the freshwater discharge in the North Atlantic generated a negative trend in the SASD and strengthened the SAMS during the 8.2 ka event? This paper will be structured in the following manner to address these questions: the next section describes the proxy data, simulations and methods. Section 3 dis-

cusses the proxy-based SASD and precipitation signal. Section 4 compares the proxy data to the simulations to evaluate their ability to reproduce the SASD and South American precipitation record during the period of interest. Section 5 analyzes the temporal evolution in the AMOC and sea ice extent in the simulations. Section 6 discusses the SASD and bipolar seesaw states, and Section 7 analyzes the mechanisms of the SASD shift. Section 8 discusses the SST and wind anomalies between the AMOC slowdown and restart phases. Finally, in Section 9, we summarize the discussion and answer the questions raised in the introduction based on our results.

2. Data and Methods

2.1. Climate Reconstructions

Five SST proxy records were used to generate an early-Holocene-reconstructed SASD (Fig 1a). The westernmost records were LaPAS-KF02 and SAN-76 located at 25^o50'S 45^o12'W at a depth of 827 m and 24^o25'S 42^o16'W at a depth of 1682 m, respectively (Toledo, 2008; Pivel et al., 2013). The easternmost cores used were ODP 1084B at 25^o30'S 13^o1'E and a depth of 1992 m, GeoB1023-5 at 17^o9'S 11^o0'E and a depth of 1978 m, and ODP 1078C at 11^o55'S 13^o24'E and a depth of 426 m (Kim et al., 2002, 2003; Farmer et al., 2005). The SASDrec index is reconstructed based on the difference in the mean SST anomalies between the eastern and western cores in an approach similar to that used in Wainer et al. (2014). The South American speleothem records include the Padre (Cheng et al., 2009) and Lapa Grande tropical caves (Stríkis et al., 2011) and the Botuverá (Bernal et al., 2016) and Jaragua subtropical caves (Novello et al., 2017). All the registers were calibrated using the most recent continental and oceanic isotopic curve based on a Monte Carlo approach.

2.2. Early Holocene CCSM3 simulations

To derive the early-Holocene SASD variability, we used one fully transient and one equilibrium simulation generated by the Community Climate System Model, version 3. The first is the simulation of the transient climate evolution over the last 21,000 years (TrACE21ka) (He, 2011). TrACE21ka has a latitude-longitude resolution of approximately 3.75^o, without flux adjustments and with a dynamic global vegetation module. Starting from the initial conditions of the last glacial maximum (Otto-Bliesner et al., 2006), the simulation is forced with transient orbital parameters and greenhouse

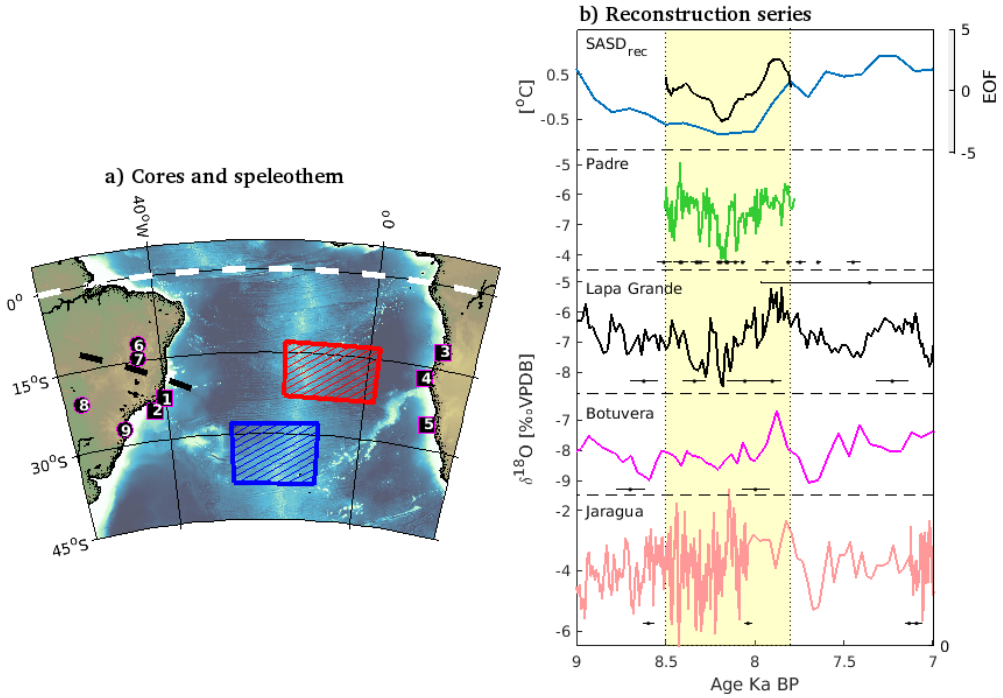

Figure 1: Speleothem $\delta^{18}O$ records for South America and the proxy-based SASD reconstructions. a) Location of the marine sediment cores (squares: 1-SAN76, 2-LaPASKF02, 3-ODP1078C, 4-GeoB10235, and 5-ODP1084B) and the speleothems (circles: 6-Padre, 7-Lapa Grande, 8-Jaragua, and 9-Botuverá). The dashed lines illustrate the locations of the Intertropical (white - -) and South Atlantic Convergence Zones (black - -), based on mean climatological position (Pottapinjara et al., 2019; Zilli et al., 2019). The red and blue boxes show the northeast and southwest SASD poles, respectively. b) The blue line at the top is the proxy-based SASD reconstruction, and the black line is the sum of the 1^{st} and 2^{nd} speleothem EOFs. The speleothem $\delta^{18}O$ time series are in VPDB. Age error bars for each speleothem are presented in the horizontal box plots.

gases (Joos and Spahni, 2008), ICE-5G ice sheet reconstructions (Peltier, 2004), and meltwater forcing based on Clark and Mix (2002). To simulate early-Holocene rerouting of continental runoff, a freshwater forcing of 7.47 m/kyr in the equivalent sea level was added to Hudson Bay between 9-8 ka. Additionally, the lake outburst is simulated by adding 5 Sv (438 m/kyr) of freshwater to Hudson Bay over a time span of six months at 8.47 ka AP (Carlson et al., 2009; Clarke et al., 2004).

A second simulation analyzes the effect of the Lake Agassiz outburst and Hudson ice dome melting on a climate state in equilibrium, also using the Community Climate System Model, version 3. The simulation was equilibrated with the 8.5 ka orbital parameters (Berger, 1978) and greenhouse concentrations corresponding to $[CO_2] = 260ppm, [CH_4] = 660ppb$ and $[N_2O] = 260ppb$, with a 1^o resolution. To simulate the Hudson Bay ice dome melting, a freshwater forcing of 0.13 Sv was added to the Labrador Sea within the first 99 years of simulation, while in year 1 a 2.5 Sv flux was added to simulate the lake outburst (Clarke et al., 2004). After 100 years, the simulation proceeds without any additional flux for 50 years. In contrast to TrACE21ka, this simulation compresses the 1 kyr ice dome melting to 100 years; however, previous studies show that this temporal compression of the freshwater flux does not cause significant changes in the 8.2 ka SST signal (Wagner et al., 2013; Morrill et al., 2014). In both simulations, freshwater forcing is applied to the Labrador Sea, and the 8.2 ka and early-Holocene SST and precipitation signals have been previously validated by comparison with proxy records (He, 2011; Wagner et al., 2013; Morrill et al., 2014).

2.3. UVic Model Simulation

An additional simulation was performed using the isotope-enabled University of Victoria Earth System Climate Model, version 2.9 (Brennan et al., 2012, UVic model). The UVic model is also fully coupled with ocean, land surface, atmosphere, vegetation, sea ice, and sediment components and does not include flux adjustments (Weaver et al., 2001). The model was forced with a present-day wind reanalysis by the National Center for Environmental Prediction (Kalnay et al., 1996). Time-varying geostrophic wind anomalies are computed and added to the climatology to allow dynamic feedback (Weaver et al., 2001). The Modular Ocean Model - Version 2 is the ocean component. It has 19 vertical levels with Δz varying from 50 m at the surface to 500 m at the deepest level and a resolution of 3.6^o longitude by 1.8^o latitude (Pacanowski, 1996). The model also includes sea ice (Hibler, 1979),

sediment (Archer, 1996), land surface, dynamic vegetation components and fully prognostic $\delta^{18}O$ for the ocean, atmosphere, sea ice and land (Meissner et al., 2003; Brennan et al., 2012, 2013; Bagniewski et al., 2015, 2017).

The orbital parameters and carbon dioxide concentration chosen for the simulation refer to 9 ka (i.e., eccentricity=0.0167, obliquity=23.45^o, longitude of perihelion=102.04^o, and $[CO_2] = 280ppm$) (Berger, 1978). A ten-thousand-year-long equilibrium simulation was performed to guarantee that both the ocean circulation and ocean tracers are in full equilibrium. Hence, the last 2 kyrs of the equilibrium simulation consist of the control output. The freshwater forcing scheme is implemented from the last control year. To simulate the Laurentide Ice Sheet melting and rerouting of Canadian continental runoff, 0.086 Sv of freshwater was added to the Labrador Sea (50^{o}N-65^{o}N, 70^{o}W-35^{o}W) for one thousand years (Carlson et al., 2009, 9-8ka AP). Finally, to simulate the Lake Agassiz outburst, 2.5 Sv of freshwater forcing was added to the same Labrador Sea area in 8.5 ka (Clarke et al., 2004). In the real world, both discharges would have drained into the Hudson Bay; however, due to the rigid-lid approximation, the addition of freshwater had to be spread over a large area to avoid instabilities. After 8 ka, a virtual salt flux was added over the same region in the Labrador Sea to restart the North Atlantic deep convection. The virtual salt flux decreased from -0.2 SV to -0.05 SV between 8 and 7.5 ka. This virtual salt flux has no isotopic signature and was chosen so that the overturning could be restarted smoothly.

2.4. SASD, bipolar seesaw and wind effect analysis

The effect of the bipolar seesaw on SST anomalies was analyzed based on the first empirical orthogonal function (EOF) of the Atlantic SSTs. Since the surface signal of the bipolar seesaw is directly affected by the strength of the AMOC overturning (Pedro et al., 2018), an AMOC index, i.e., the maximum overturning streamfunction between 20^{o}N-70^{o}N and between 200 and 3000 m, was calculated as in (Yang et al., 2015). The total sea ice area was also calculated for the models due to its effect on global SST patterns and deep water formation (Chiang and Bitz, 2005). To analyze the SASD variability in the early Holocene, we calculated the model-based SASD index in two ways. First, the SASD$_{\text{MODEL}}$ area index was obtained by calculating the difference in the SST anomalies between the southwest (30^o-40^{o}S, 30^o-10^{o}W) and northeast (15^o-25^{o}S, 0^o-20^{o}W) areas of the dipole region(Morioka et al., 2011). Hence, SASD$_{\text{MODEL}}$ measures the rate of warming (or cooling) between the South Atlantic poles, with a negative SASD$_{\text{MODEL}}$ meaning

stronger warming in the northeast South Atlantic or stronger cooling in the southwest South Atlantic, and vice versa (Lorenz, 1956; Morioka et al., 2011, Figure C.3). Since the core-based SASDREC is the difference between coastal temperatures, we calculated SASDCOAST, which takes the difference in SST anomalies at the coastal cells of each model within the latitude range of each pole of the SASDMODEL index. SASDMODEL is calculated following the definition of the SASD index by Morioka et al. (2011), but the addition of SASDCOAST assures comparability with SASDREC.

Vertical displacement of the thermocline along longitudes can be triggered by either wind action or horizontal water mass advection into the South Atlantic. Specifically, shifts in the meridional component of the winds change the zonal surface Ekman transport and rearrange the zonal SST distribution. Using the 1.5 layer model and Ekman dynamics, we are able to derive how changes in the trade winds affect the thermocline depth (Eq. 1).

$$h^2(x,y) = \frac{2f^2(y)}{\beta(y)\gamma} w_e(x - x_e) + H^2(y) \tag{1}$$

where $h(x,y)$ is the predicted isothermal depth as a function of the longitude (x) and latitude (y). $H(y)$ is the depth of the chosen isotherm in the eastern boundary, and $D(x,y) = \sqrt{\frac{2f(y)^2}{\beta(y)\gamma} w_e(x - x_e)}$ is the increment of the isothermal depth over the basin. The variables $(x - x_e)$, w_e and $\gamma = \frac{\rho_3 - \rho_2}{\rho_0} g$ are the distance from the eastern boundary, Ekman pumping and density stratification, respectively. The values chosen for ρ_2 (1025 kg m^{-3}) and ρ_3 (1035 kg m^{-3}) represent the approximate mean densities above and below the thermocline, respectively. $\rho_0 = 1020$ kg m^{-3} is a reference density. Finally, $f(y)$ is the Coriolis parameter, and $\beta(y)$ is the beta effect parameter. The parameter that tracks the vertical displacement of the isotherms along the longitudes ($D(x,y)$) depends on Ekman pumping changes. Hence, $h(x,y)$ measures how wind changes affect a specific isotherm. Although the 20^{o}C isotherm is traditionally used to track thermocline depth, this isotherm emerges north of 35^{o}S in both simulations, i.e., north of the maximum latitudinal extent of the SASD. We therefore chose to track the 17^{o}C isotherm, which lies close to the top of the thermocline. The full derivation of Eq. 1 is found in the supplementary material. Finally, wind patterns also respond to sea ice alterations. Sea ice expansion may intensify trade winds (Chiang and Bitz, 2005). As sea ice changes influence Antarctic Bottom Water and North Atlantic Deep Water formation, we also analyze simulated sea ice areas (SIAs).

3. Precipitation and SASD records

First, we analyzed the SASD and SAMS signals in ocean cores and precipitation. The reconstructed SASDREC index shows a decrease in the dipole between 9 and 8 ka by up to 1°C, followed by an increase after 8 ka (Fig 1). A negative SASD index is associated with anomalous warming of the northeast South Atlantic, which in turn enhances the SAMS by increased evaporation (Liebmann and Mechoso, 2011). Precipitation over South America is mediated by convergence and convection over the ITCZ and SACZ (Garcia and Kayano, 2010; Souza and Cavalcanti, 2009). However, intensified evaporation in the northeast South Atlantic during negative SASD events enhances water vapor saturation over the convection bands, strengthening the precipitation (Monerie et al., 2019; Wainer et al., 2014). The spatial footprint of a strong SAMS is an increment in the precipitation along northeast South America (Vera et al., 2006), with this increment decreasing from the north towards southernmost South America (Fig C.3 - supplementary). Speleothem $\delta^{18}O_p$ records along South America can help us determine if, in fact, an increase in the precipitation signal is recorded between 9-8 ka. Lapa Grande and Padre speleothem reconstructions register a decrease in $\delta^{18}O_p$ from 9-8.2 ka, pointing to an increase in precipitation in this period (Fig 1). In both caves, $\delta^{18}O_p$ increases after 8.2 ka, pointing to a decrease in precipitation. Conversely, an SASD negative event decreases the SST over the southwestern South Atlantic. This decrease in SST counter-balances the stronger evaporation in the northeast South Atlantic, which then causes the precipitation signal to decrease southwards (Liebmann and Mechoso, 2011). Jaragua Cave is located south of the previous speleothems. As expected for southern South America, there is a minimal $\delta^{18}O_p$ decrease between 8.5-8.3 ka and an increase after 8.3 ka. Botuverá cave is the southernmost speleothem considered in this study. Since the SAMS has a lowering effect on southern South America precipitation, if the recorded changes in the precipitation are due to changes in the SAMS, we would expect very small or no precipitation variation in this record. In fact, the Botuverá speleothem shows no significant changes in $\delta^{18}O_p$ except for a slight increase (precipitation decrease) between 8.2 ka and 7.9 ka. The decrease in the precipitation variation from northeastern to southern South America is an indication of SAMS-driven precipitation events. Notice also that the SASDREC index is correlated with $\delta^{18}O_p$ changes recorded in the caves, implying the influence of the SASD pattern on the SAMS.

EOF analysis was performed for the Padre, Lapa Grande, Botuverá and Jaguara Caves within their maximum gap-free time range (8.5 ka - 7.8 ka, the yellow band in Fig 1b). The sum of the first and second components show a decrease in $\delta^{18}O_p$ from 8.5-8.2 ka and explains 89% of the total speleothem record variability (Fig 1b - top). The maximum cross-correlation of the sum of the EOFs with the reconstructed SASD equals 0.83 (nPREC=231,unfiltered), with an SASD lag of 21 years, which indicates the coevolution of those patterns. Although this lag is large considering the real world SST-precipitation coupling, one has to bear in mind that the dating error for the marine records used here is up to 60 years (Pivel et al., 2013). Still, the 21 years lag is in agreement with the time scale of the response of the global monsoons to a change in the South Atlantic meridional heat transport estimated by Lopez et al. (2016).

The synchronous signal in the reconstructed SASD and speleothem $\delta^{18}O_p$ hints that the change in precipitation in the early Holocene is tied to the recorded change in the SASD. Moreover, due to the scarcity of early-Holocene precipitation and SST reconstructions, climate model simulations can be a helpful tool to further explore the connection between the SASD and SAMS.

4. Simulated SASD signal

Prior to analyzing the early-Holocene simulations, it is necessary to test whether they reproduce the SASD and precipitation signals described in Section 3. We therefore compare SASDREC with the simulated SASDCOAST value and the speleothem $\delta^{18}O_p$ with the simulated precipitation. SASDREC is created by taking the difference in the SST anomalies between records in the coastal cores. Because the coastal gradients may differ from open-ocean ones, we calculated the difference between the SST anomalies off the African and Brazilian coasts at the latitudes of the northeast and southwest poles (Section 2.4, SASDCOAST). The SASDCOAST values in TrACE and UVic decrease by 1.5^oC and 1^oC, respectively, from 9 to 8 ka (Fig 2 - top). After 8 ka, the SASDCOAST values in both simulations increase back to its initial value. The UVic and TrACE long-term behaviors are very similar to SASDREC for the period, having a similar magnitude of 1.5^oC. It must be stressed, however, that after 7.5 ka, the TrACE SASDCOAST decreases again, unlike SASDREC. The CCSM3 simulation is forced with a freshwater flux over the first hundred years of the experiment, leading to a decrease in

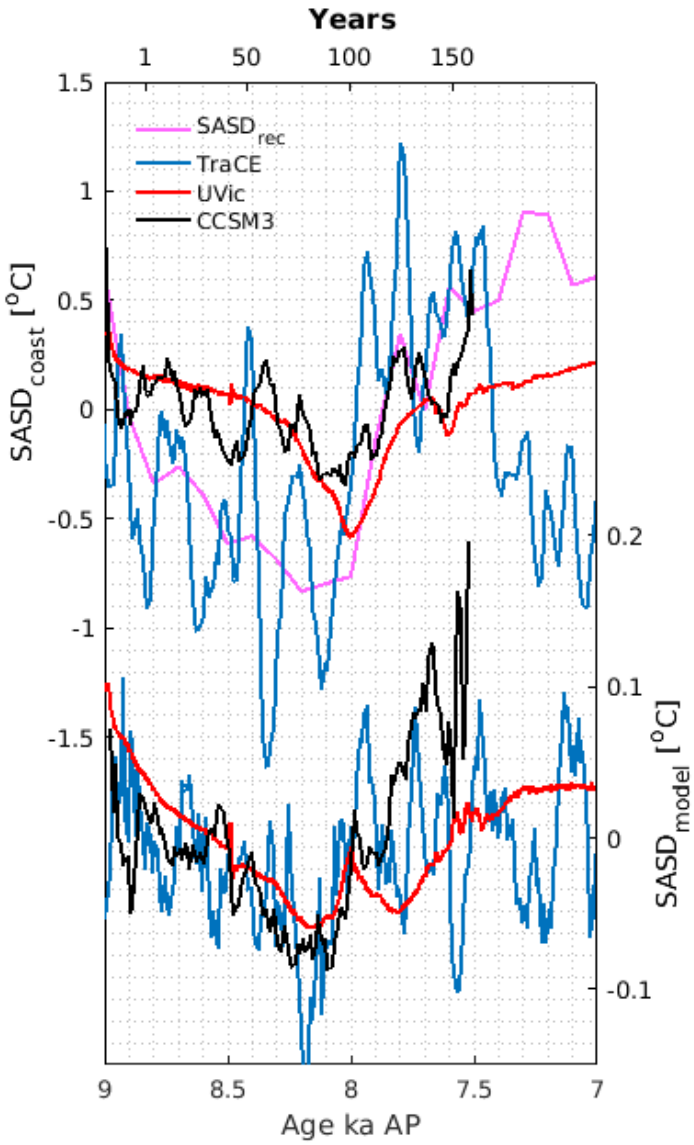

Figure 2: SASDrec, SASDcoast and SASDmodel time series. The UVic and TrACE integration years are shown on the bottom x-axis, while the CCSM3 integration years are shown on the top x-axis. The SASDcoast and SASDmodel values are on the left and right y-axes, respectively.

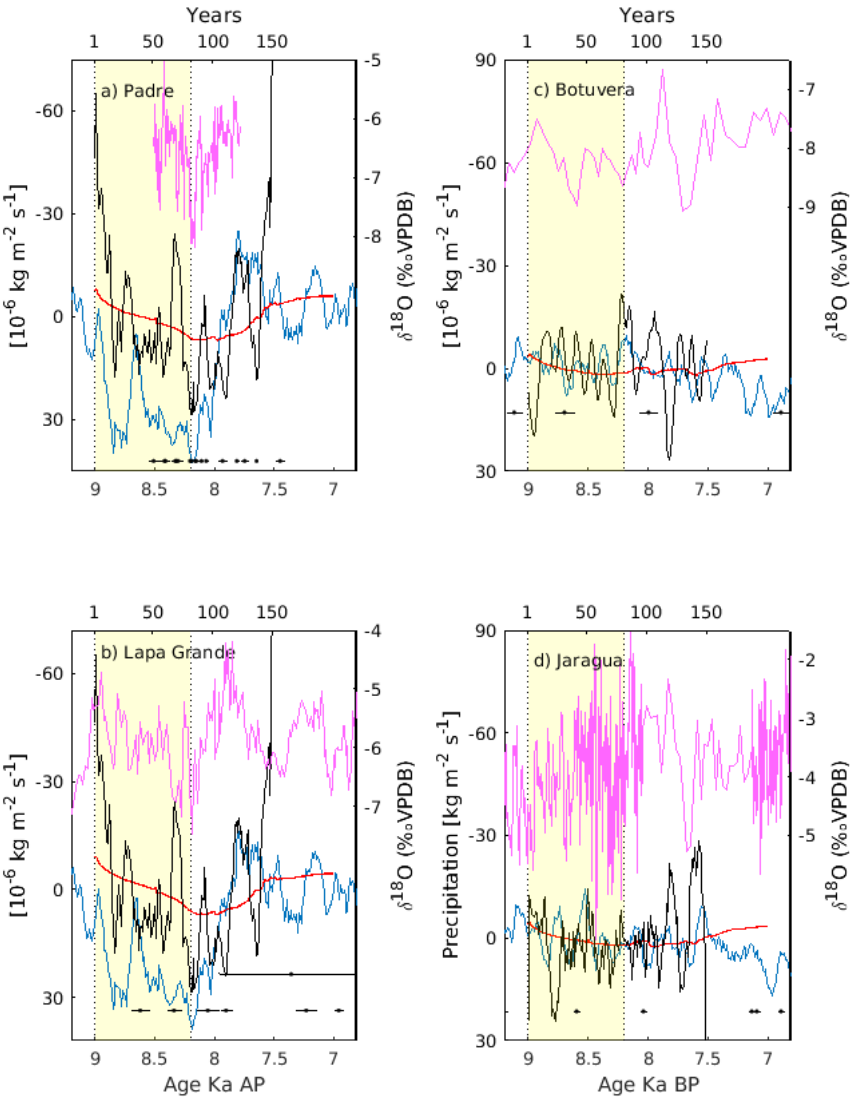

Figure 3: Comparison between the simulated precipitation and $\delta^{18}O_p$ for South American caves. Blue, red and black lines are the TrACE, UVic and CCSM3 precipitation time series at the cave locations, respectively. The purple line is the cave $\delta^{18}O_p$. The UVic and TrACE integration years are shown on the bottom x-axis, while the CCSM3 integration years are shown on the top x-axis. The yellow band marks the period of decreasing SASD. Note that the precipitation vertical axis is flipped, with values decreasing from top to bottom. The right y-axis in all plots are for the $\delta^{18}O_p$ series, while the left y-axis are for the simulated precipitation.

SASDcoast over this period of time. The coastal index then recovers within 50 years after the freshwater forcing ends. Hence, all the models reproduce the magnitude and trends in the SASD changes in the proxy records.

Comparing SASDcoast with SASDmodel, we can see that the coastal index does reproduce the main decreasing trend between 9 and 8 ka as well as the posterior increase in SASDmodel. The smaller range in the variation in SASDmodel (approximately 0.2^oC) is due to SST anomalies being calculated based on the area means, resulting in lower variability. Even though the range of variability in SASDmodel seems small, full SASD events have been identified to have SST anomalies of up to 0.6^oC (Nnamchi et al., 2017), and hence a $0.2\ ^oC$ shift would induce higher frequency and persistence of negative SASD phases. The similarity between signals indicates that the SASDmodel index captures the main variability in the proxy SASD.

We also compared the simulated precipitation at each cave location to the speleothem oxygen isotope ratio. The simulated precipitation increases at both the Padre and Lapa Grande Caves from 9-8 ka in the TrACE and UVic simulations and within 1-100 years in CCSM3 (Fig 3a-b). As the amount of precipitation increases, $\delta^{18}O_p$ decreases, and this signal is present in the SASDmodel index. The TrACE, CCSM3 and UVic precipitation amounts increase by approximately $3x10^{-5}$, $9x10^{-5}$ and $1x10^{-5}$ kg m^{-2} s^{-1}, respectively. The mean model-calculated precipitation at the cave locations ranges from $3.8x10^{-5}$ kg m^{-2} s^{-1} to $4.5x10^{-5}$ kg m^{-2} s^{-1}, so the anomalies represent a considerable precipitation increase. After freshwater forcing ends (8 ka and 100 years), precipitation decreases again while the $\delta^{18}O_p$ increases. The simulated precipitation in the southernmost caves (Jaragua and Botuverá) does not show a clear trend, agreeing with the lack of trend in $\delta^{18}O_p$. When taking into account both the simulated SASD and precipitation signal, all three simulations show a decreasing signal from 9 to 8 ka (increasing precipitation) and a rise afterward.This is the signal we are interested in analyzing and thus we can have more confidence in using the models to study the dynamical processes leading to reversed SASD and strengthened SAMS in the early Holocene.

5. Simulated overturning

Climate reconstructions and simulations have shown that freshwater added to the North Atlantic has the potential to concentrate heat in the South Atlantic and weaken the Southern Hemisphere trade winds by weakening in-

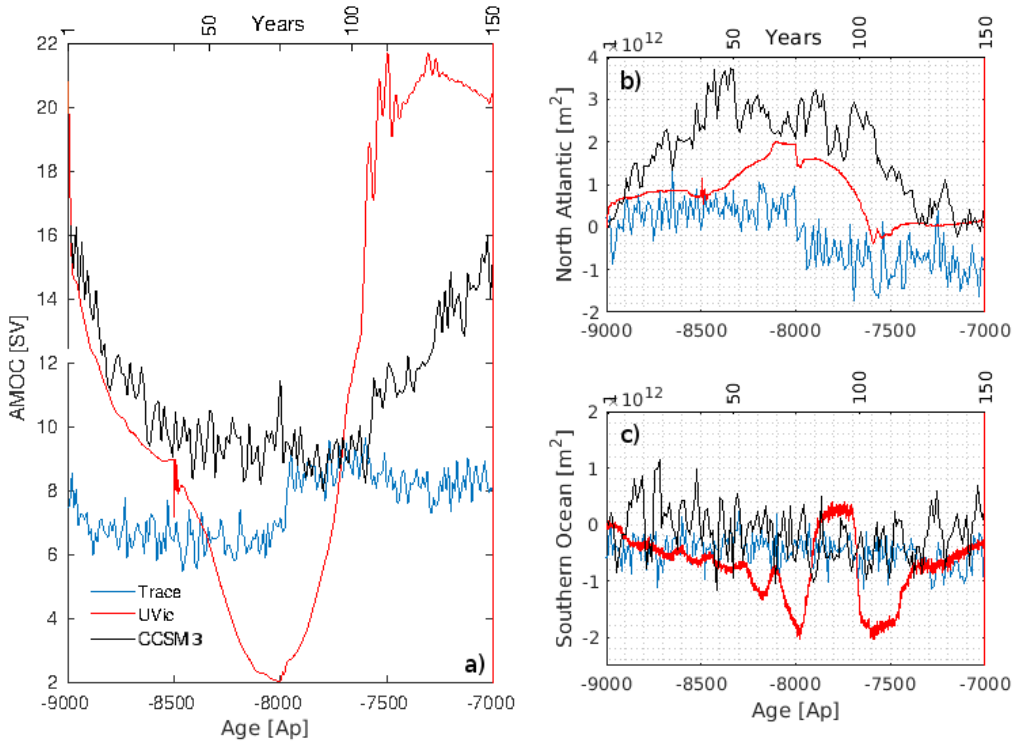

Figure 4: AMOC index [Sv] for all the simulations (a) and sea ice extent anomalies [10^{12}m^2] in the North Atlantic (b) and Southern Ocean (c). The blue and red curves correspond to the TrACE and UVic simulations, respectively, and the time integration is shown on the bottom horizontal axis, while the black curve corresponds to CCSM3, and the integration time is shown on the top horizontal axis.

terhemispheric transport (Chiang and Bitz, 2005; Chiang et al., 2008; Kim et al., 2002; Pedro et al., 2018). Changes in both the heat transport and trade wind shifts impact sea surface temperature patterns in the South Atlantic (Stocker et al., 1992; Wagner, 1996) and hence affect the SASD. Overturning in the TrACE simulation decreases from 8 Sv to approximately 6 Sv between 9 and 8 ka and recovers after 8 ka, reaching 9 Sv (Fig 4a). Note that the freshwater addition timing in TrACE is concurrent with the AMOC weakening between 9 and 8 ka. During the slowdown phase of the AMOC, the circulation weakens by 1.5 Sv, but the main structure of the circulation does not change (Fig C.4-a). The weakening is noticeable in the upper 2000 m. As AMOC weakens, zonal velocities decrease in the location of the northeastern SASD pole (Fig C.4-c). After the freshwater forcing stops (8-7 ka) the AMOC recovers with an intensification of the circulation and a deepening of NADW (Fig C.4-b – 1000-3000m), and zonal velocities are restored to the 9.1 ka values (Fig C.4-d). The CCSM3 non-transient simulation (CCSM3 hereafter) has a duration of 150 years and starts with the Lake Agassiz outburst. The CCSM3 overturning is similar to TrACE: the AMOC in this simulation drops from 16 Sv to 9 Sv within the first 100 years of freshwater forcing. After year 100, when freshwater forcing stops, the AMOC recovers, reaching approximately 15 Sv by the end of the 150 years of simulation. The AMOC in the UVic simulation weakens from approximately 20 Sv to 2 Sv during the freshwater forcing period (9-8 ka). After 8 ka, the AMOC restarts and stabilizes to approximately 20 Sv again by 7.5 ka. TrACE is fully transient and accounts for the freshwater forcing discharges associated with Heinrich event 1 and the Younger Dryas prior to the Holocene (He, 2011). The forcing prior to the Holocene possibly diminishes initial overturning in TrACE, making the initial AMOC overturning lower than that of CCSM3. Considering that the total mass added to the ocean in TrACE (7.5 m in SLR equivalent) is larger than in CCSM3 (1.5 m in SLR equivalent) and that both TrACE and CCSM3 use the Community Climate System Model, version 3, we can infer that the stronger decrease in AMOC in the CCSM3 simulation is possibly due to higher freshwater flux over a shorter time. In turn, the stronger AMOC slowdown in the UVic simulation compared to TrACE is possibly due to the stronger sensitivity of the UVic model to hosing. All models show a weakening of the overturning that reaches a minimum by the end of the respective freshwater addition, and after hosing ends, AMOC recovery takes place.

The zonal heat distribution in the Atlantic is directly affected by zonal

Ekman transport, which in turn responds to wind shifts. Moreover, sea ice expansion can have an impact on trade winds and deep water formation (Chiang and Bitz, 2005). Fig 4b shows the total sea ice area in the Northern Hemisphere for all simulations. In all three simulations, the North Atlantic sea ice area (SIA) increases during the freshwater forcing period, i.e., approximately 9-8 ka for TrACE and UVic and 1-100 years for CCSM3. The TrACE and UVic SIAs increase by approximately $1x10^{12}m^2$ and $2x10^{12}m^2$, respectively, while the CCSM3 area increases by $3x10^{12}m^2$. At 8 ka, with the AMOC restart, heat transport is restored in the North Atlantic, and the SIA starts to decrease again in the UVic and TrACE experiments. After 7.5 ka, the North Atlantic SIA plateaus into a new equilibrium value as the AMOC reaches equilibrium as well. In CCSM3, the SIA reaches its maximum after approximately 50 years of simulation, stays relatively high until year 80 and decreases afterwards. Despite the distinct variability in each simulation, the time series of the AMOC index and the North Atlantic SIA have a coherent pattern: As freshwater is added to the North Atlantic (9-8 ka or 1-100 years), the AMOC slows down and sea ice expands in the North Atlantic, while the opposite occurs when freshwater forcing stops.

The Southern Ocean SIA response to AMOC changes varies between models (Fig 4c). While both the TrACE and CCSM3 exhibit no significant Southern Ocean sea ice response to the freshwater forcing in the early Holocene, the UVic model shows high SIA variability. From 9 to 8 ka, the UVic SIA decreases by $2x10^{12}m^2$ in the Southern Ocean. This decrease is triggered by an increase in open-ocean deep convection and Antarctic Bottom Water formation, melting sea ice due to warmer water advected southward and brought up from deeper layers in the Southern Ocean (supplementary materials). This behavior is consistent with the bipolar seesaw hypothesis (Broecker, 1998). From 8 ka-7.5 ka onwards, strong positive anomalies in the SIA occur, as Antarctic Bottom Water formation reaches its maximum (see Fig B.2-3 in the supplementary materials). Finally, after 7.5 ka, the AMOC stabilizes, and as the Southern Ocean starts to cool down again, the SIA increases, which is an ocean dynamic response to North Atlantic overturning slowdown. Southern Ocean deep convection events in the open ocean in the UVic model have been previously described by Meissner et al. (2007). Similar processes have been suggested by Azaneu et al. (2014) and Aguiar et al. (2017) for reanalysis products. This 8-7.5 ka signal does affect the SASD (Section 6), and we will analyze the SASD anomalies in this period. However, those anomalies are outside the period that we aim to analyze for

the freshwater forcing response (9-8 ka) and are therefore not the focus of this study.

6. Early-Holocene SASD

EOF analysis was performed to determine the main variability pattern in all the simulated SSTs and their link with the SASD between 9-7 ka (Fig 5). The first global components of the SST EOF analysis have correlations of 0.72, 0.6 and 0.87 with the AMOC index for TrACE, the UVic model and CCSM3, respectively. The spatial pattern of the first EOF shows positive temperature anomalies in the North Atlantic and negative ones in the South Atlantic (Fig 5a-c). When the AMOC weakens (9-8.2 ka and 1-100 years), the 1^{st} component from all the models show warming in the South Atlantic and cooling in the North Atlantic.

After freshwater forcing stops, the time series of the first EOF from both TrACE and CCSM3 increase, restoring the North and South Atlantic SSTs. In the UVic simulation, the 1^{st} component also increases after the cessation of freshwater forcing but has an oscillatory behavior between 8 and 7.6 ka. This oscillation matches the variability in the Southern Ocean deep convection and sea ice area discussed above (Fig 4c).

In all three models, as the AMOC weakens and the South Atlantic warms, the area-based SASD index moves towards negative values (Fig 5d, 9-8.2ka). The decrease in the SST gradient equals 0.3^oC, 0.4^oC, and 0.2^oC in the TrACE, CCSM3 and UVic simulations, respectively. As the AMOC restarts, the SASD$_{\text{MODEL}}$ indices for the TrACE, CCSM3 and UVic simulations increase towards positive values again. The SASD$_{\text{MODEL}}$ index in the UVic simulation again shows an oscillation due to changes in AABW formation. This oscillation is a quarter of the magnitude (0.05^oC) of the main SASD decay (0.2^oC); hence, we consider it a minor departure from the main SASD$_{\text{MODEL}}$ increase.

A negative SASD$_{\text{MODEL}}$ value is therefore a consistent response to freshwater anomalies between 9 and 8 ka. The agreement between the simulations and reconstructions (SASD$_{\text{REC}}$, Fig 2) points to the persistence of a weaker dipole in the transition from the early to middle Holocene. After the freshwater addition period ends, the SASD values increase again. Since the simulations forced only with meltwater (CCSM3 and UVic model) show a decrease in the SASD, the freshwater addition to the North Atlantic, and

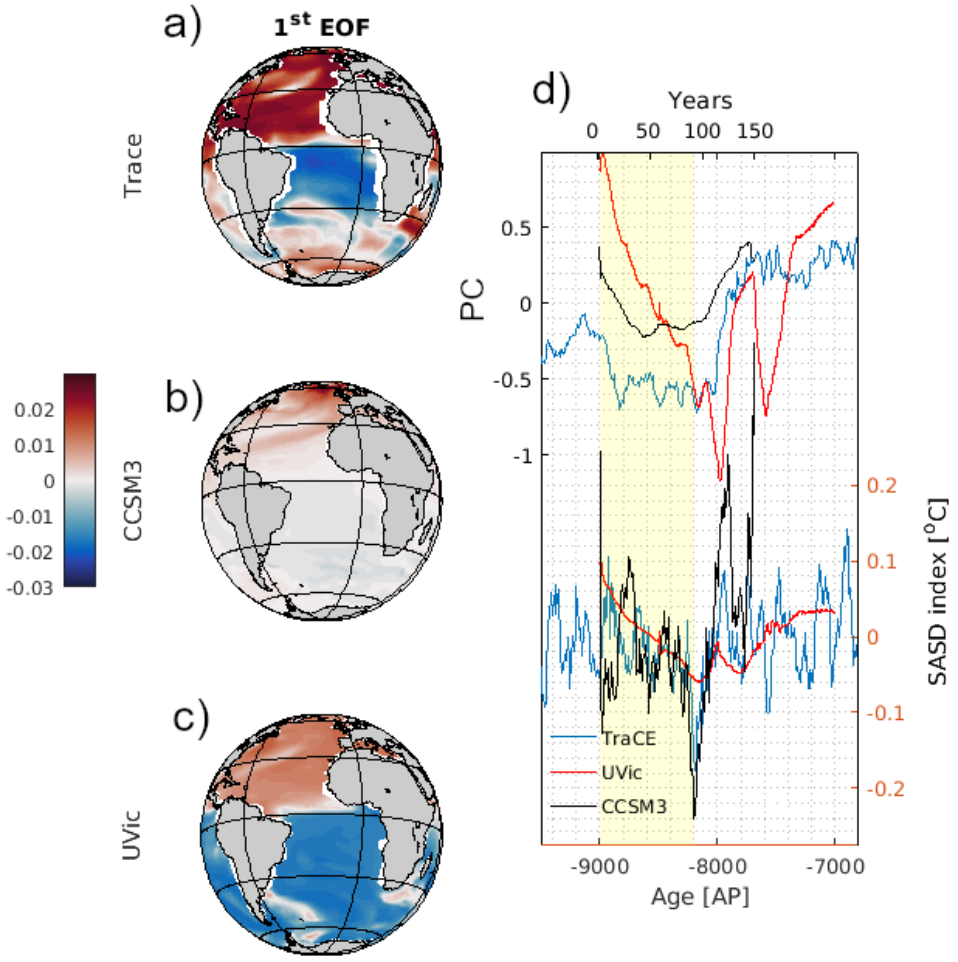

Figure 5: EOF analysis of the sea surface temperature and SASDMODEL. Maps a, b and c represent the 1^{st} EOF components for the globe in TrACE, CCSM3 and UVic simulations, respectively. Graph d is the time series of the normalized values for the 1^{st} component (top) and nonnormalized area-based index (SASDMODEL - bottom). The yellow box highlights the period of slowing AMOC in all simulations.

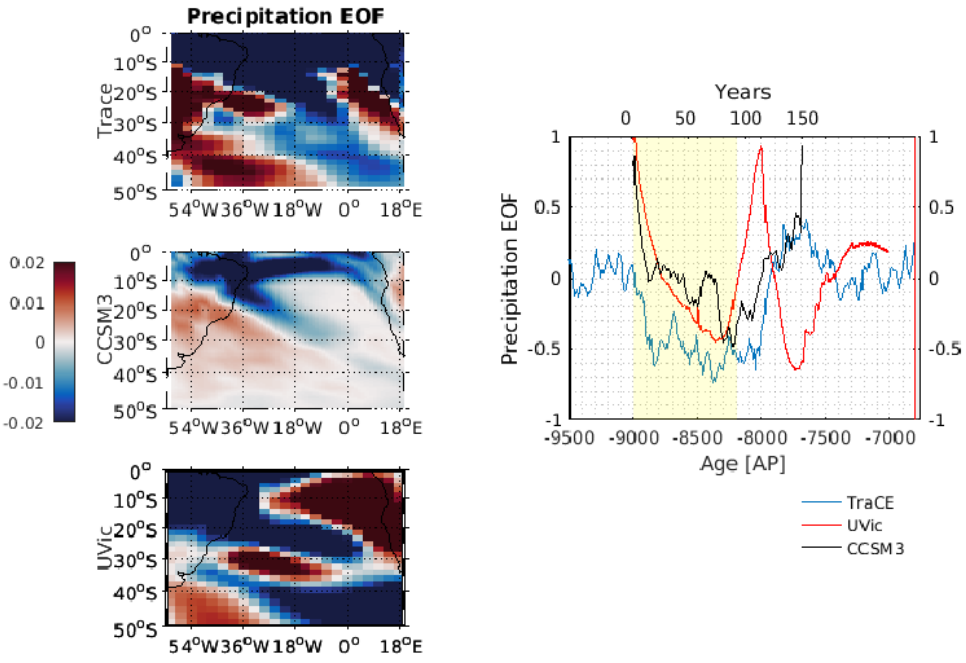

Figure 6: SAMS signal of the precipitation in the EOF analysis. The maps represent the precipitation EOF component for the South Atlantic and South America in the simulations. The graph is the time series of the values for the principal components of the EOFs. The yellow box highlights the period of weaker AMOC in all simulations. The precipitation modes in the TrACE, CCSM3 and UVic simulations explain 51%, 50% and 30% of the precipitation variability, respectively.

not the other transient forcings included in the TrACE simulation, is likely the forcing responsible for triggering the SASD shift in the early Holocene.

Negative SASD events enhance the SAMS by increasing the amount of precipitation over the ITCZ and SACZ (Liebmann et al., 2004), with increased precipitation over northeastern South America and decreased precipitation in southern South America (Cavalcanti, 2012). The SST-precipitation coupling mechanism proposed by Wainer et al. (2014) states that warming over the northeast SASD pole during a negative SASD phase enhances ocean evaporation, resulting in higher atmospheric moisture over the respective latitudinal band. An EOF analysis of the precipitation was performed here to evaluate the evolution of the precipitation pattern. The components that cap-

tured the SAMS spatial signal were the 1^{st} EOF for the TrACE and CCSM3 simulations and the 2^{nd} EOF for the UVic simulation, showing anomalies in the Intertropical and the South Atlantic Convergence Zones (Fig 6). A positive EOF signal for the three simulations represents negative precipitation anomalies over the SACZ and ITCZ, and a shift towards positive anomalies southwards. The three simulations are characterized by a shift of the EOF time series towards negative values when the AMOC is weakened; i.e., the precipitation increases in northeastern South America (Fig 6d). When the AMOC recovers, the TrACE and CCSM3 principal components increase back to their initial values. During recovery, the UVic simulation shows the oscillation already described in the SST and sea ice signals, which points to an SST-precipitation coupling in the mechanism. The EOFs describing the SAMS variability explain 51%, 50% and 30% of precipitation variability in TrACE, CCSM3 and UVic experiments, respectively. Finally, the synchronous weakening of the bipolar seesaw and precipitation EOFs and SASD index during overturning slowdown suggests that there is a link between the AMOC strength, SASD negative and SAMS positive anomalies. A Pearson's correlation between the SASDMODEL and the precipitation principal component time series results in correlation coefficients of 0.62, 0.70, and 0.46 for TrACE, CCSM3, and the UVic model respectively ($p<0.05$), showing a moderate relationship between the patterns. Moreover, the determination coefficients from a linear regression between the SASDMODELand precipitation are 0.38, 0.5, and 0.21 in TrACE, CCSM3, and UVic simulations, respectively. Those determination coefficients suggest that SASD explained up to 50% of the precipitation signal of SAMS during the 8.2 ka event. Hence the SASD possibly exerts a second-order forcing on the precipitation in the early-Holocene.

7. Mechanisms of SASD variability

The zonal heat distribution in the South Atlantic is directly affected by the strength of the trade winds. A weaker wind meridional component decreases the westward Ekman transport, displaces the surface heat from the Brazilian coast towards the African coast, and reduces the depth of the thermocline. Hence, changes in the wind during the early Holocene could have altered the surface mixed layer heat content in the SASD poles, shifting the system. To analyze the role of the winds in shifting the SASD towards negative values, we used the 1.5 layer solution (Eq. 1) to compute the depth

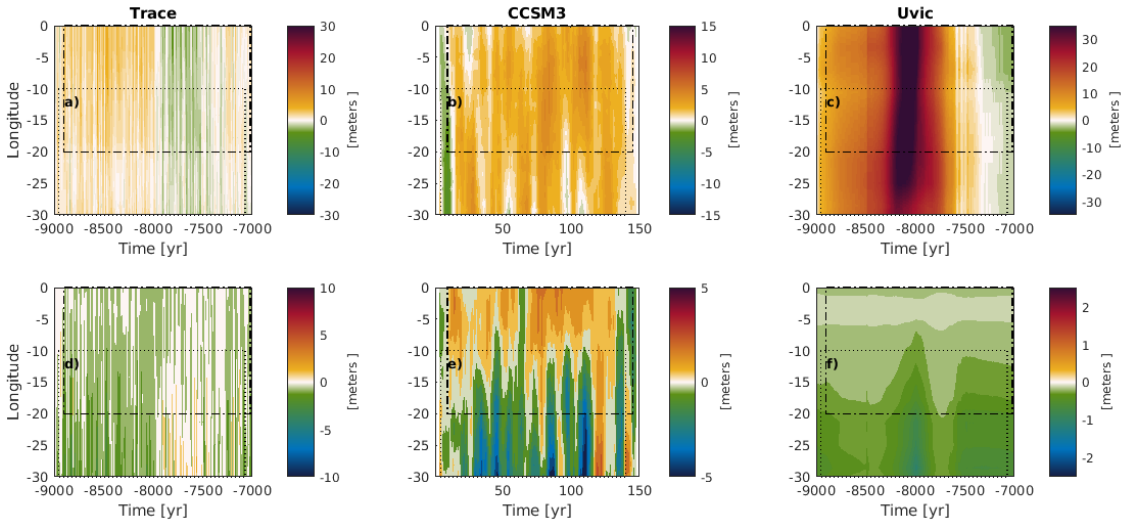

Figure 7: Mean depth anomaly (m) of the 17^{o}C isotherm from 15^{o}S to 40^{o}S. a, b and c are the simulated anomalies, and d, e and f are the wind predicted anomalies ($h(x, y)$) for the TrACE, CCSM3 and UVic experiments, respectively. Dashed and dotted boxes show the values within the longitude ranges of the northeast and southwest SASD poles.

of the 17^{o}C isotherm. In TrACE, the wind causes a shallowing of the 17^{o}C isotherm within the South Atlantic during 9-8 ka, i.e., during freshwater forcing, with an upward displacement of up to 3 m (Fig 7d), which is larger in the western Atlantic. In the CCSM3 experiment, the wind-induced shallowing of the western isotherms of 10 m and a 5 m deepening of the eastern isotherm (Fig 7e) from year 1 to 100. The same pattern is observed in the UVic simulation from 9-8 ka, with a maximum shallowing of a meter (Fig 7f), especially after 8.5 ka. The wind anomalies in the UVic simulation derive from a geostrophic adjustment to air temperature anomalies, and not from a fully resolved atmospheric dynamics. This method of adjustment might explain the low magnitudes of isothermal deepening in the UVic simulation. Nevertheless, the upward movement of the thermocline indicates cooling of surface waters by their mixing with deep colder waters. Accordingly, as western isotherms move upwards, it is expected that colder deep waters will reach the surface, cooling the SST distribution of the southwestern SASD pole, and pushing the dipole towards negative values. The simulated decay of the SASD from 9-8 ka in Fig 5d hints this is the process responsible for shifting the SASD. Hence, when freshwater is added to the North Atlantic, winds tilt

the isotherms, which results in the development of a negative SASD phase.

After the freshwater forcing period, TrACE winds push the isotherms down again in the western South Atlantic, pushing the dipole index towards the positive phase (Fig 7d, 8-7ka). In CCSM3, the wind-driven isothermal downlift occurs after year 110 (Fig 7b). The western isotherms deepen by up to 5 m after year 110, and the eastern Atlantic isotherms move upwards from 130-150 years in CCSM3. This motion drives the dipole towards positive values by cooling the notheastern SASD pole and warming the southwestern pole. In the UVic model, wind-driven isothermal downlift occurs through an oscillation (Fig 7f). First, the western Atlantic isothermal depth anomaly becomes less negative, i.e., western isotherms move downwards from 8.2-7.8 ka. This motion pushes the dipole towards positive values (Fig 5d) by warming the southwestern SASD pole. From 8-7.6 ka, the negative anomalies in the western pole become more negative, the 17^{o}C isotherm moves up again and the dipole becomes negative (Fig 5d). Finally, after 7.6 ka, the isotherms slowly deepen again, driving the SASD to be positive again.

A comparison of the wind-driven isothermal shift from the 1.5 layer model with the 17^{o}C depth shift obtained from the simulations illustrates how the wind effect changes the thermocline. To simplify the text here, we will call the depth of the 17^{o}C isotherm obtained directly in the water column of each simulation Z17. This parameter differs from the wind-driven one calculated from the 1.5 layer model. The changes in the depth of Z17 in TrACE, UVic and CCSM3 show a deepening when freshwater forcing is added to the North Atlantic (9-8 ka, Fig 7a; c, years 1-100, Fig 7b). Deepening in all the models seems to be concentrated within the South Atlantic eastern boundary. At 20^{o}W in TrACE, the Z17 deepens by up to 15 m, while in the CCSM3 and UVic, it deepens by 15 m and 30 m, respectively. The South Atlantic temperature increase is expected in a slowing overturning scenario due to slow northward heat transport. As the bipolar seesaw shifts towards a state of slower northward heat transport, heat concentrates in the South Atlantic (Pedro et al., 2018). Thus, the isothermal deepening results are consistent with the bipolar seesaw variability. However, as the AMOC slows down, the winds over the South Atlantic in the simulations cause a shallowing of the isotherms, mostly in the western South Atlantic (Fig 7d-f). This shallowing and the heat addition to the South Atlantic creates the final pattern of deeper eastern isotherms and warms up the surface of the northeast pole. A warmer northeast South Atlantic then reduces the SASD index.

After the meltwater forcing period ends (after 8 ka and year 100), the

TrACE Z17 moves up again, with stronger shallowing in the eastern Atlantic (8-7.5 ka), which induces a positive shift in the SASD. This vertical displacement in Z17 is not evident in the CCSM3 simulation, but it can be seen in the UVic results. The absence of uplift in Z17 in the CCSM3 simulation does not necessarily discredit the SASD return to positive values. Especially because other oceanic signals, such as water mass entrance or wave propagation, interfere with the measured isothermal displacement. The dynamic analysis shows that South Atlantic winds push the western isotherms upwards, while ocean dynamics heat up the surface of the South Atlantic. The combination of these two factors act by concentrating heat in the eastern South Atlantic and pushing the SASD towards negative values. It is important to highlight that there is a difference in the magnitude of the vertical migration of the Z17 and the wind-driven isothermal deepening. That is because the 1.5 layer model does not simulate the propagation of eastern boundary isothermal deepening into the interior ocean by Rossby waves. Hence, it is likely that other processes triggered by freshwater addition in the North Atlantic amplify the isothermal deepening in eastern South Atlantic.

Finally, none of the previously analyzed signals seem to have a large response by 8.5 ka or year 1; i.e., they do not seem to be directly forced by the lake outburst, showing that background slow freshwater addition is more important for modulating the SASD than abrupt freshwater release.

8. Wind anomalies between AMOC states

The 1.5 layer analysis suggests that wind anomalies during different AMOC states shift the zonal heat distribution, hence shifting the SASD state. Here, we will investigate the SST and wind patterns under the AMOC slowdown and recovery states. Meridional (zonal) winds control zonal (meridional) surface transport; hence, we will use the wind components to understand the transport of surface waters. It is important to highlight however that changes in the meridional winds affect mostly the eastern boundary isotherms, while its propagation to internal ocean happens due to Rossby waves propagation.

Trade winds in the TrACE experiment weakened during the AMOC slowdown phase, while the anomalies in the westerly winds seemed to vary with longitude (Fig 8, 9-8 ka). During the AMOC slowdown phase, the SSTs increased by 0.2^{o}C in the northeast South Atlantic, while the southwest Atlantic cooled. Weakening of the meridional winds can decrease westward Ekman transport and hence concentrate heat in the eastern South Atlantic.

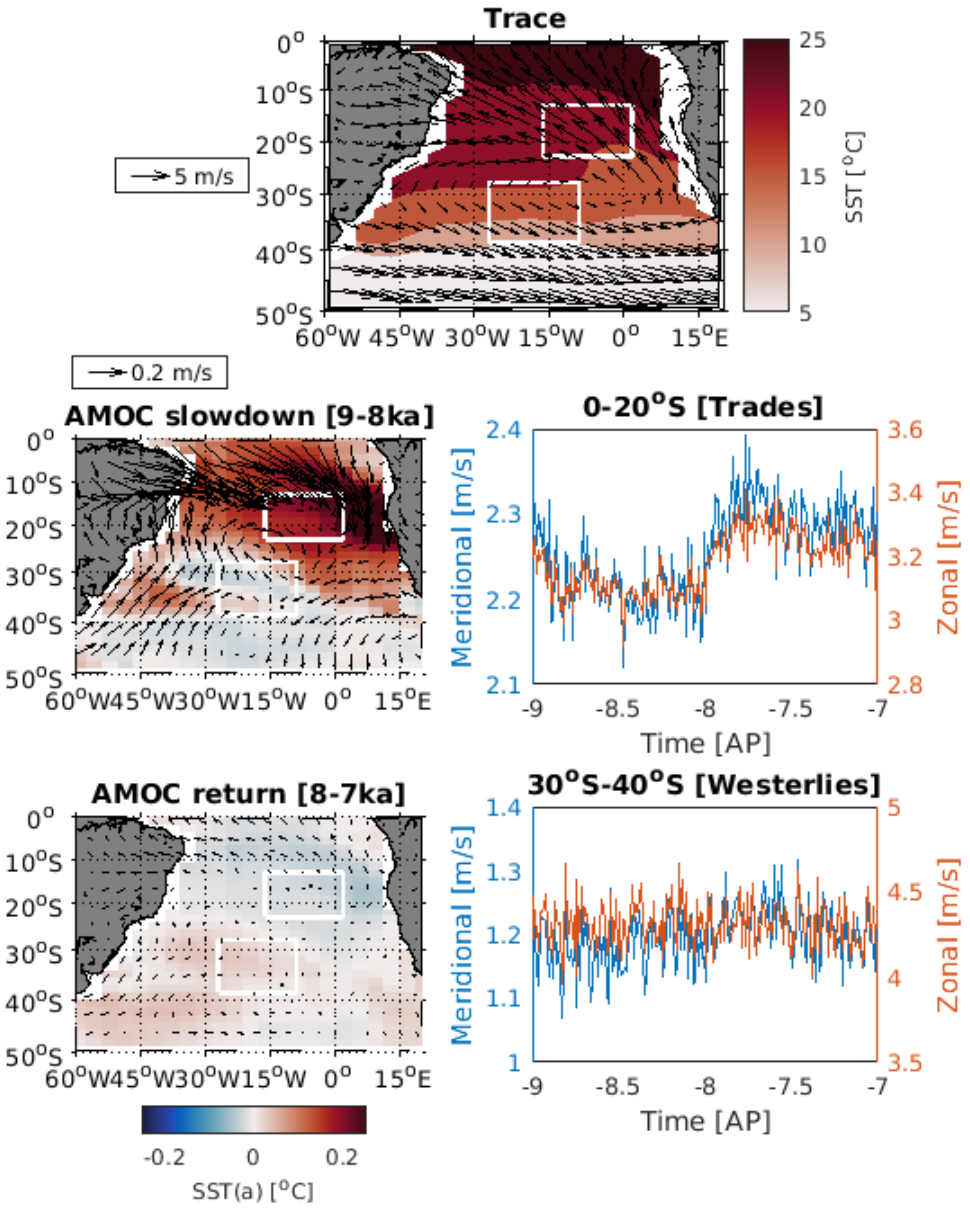

Figure 8: Wind anomalies during the AMOC slowdown (9-8 ka) and AMOC recovery phases (8-7 ka) in TrACE. The map colors are the SST anomalies, and the time series show that the mean surface wind components within the Atlantic. Anomalies are calculated using the 9-7 ka mean. White boxes show the location of the northeast and southwest SASD poles.

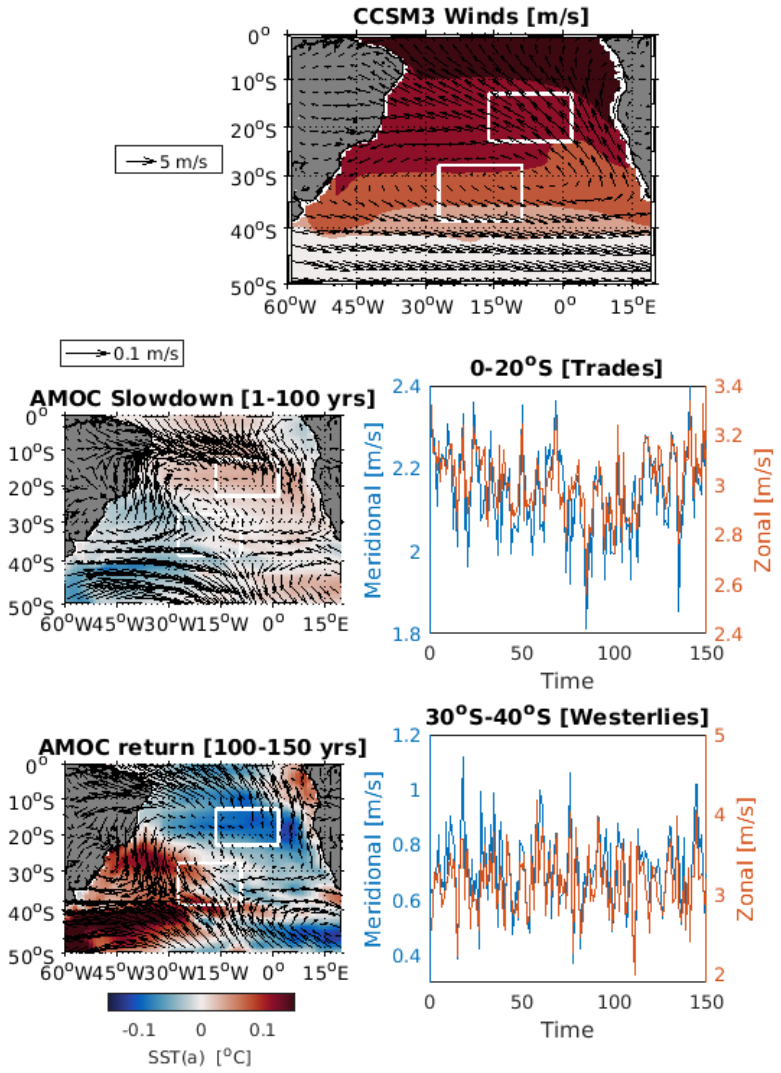

Figure 9: Wind anomalies during the AMOC slowdown (1-100 ka) and resumption phases (100-150 ka) in CCSM3. The map colors are the SST anomalies, and the time series represent the mean components within the Atlantic. The anomalies are calculated using the 1-150 year mean.

Additionally, weakening of the trade wind's zonal component can concentrate warm surface waters in the northern South Atlantic. In fact, the time series of the meridional component of the trade winds between 0-20ºS show a 0.1 m/s weakening, while the zonal component weakens by 0.2 m/s from 9-8 ka. After 8 ka, the trade wind speeds increase. The westerlies, however, do not seem to have any measurable signal through the whole simulation, hence not necessarily affecting the SASD signal. SST anomalies agree with a negative SASD phase from 9 to 8 ka. In the AMOC recovery phase, the wind anomalies decrease, and the SST anomalies between poles revert, agreeing with a positive SASD phase.

In CCSM3, while the AMOC weakens in the first 100 years of simulation, the meridional (zonal) component of the trade winds weakens by 0.3 m/s (0.6 m/s), and positive SST anomalies appear in the northeast South Atlantic (Fig 9). SST anomalies in this phase also point to a negative SASD. The westerlies do not show any apparent trend throughout the simulation. In the AMOC return phase, the SST anomalies revert, with cooling in the northeast pole and warming in the southwest pole. At this point, wind anomalies show that the trade winds strengthen again.

The UVic simulation wind anomaly maps and time series show that the meridional component of the trade winds also weakens by $0.04m/s$, and the zonal component weakens by $0.02m/s$ during the AMOC slowdown phase (Fig 10, 9-8.2 ka). In contrast to previous simulations, the westerlies seem to accelerate in the UVic simulation by $0.03m/s$ from 9-8 ka. The SST anomalies show a warming phenomenon concentrated in the northeast pole, also pointing to a negative SASD. After 8 ka, while the AMOC accelerates, the mean meridional component of the trade winds increases again, and the northeast pole cools down. The signal of the westerlies after 8 ka seems to have a response identical to the bipolar seesaw EOF (Fig 5c).

9. Summary and conclusions

The SAMS is one of the most important modes of precipitation variability in South America (Vera et al., 2006). Specifically, an early-Holocene SAMS intensification has been proposed (Wainer et al., 2014), most likely connected to meltwater fluxes into the North Atlantic. This points to the initial question raised in the introduction: (1) Does the spatial pattern of reconstructed South American precipitation points to a strengthening of the SAMS around 9-8 ka? We indeed found this phenomenon. The agreement

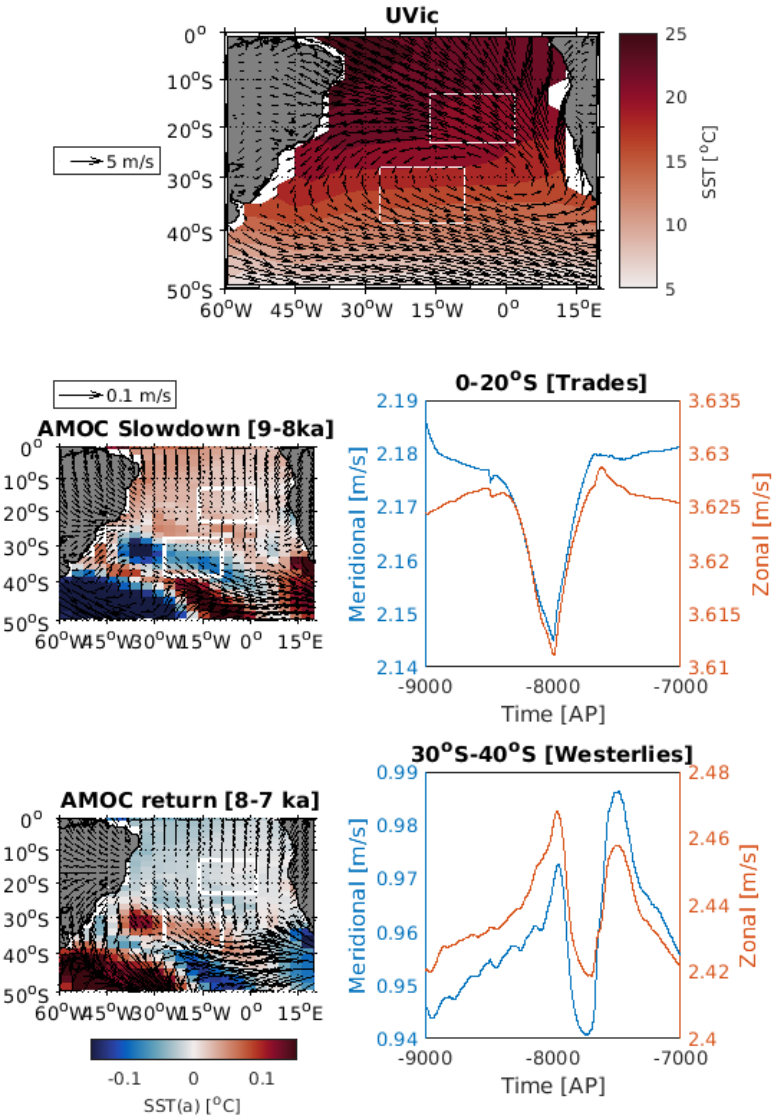

Figure 10: Wind anomalies during the AMOC slowdown (9-8 ka) and AMOC resumption phases (8-7 ka) in the UVic model. The map colors are the SST anomalies, and the time series represent the mean wind components within the Atlantic. The anomalies are calculated using the 9-7 ka mean.

and weakening of the $\delta^{18}O_p$ negative rends towards southern South America (Section 3) corroborates that hypothesis. Cheng et al. (2009) present evidence of a precipitation increase in South America connected to the 8.2 ka event. Although our study agrees with their findings, we advise caution since there are still too few speleothem records in South America that can be analyzed to infer the SAMS signal for the study period.

The study of other analogous periods with weakening overturning can provide evidence of the validity of the early-Holocene changes proposed here. The examination of widespread continental precipitation records by Stríkis et al. (2011) shows evidence of increased SAMS during 8.2 ka. Additionally, an intense strengthening of the SAMS has been proposed for Heinrich Stadials 1a and 1c (Stríkis et al., 2015). Heinrich events are associated with ice rafting, weakened overturning and the southward migration of the Intertropical Convergence Zone (Broecker et al., 1992), all processes used to explain our proposed SAMS strengthening mechanism. We conclude that the documented SAMS intensification regimes during other low-overturning states corroborate our hypothesis of a stronger SAMS due to meltwater addition to the North Atlantic during the 8.2 ka event.

Modeling experiments with AMOC weakening in the North Atlantic have shown an increase in South American precipitation and a change in the South Atlantic heat distribution (Frierson et al., 2013; Mulitza et al., 2017). Wainer et al. (2014) proposed that South Atlantic surface heat variability plays a key role in early-Holocene SAMS intensification, specifically due to the SASD teleconnection. However, is the SASD-SAMS shift caused by freshwater addition to the North Atlantic (2)? Our results indicate that it is. Simulations in which the single transient forcing is the meltwater addition to the North Atlantic reproduce SASD shifts similar in magnitude to the reconstructions. While we used two different models and three simulations in this study, this mechanism will need to be tested with other models. Furthermore, other transient forcings could also contribute to the SASD signal. The rising atmospheric temperatures in the early Holocene might play a role by causing widespread warming of the South Atlantic and increased South Atlantic evaporation. However, freshwater-triggered trade wind weakening is most likely the direct contributor to SASD-SAMS changes. Further sensitivity studies with a variety of single-forcing experiments are required to quantify the effect of each climate component on the strengthening of the SAMS. Additionally, Lopez et al. (2016) suggested that decadal variations in AMOC and the Atlantic meridional heat transport can be potential predictors of the strength

of the global monsoons within a 20 years adjustment lag. Indeed, in our analysis, we find evidence that a weakening of AMOC and the consequent anomalies in South Atlantic SSTs during the early-Holocene can enhance the South American Monsoonal system.

Finally, (3) what are the mechanisms causing the negative SASD and strengthened SAMS during the early Holocene? Here, the proposed mechanism is based on ocean and atmospheric changes during the low-overturning phase: As the AMOC slows down, heat concentrates in the South Atlantic and the trade winds in Southern Hemisphere weaken. Weakened trade winds push the isotherms upwards, with higher vertical movement on the western South Atlantic. This differential isothermal uplift contributes to more heat being stored in the eastern South Atlantic, warming up the northeast SASD pole. Warmer waters in the northeast South Atlantic enhance evaporation. Excess moisture is then transported to northeast South America, where the SAMS regime is then intensified. Freshwater forcing has been identified as one of the trigger mechanisms for SAMS intensification (Stríkis et al., 2011). Caution has to be taken regarding the interpretation of our results for three reasons. First, the signal found here for the SASD-driven SAMS shift is likely embedded within a larger picture of South Atlantic warming. Widespread warming is the first South Atlantic signal in the SST when the AMOC slows down (Pedro et al., 2018). This warming increases South Atlantic evaporation, which likely leads to enhanced continental precipitation. The mechanism proposed here is a second-order SST signal regarding heat redistribution from the southwest to the northeast South Atlantic. In our simulations, this pattern explains up to 31% of the SST variance during the AMOC slowdown and up to 50% of the precipitation increase in the early Holocene. Second, SAMS intensification in low-overturning states has also been associated with the El Niño–Southern Oscillation variability by causing anomalies in the Walker cell circulation and triggering convective rain in northeastern South America (Ropelewski and Halpert, 1989). However, the influence of each of the processes is still under debate (Aceituno, 1988; Zhou and Lau, 2001; Kayano et al., 2013), and we consider the evaluation of the El Niño signal in Holocene precipitation out of the scope of the present study. Another feature of South American precipitation not analyzed here is the modulation of the zonal precipitation regime over the Amazon Basin. This modulation is most likely affected by changes in the SASD since negative SASD intensifies monsoons mostly in the eastern Brazil basin (Wainer et al., 2014). However, we consider this result to be an issue to be addressed in

future studies. Third, present-day SASD events are connected to southward migration of the subtropical high and differential heat fluxes between the SASD poles (Morioka et al., 2011). Latent heat fluxes are mostly considered the main driver, although heat concentration due to zonal Ekman transport also contributes to differential pole SST anomalies (Sterl and Hazeleger, 2003). Our analysis shows that for the early Holocene, weakening of the trade winds changes the ocean vertical temperature structure, which together with extra South Atlantic heat due to the AMOC slowdown, changes the SASD index to negative values. The proposed mechanism explains how extra heating in the surface South Atlantic contributes to the SASD establishment and phase. One mechanism does not necessarily exclude the other; in fact, the weakening of the trade winds can be a consequence of subtropical high weakening. Future studies should evaluate the role of each one of the mechanisms in the establishment of negative SASD values.

Although high-resolution proxies that quantitatively measure precipitation are scarce in South America, several nonquantitative evidence of an increased SAMS exists. Rodrigues-Filho et al. (2002) found deposition of slope-wash sequences in Lake Silvana from 9.4 to 8 ka, suggesting rising lake levels and an extreme increase in rainfall. An analysis of vegetation changes in southeastern Brazil found increasing pollen counts from high-humidity species concurrent with the increase in the level of Lake Silvana during 9.5 - 8.6 ka AP (P et al., 2012; Rodrigues et al., 2016). Lago do Pires pollen stratigraphy in Northeast Brazil records an increase in gallery forests and suggests an increase in precipitation from 8.8 - 7.5 BP (Behling, 1995). Other lake and cave reconstructions also point to increased precipitation during this early Holocene time span (Behling, 2003; Cheng et al., 2009; Horák-Terra et al., 2015).

Further modeling experiments to validate the proposed mechanism need to be performed, especially to test its validity during other meltwater events, such as the Younger Dryas, Heinrich events and Dansgaard-Oeschger events, and to evaluate the effect of solar and greenhouse gas forcing on the SAMS. Future studies with widespread speleothem reconstructions along South America and coastal SST reconstructions can also be used to test the validity of the SASD-SAMS signal in the early Holocene. Finally, the suggested ongoing AMOC weakening is likely a consequence of current global climate change. Changes in the SASD dipole and SAMS are already depicted in other studies (Liebmann et al., 2004; Hsu et al., 2012). Hence, future studies should analyze the coevolution of SASD and SAMS in future AMOC change scenarios.

Capítulo VIII: Síntese da Discussão e Conclusões

VIII.1 Síntese da Discussão

Projeções da intensidade de revolvimento da AMOC demonstram que esta irá possivelmente desacelerar durante o presente milênio devido ao aquecimento do Atlântico Norte e ao potencial derretimento do GIS, ambos gerados pelas emissões

antropogênicas de gases estufa [Rahmstorf et al., 2015]. Desacelerações da AMOC são associadas a um menor transporte de calor para regiões polares, e ao estabelecimento de eventos frios no hemisfério norte. Apesar de modelos do sistema terrestre serem capazes de projetar as consequências climáticas de tal desaceleração, estudos paleoceanográficos podem fornecer perspectivas adicionais, ao analisar eventos frios do passado, gerados por fluxos de água doce e calor no Atlântico Norte. Neste sentido, ainda que o planeta tenha sofrido vários eventos de resfriamento gerados pela desaceleração da AMOC ao longo da transição do LGM para o Holoceno (e.g., *YD*), um evento se destaca por ocorrer no presente interglacial e, portanto, possuir alta similaridade com as condições climáticas atuais: o evento de 8,2 ka AP. Estas similaridades levantaram a hipótese do 8,2 ka servir de análogo climático para a futura desaceleração da AMOC devido ao potencial derretimento do GIS [Schmidt & Legrande, 2005]. No entanto, incertezas relativas à forçante de água doce geradora do 8,2 ka AP e à sua expressão global dificultam comparações mais especificas com os cenários futuros de desaceleração da AMOC. A motivação desta tese é diminuir estas incertezas ao tentar reconstruir a magnitude da descarga de água doce geradora do 8,2 ka AP [Aguiar et al., 2021] e a expressão deste evento na América do Sul e no Atlântico Sul [Aguiar et al., 2020].

No primeiro artigo oriundo desta tese (capítulo VI), uma análise *multiproxy* foi feita juntamente com simulações do sistema terrestre com o objetivo de reconstruir a magnitude da descarga de água doce no mar de Labrador, responsável por gerar o evento de 8,2 ka AP. Estudos anteriores tentaram reconstruir tais forçantes comparando SSTs simuladas e obtidas por *paleoproxies* [Wiersma et al., 2006;Wagner et al., 2013; Morrill et al., 2013, 2014] e assumindo que a simulação que melhor representa os campos de SST dos *paleoproxies* é a que possui a forçante mais realística. No entanto, a

premissa de que a melhor forçante é aquela que produz um campo de SST mais similar ao reconstruído não necessariamente é realista, já que reconstruções de SST possuem altos erros associados [Cronin, 2009] e que diferentes modelos terão diferentes respostas da AMOC e de SST à mesma descarga de água doce [Weaver et al., 2012]. Uma forma de contornar este viés intrínseco dos modelos é através da comparação de campos espaciais e anomalias temporais de traçadores passivos, como por exemplo a razão isotópica de oxigênio ($\delta^{18}O$). Isto deve-se especialmente a dois motivos. Primeiramente, a $\delta^{18}O$ deriva diretamente da análise química de registros sedimentares e é a variável efetivamente usada para se reconstruir a paleotemperatura (Sessao IV.1). Portanto a comparação direta de $\delta^{18}O$ entre modelos e proxies elimina da análise os erros de SST nos *paleoproxies,* relativos às funções de transferência empíricas. Um segundo motivo está no fato de os mantos de gelo polares possuírem baixíssimas concentrações do isótopo mais pesado de oxigênio (^{18}O) e altas concentrações do isótopo leve (^{16}O), conferindo a estes uma baixa razão isotópica (Fig IV.1). Assim, quando estes mantos de gelo derretem, eles adicionam ^{16}O nos oceanos, reduzindo então a razão isotópica na superfície oceânica. Portanto, sabendo-se a assinatura isotópica do manto de gelo e a magnitude da diminuição da $\delta^{18}O$ nos oceanos durante período de interesse pode-se reconstruir o quanto de água de degelo foi adicionado aos oceanos.

Reminiscentes do manto do LIS ainda são presentes no Hemisfério Norte e possuem assinatura isotópica conhecida [Fisher et al., 1998], permitindo a execução de estudos de sensibilidade que utilizem $\delta^{18}O$ como base de comparação. Levando em consideração a maior confiabilidade na $\delta^{18}O$ para reconstrução de forçantes de degelo, a primeira parte desta tese focou em estimar a magnitude da descarga de água doce do 8,2 ka comparando $\delta^{18}O$ de 28 simulações do sistema terrestre com as obtidas em 35

paleoproxies [Morrill et al., 2013] e assumindo que a simulação que melhor representa os campos de $\delta^{18}O$ dos *paleoproxies* é a que possui a forçante mais realística. Os resultados desta comparação demonstram que 7,5 m de água doce (em SLR) liberados durante 1000 anos fornecem a melhor representação do evento de 8,2 ka AP. Um fluxo complexo envolvendo um lento derretimento do LIS (0,066 Sv entre 9 e 8 ka AP) e o evento de transposição de descarga continental do rio *St. Lawrence* (0,19 Sv em 130 anos) perfazem uma forçante transiente capaz de melhor explicar as alterações no registro isotópico para o evento. Não obstante, o estudo demonstra que a AMOC possivelmente desacelerou em 62% seu revolvimento devido às descargas de água doce no início do Holoceno.

O segundo foco desta tese foi reconstruir a resposta do Atlântico Sul e da América do Sul à desaceleração da AMOC durante o 8,2 ka AP. Para isto, utilizou-se uma análise comparativa de precipitação e SSTs em simulações do 8,2 ka AP e *paleoproxies*. Através desta análise, foi possível observar uma aceleração do SAMS em resposta a uma persistente tendência negativa do SASD no Atlântico Sul durante o 8,2 ka AP e propor um possível mecanismo de acoplamento entre a intensidade de AMOC e as fases do SASD. A persistência de um dipolo negativo no SASD durante o início do Holoceno já havia sido proposta por Wainer et al. [2014] e, portanto, o avanço da análise feita nesta tese está em atribuir tal dipolo negativo à descarga de água doce no hemisfério norte e em propor um mecanismo de acoplamento entre a desaceleração da AMOC e a fase negativa do SASD [Aguiar et al., 2020; capítulo VII].

De acordo com a análise do capítulo VII, o mecanismo responsável pela persistente tendência negativa no SASD entre 9 ka AP e 8 ka AP deve-se a um aquecimento desigual da superfície do Atlântico Sul em resposta à desaceleração da

AMOC. À medida que a AMOC desacelera no início do Holoceno, calor é armazenado no Atlântico Sul e os ventos alísios de sudeste desaceleram. A desaceleração dos alísios de sudeste permite que o transporte de *Ekman* para sudoeste na região tropical seja diminuído, causando levantamento isotermal no sudoeste do Atlântico Sul e maior mistura das águas de superfície com as águas frias sub-termoclina (Fig VIII.1). Esta maior mistura permite então que o sudoeste do Atlântico Sul aqueça a uma velocidade menor do que o polo nordeste do SASD, desenvolvendo então o padrão de SST relativo ao SASD negativo. A partir do estabelecimento de um SASD negativo, a maior evaporação no nordeste do Atlântico Sul, devido às anomalias positivas de SST, permite uma maior a saturação de vapor d'água nas massas de ar tropicais, assim aumentando a intensidade de precipitação devido ao SAMS no nordeste da América do Sul [Wainer et al., 2015]. O processo inverso ocorre quando os fluxos de água doce cessam no Atlântico Norte, permitindo uma re-aceleração da AMOC e arrefecimento do SAMS (Fig VIII.1). Nossa análise demonstra que este mecanismo foi capaz de modular em até 50% a intensidade da precipitação devido ao SAMS.

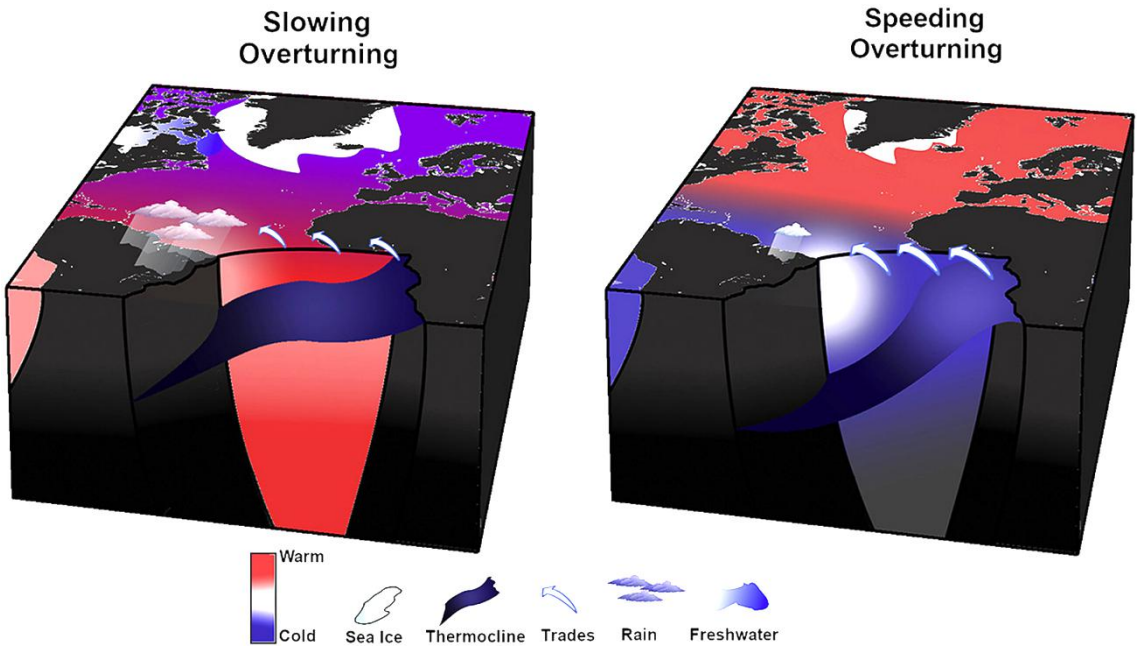

Figura VIII.1 Desenho esquemático do mecanismo proposto para o controle do SASD pela AMOC e ventos alísios. [Aguiar el al., 2020]

VIII.2 Conclusões e perspectivas futuras

A comparação entre os valores obtidos para a descarga de água doce geradora do 8,2 ka AP e as projeções de derretimento do GIS demonstram um padrão importante: os fluxos de água doce projetados para derretimento do GIS nos cenários de alta emissão de CO_2 do RCP8.5 são extremamente similares aos obtidos para o 8,2 ka AP, tanto em termos de magnitude total de adição de água doce no Hemisfério Norte (7,2 m em SLR para o RCP8.5 - [Aschwanden et al., 2019]) quanto em duração (1000 anos - [Aschwanden et al., 2019]). Esta similaridade trás novamente à tona a hipótese do 8,2 ka AP ser considerado um análogo para futuras alterações da AMOC devido ao derretimento do GIS.

No entanto, é importante salientar que os cenários futuros de desaceleração da AMOC incluem uma forçante radiativa muito maior que o início do Holoceno, devido a maior concentração de dióxido de carbono atmosférico no RCP8.5. Esta maior forçante radiativa contribuirá para um maior aquecimento e estratificação no Atlântico Norte, potencialmente desacelerando ainda mais a AMOC do que os 62% de diminuição estimados para o 8,2 ka AP. Ainda assim, as estimativas de descarga de água doce encontradas nesta tese são extremamente similares às projeções futuras de derretimento do GIS, confirmando que o 8,2 ka AP é um possível análogo para os efeitos do derretimento do GIS sobre a AMOC nos cenários de intenso aumento nas concentrações de dióxido de carbono.

Os resultados obtidos nesta tese demonstram também que a desaceleração da AMOC durante o 8,2 ka AP possivelmente causou uma intensificação do SAMS, alterando o clima da América do Sul. Este resultado, quando interpretado junto com a hipótese do 8,2 ka AP como análogo da futura desaceleração da AMOC no século 21, levanta a possibilidade de aumento na intensidade do SAMS durante o século 21. De fato, estimativas baseadas nas fases 5 e 6 do *Coupled Model Intercomparison Project* (CMIP5 e CMIP6) demonstram um aumento na precipitação durante o verão devido ao SAMS ao final do século 21 [Jones & Carvalho, 2013; Wang et al., 2021] e uma extensão da estação chuvosa [Kitoh et al., 2013] nos cenários RCP8.5 e SSP2-4.5. No entanto, a relação entre a futura desaceleração da AMOC nestes estudos e a intensidade do SAMS não foi explorada. Nota-se ainda que a maior parte dos modelos utilizados nos CMIP5 e CMIP6 não incluem a dinâmica das plataforma de gelo continental [Taylor et al., 2012; Eyring et al., 2016] e, portanto, não projetam a desaceleração da AMOC devido ao derretimento do manto de gelo da Groenlândia - mas somente como resposta a maior estratificação do Atlântico Norte. Se o mecanismo de controle do SAMS por descargas de água doce proposto para o 8,2 ka é válido para projeções futuras, então é esperado que a intensificação do SAMS no século 21 seja ainda maior do que projetada nos CMIPs. Pensando nisto, estudos futuros devem se ater a entender se os mecanismos de controle do SAMS pela AMOC propostos para o 8,2 ka AP nesta tese são válidos para projeções climáticas do século 21.

Capítulo IX: Referências

Aguiar, W., Meissner, K.J., Montenegro, A., Prado, L., Wainer, I., Carlson, A.E., Mata, M.M., 2021. Magnitude of the 8.2 ka event freshwater forcing based on stable isotope modelling and comparison to future Greenland melting. Sci. Rep. 11, 5473. https://doi.org/10.1038/s41598-021-84709-5

Aguiar, W., Prado, L.F., Wainer, I., Liu, Z., Montenegro, A., Meissner, K.J., Mata, M.M., 2020. Freshwater forcing control on early-Holocene South American monsoon. Quat. Sci. Rev. 245, 106498. https://doi.org/10.1016/j.quascirev.2020.106498

Alley, R., Agustsdottir, A., 2005. The 8k event: cause and consequences of a major Holocene abrupt climate change. Quat. Sci. Rev. 24, 1123–1149. https://doi.org/10.1016/j.quascirev.2004.12.004

Alley, R.B., 2000. The Younger Dryas cold interval as viewed from central Greenland. Quat. Sci. Rev. 19, 213–226. https://doi.org/10.1016/S0277-3791(99)00062-1

Alley, R.B., Mayewski, P.A., Sowers, T., Stuiver, M., Taylor, K.C., Clark, P.U., 1997. Holocene climatic instability: A prominent, widespread event 8200 yr ago. Geology 26, 483–486. https://doi.org/10.1130/0091-7613(1997)025<0483:HCIAPW>2.3.CO;2

Andreoli, R.V., Kayano, M.T., 2007. A importância relativa do atlântico tropical sul e pacífico leste na variabilidade de precipitação do Nordeste do Brasil. Rev. Bras. Meteorol. 22, 63–74. https://doi.org/10.1590/S0102-77862007000100007

Archer, D., 1996. A data-driven model of the global calcite lysocline. Glob. Biogeochem. Cycles 10, 511–526. https://doi.org/10.1029/96GB01521

Arz, H.W., Gerhardt, S., Pätzold, J., Röhl, U., 2001. Millennial-scale changes of surface- and deep-water flow in the western tropical Atlantic linked to Northern Hemisphere high-latitude climate during the Holocene. Geology 29, 239–242. https://doi.org/10.1130/0091-7613(2001)029<0239:MSCOSA>2.0.CO;2

Aschwanden, A., Fahnestock, M.A., Truffer, M., Brinkerhoff, D.J., Hock, R., Khroulev, C., Mottram, R., Khan, S.A., 2019. Contribution of the Greenland Ice Sheet to sea level over the next millennium. Sci. Adv. 5, eaav9396. https://doi.org/10.1126/sciadv.aav9396

Bagniewski, W., Meissner, K.J., Menviel, L., 2017. Exploring the oxygen isotope fingerprint of Dansgaard-Oeschger variability and Heinrich events. Quat. Sci. Rev. 159, 1–14. https://doi.org/10.1016/j.quascirev.2017.01.007

Bagniewski, W., Meissner, K.J., Menviel, L., Brennan, C.E., 2015. Quantification of factors impacting seawater and calcite δ^{18}O during Heinrich Stadials 1 and 4: δ^{18}O DURING HEINRICH STADIALS. Paleoceanography 30, 895–911. https://doi.org/10.1002/2014PA002751

Bakker, P., Schmittner, A., Lenaerts, J.T.M., Abe-Ouchi, A., Bi, D., van den Broeke, M.R., Chan, W.-L., Hu, A., Beadling, R.L., Marsland, S.J., Mernild, S.H., Saenko, O.A., Swingedouw, D., Sullivan, A., Yin, J., 2016. Fate of the Atlantic Meridional Overturning Circulation: Strong decline under continued warming and Greenland melting: AMOC PROJECTIONS FOR WARMING AND GIS MELT. Geophys. Res. Lett. 43, 12,252-12,260. https://doi.org/10.1002/2016GL070457

Barber, D.C., Dyke, A., Hillaire-Marcel, C., Jennings, A.E., Andrews, J.T., Kerwin, M.W., Bilodeau, G., McNeely, R., Southon, J., Morehead, M.D., Gagnon, J.-M., 1999. Forcing of the cold event of 8,200 years ago by catastrophic drainage of Laurentide lakes. Nature 400, 344–348. https://doi.org/10.1038/22504

Bemis, B.E., Spero, H.J., Bijma, J., Lea, D.W., 1998. Reevaluation of the oxygen isotopic composition of planktonic foraminifera: Experimental results and revised paleotemperature equations. Paleoceanography 13, 150–160. https://doi.org/10.1029/98PA00070

Berger, A.L., 1978. Long-Term Variations of Caloric Insolation Resulting from the Earth's Orbital Elements. Quat. Res. 9, 139–167. https://doi.org/10.1016/0033-5894(78)90064-9

Bintanja, R., Selten, F.M., 2014. Future increases in Arctic precipitation linked to local evaporation and sea-ice retreat. Nature 509, 479–482. https://doi.org/10.1038/nature13259

Bond, G., Broecker, W., Johnsen, S., McManus, J., Labeyrie, L., Jouzel, J., Bonani, G., 1993. Correlations between climate records from North Atlantic sediments and Greenland ice. Nature 365, 143–147. https://doi.org/10.1038/365143a0

Boville, B.A., Gent, P.R., 1998. The NCAR Climate System Model, Version One. J. Clim. 11, 1115–1130. https://doi.org/10.1175/1520-0442(1998)011<1115:TNCSMV>2.0.CO;2

Brennan, C.E., Meissner, K.J., Eby, M., Hillaire-Marcel, C., Weaver, A.J., 2013. Impact of sea ice variability on the oxygen isotope content of seawater under glacial and interglacial conditions: SEA ICE VARIABILITY AND SEAWATER δ^{18} O. Paleoceanography 28, 388–400. https://doi.org/10.1002/palo.20036

Brennan, C.E., Weaver, A.J., Eby, M., Meissner, K.J., 2012. Modelling Oxygen Isotopes in the University of Victoria Earth System Climate Model for Pre-industrial and Last Glacial Maximum Conditions. Atmosphere-Ocean 50, 447–465. https://doi.org/10.1080/07055900.2012.707611

Briggs, R.D., Tarasov, L., 2013. How to evaluate model-derived deglaciation chronologies: a case study using Antarctica. Quat. Sci. Rev. 63, 109–127. https://doi.org/10.1016/j.quascirev.2012.11.021

Broecker, W., Bond, G., Klas, M., Clark, E., McManus, J., 1992. Origin of the northern Atlantic's Heinrich events. Clim. Dyn. 6, 265–273. https://doi.org/10.1007/BF00193540

Broecker, W.S., 1998. Paleocean circulation during the Last Deglaciation: A bipolar seesaw? Paleoceanography 13, 119–121. https://doi.org/10.1029/97PA03707

Broecker, W.S., Olson, E.A., Orr, P.C., 1960. Radiocarbon Measurements and Annual Rings in Cave Formations. Nature 185, 93–94. https://doi.org/10.1038/185093a0

Cai, W., McPhaden, M.J., Grimm, A.M., Rodrigues, R.R., Taschetto, A.S., Garreaud, R.D., Dewitte, B., Poveda, G., Ham, Y.-G., Santoso, A., Ng, B., Anderson, W., Wang, G., Geng, T., Jo, H.-S., Marengo, J.A., Alves, L.M., Osman, M., Li, S., Wu, L., Karamperidou, C., Takahashi, K., Vera, C., 2020. Climate impacts of the El Niño–Southern Oscillation on South America. Nat. Rev. Earth Environ. 1, 215–231. https://doi.org/10.1038/s43017-020-0040-3

Carlson, A. E., Anslow, F.S., Obbink, E.A., LeGrande, A.N., Ullman, D.J., Licciardi, J.M., 2009. Surface-melt driven Laurentide Ice Sheet retreat during the early Holocene. Geophys. Res. Lett. 36, L24502. https://doi.org/10.1029/2009GL040948

Carlson, Anders E., Clark, P.U., Haley, B.A., Klinkhammer, G.P., 2009. Routing of western Canadian Plains runoff during the 8.2 ka cold event. Geophys. Res. Lett. 36, L14704. https://doi.org/10.1029/2009GL038778

Carlson, A.E., LeGrande, A.N., Oppo, D.W., Came, R.E., Schmidt, G.A., Anslow, F.S., Licciardi, J.M., Obbink, E.A., 2008. Rapid early Holocene deglaciation of the Laurentide ice sheet. Nat. Geosci. 1, 620–624. https://doi.org/10.1038/ngeo285

Cavalcanti, I.F.A., 2012. Large scale and synoptic features associated with extreme precipitation over South America: A review and case studies for the first decade of the 21st century. Atmospheric Res. 118, 27–40. https://doi.org/10.1016/j.atmosres.2012.06.012

Cazenave, A., 2006. How Fast Are the Ice Sheets Melting? Science 314, 1250–1252. https://doi.org/10.1126/science.1133325

Cheng, W., Chiang, J.C.H., Zhang, D., 2013. Atlantic Meridional Overturning Circulation (AMOC) in CMIP5 Models: RCP and Historical Simulations. J. Clim. 26, 7187–7197.

https://doi.org/10.1175/JCLI-D-12-00496.1
Clark, P.U., 2001. Freshwater Forcing of Abrupt Climate Change During the Last Glaciation. Science 293, 283–287. https://doi.org/10.1126/science.1062517
Clark, P.U., Pisias, N.G., Stocker, T.F., Weaver, A.J., 2002. The role of the thermohaline circulation in abrupt climate change. Nature 415, 863–869. https://doi.org/10.1038/415863a
Clark, P.U., Shakun, J.D., Baker, P.A., Bartlein, P.J., Brewer, S., Brook, E., Carlson, A.E., Cheng, H., Kaufman, D.S., Liu, Z., Marchitto, T.M., Mix, A.C., Morrill, C., Otto-Bliesner, B.L., Pahnke, K., Russell, J.M., Whitlock, C., Adkins, J.F., Blois, J.L., Clark, J., Colman, S.M., Curry, W.B., Flower, B.P., He, F., Johnson, T.C., Lynch-Stieglitz, J., Markgraf, V., McManus, J., Mitrovica, J.X., Moreno, P.I., Williams, J.W., 2012. Global climate evolution during the last deglaciation. Proc. Natl. Acad. Sci. 109, E1134–E1142. https://doi.org/10.1073/pnas.1116619109
Clarke, G., Leverington, D., Teller, J., Dyke, A., 2003. Superlakes, Megafloods, and Abrupt Climate Change. Science 301, 922. https://doi.org/10.1126/science.1085921
Clarke, G.K.C., Leverington, D.W., Teller, J.T., Dyke, A.S., 2004. Paleohydraulics of the last outburst flood from glacial Lake Agassiz and the 8200BP cold event. Quat. Sci. Rev. 23, 389–407. https://doi.org/10.1016/j.quascirev.2003.06.004
Craig, H., 1961. Isotopic Variations in Meteoric Waters. Science 133, 1702–1703. https://doi.org/10.1126/science.133.3465.1702
Cronin, T.M., 2009. Paleotemperatures and Proxy Reconstructions, in: Gornitz, V. (Ed.), Encyclopedia of Paleoclimatology and Ancient Environments, Encyclopedia of Earth Sciences Series. Springer Netherlands, Dordrecht, pp. 757–763. https://doi.org/10.1007/978-1-4020-4411-3_180
Dansgaard, W., Johnsen, S.J., Clausen, H.B., Dahl-Jensen, D., Gundestrup, N.S., Hammer, C.U., Hvidberg, C.S., Steffensen, J.P., Sveinbjörnsdottir, A.E., Jouzel, J., Bond, G., 1993. Evidence for general instability of past climate from a 250-kyr ice-core record. Nature 364, 218–220. https://doi.org/10.1038/364218a0
Davies, F.J., Renssen, H., Goosse, H., 2014. The Arctic freshwater cycle during a naturally and an anthropogenically induced warm climate. Clim. Dyn. 42, 2099–2112. https://doi.org/10.1007/s00382-013-1849-y
Dean, W.E., Schwalb, A., 2000. Holocene environmental and climatic change in the Northern Great Plains as recorded in the geochemistry of sediments in Pickerel Lake, South Dakota. Quat. Int. 67, 5–20. https://doi.org/10.1016/S1040-6182(00)00004-5
Denton, G.H., Karlén, W., 1973. Holocene Climatic Variations—Their Pattern and Possible Cause. Quat. Res. 3, 155–205. https://doi.org/10.1016/0033-5894(73)90040-9
Diebold, F.X., Mariano, R.S., 2002. Comparing Predictive Accuracy. J. Bus. Econ. Stat. 20, 134–144. https://doi.org/10.1198/073500102753410444
Epstein, S., Mayeda, T., 1953. Variation of O18 content of waters from natural sources. Geochim. Cosmochim. Acta 4, 213–224. https://doi.org/10.1016/0016-7037(53)90051-9
Eyring, V., Bony, S., Meehl, G.A., Senior, C.A., Stevens, B., Stouffer, R.J., Taylor, K.E., 2016. Overview of the Coupled Model Intercomparison Project Phase 6 (CMIP6) experimental design and organization. Geosci. Model Dev. 9, 1937–1958. https://doi.org/10.5194/gmd-9-1937-2016
Fauchereau, N., Trzaska, S., Richard, Y., Roucou, P., Camberlin, P., 2003. Sea-surface temperature co-variability in the Southern Atlantic and Indian Oceans and its connections with the atmospheric circulation in the Southern Hemisphere. Int. J. Climatol. 23, 663–677. https://doi.org/10.1002/joc.905
Fettweis, X., Box, J.E., Agosta, C., Amory, C., Kittel, C., Lang, C., van As, D., Machguth, H., Gallée, H., 2017. Reconstructions of the 1900–2015 Greenland ice sheet surface mass balance using the regional climate MAR model. The Cryosphere 11, 1015–1033. https://doi.org/10.5194/tc-11-1015-2017
Fisher, D.A., Koerner, R.M., Bourgeois, J.C., Zielinski, G., Wake, C., Hammer, C.U., Clausen, H.B., Gundestrup, N., Johnsen, S., Goto-Azuma, K., Hondoh, T., Blake, E., Gerasimoff, M., 1998. Penny Ice Cap Cores, Baffin Island, Canada, and the Wisconsinan Foxe Dome Connection: Two States of Hudson Bay Ice Cover. Science 279, 692–695. https://doi.org/10.1126/science.279.5351.692
Gan, M.A., Rao, V.B., Moscati, M.C.L., 2005. South American monsoon indices. Atmospheric Sci. Lett. 6, 219–223. https://doi.org/10.1002/asl.119
García-Ibáñez, M.I., Pardo, P.C., Carracedo, L.I., Mercier, H., Lherminier, P., Ríos, A.F., Pérez, F.F., 2015. Structure, transports and transformations of the water masses in the Atlantic Subpolar Gyre. Prog. Oceanogr. 135, 18–36. https://doi.org/10.1016/j.pocean.2015.03.009

Golledge, N.R., Keller, E.D., Gomez, N., Naughten, K.A., Bernales, J., Trusel, L.D., Edwards, T.L., 2019. Global environmental consequences of twenty-first-century ice-sheet melt. Nature 566, 65–72. https://doi.org/10.1038/s41586-019-0889-9

Gonfiantini, R., 1984. Stable Isotope Reference Samples for Geochemical and Hydrological Investigations. Int. J. Appl. Radiat. Isot. 35, 426. https://doi.org/10.1016/0020-708X(84)90059-0

Gregoire, L.J., Payne, A.J., Valdes, P.J., 2012. Deglacial rapid sea level rises caused by ice-sheet saddle collapses. Nature 487, 219–222. https://doi.org/10.1038/nature11257

Hays, J.D., Imbrie, J., Shackleton, N.J., 1976. Variations in the Earth's Orbit: Pacemaker of the Ice Ages. Science 194, 1121–1132. https://doi.org/10.1126/science.194.4270.1121

He, F., 2011. Simulating transient climate evolution of the last deglaciation with CCSM3.

Hein, M., F., J., Smethie, W. M., Smythe-Wright, D., Weiss, R.F., Merteins, C., Min, D.H., Fleischmann, U., Putzka, A., 2002. Labrador Sea Water: Pathways, CFC Inventory, and Formation Rates. J. Phys. Oceanogr. 32, 648–665. https://doi.org/10.1175/1520-0485(2002)032<0648:LSWPCI>2.0.CO;2

Hendy, C.H., Wilson, A.T., 1968. Palaeoclimatic Data from Speleothems. Nature 219, 48–51. https://doi.org/10.1038/219048a0

Hermes, J.C., Reason, C.J.C., 2005. Ocean Model Diagnosis of Interannual Coevolving SST Variability in the South Indian and South Atlantic Oceans. J. Clim. 18, 2864–2882. https://doi.org/10.1175/JCLI3422.1

Hibler III, W.D., 1979. A Dynamic Thermodynamic Sea Ice Model. J. Phys. Oceanogr. 9, 815–846. https://doi.org/10.1175/1520-0485(1979)009<0815:ADTSIM>2.0.CO;2

Hijma, M.P., Cohen, K.M., 2010. Timing and magnitude of the sea-level jump preluding the 8200 yr event. Geology 38, 275–278. https://doi.org/10.1130/G30439.1

Hughen, K.A., Overpeck, J.T., Peterson, L.C., Trumbore, S., 1996. Rapid climate changes in the tropical Atlantic region during the last deglaciation. Nature 380, 51–54. https://doi.org/10.1038/380051a0

Jones, C., Carvalho, L.M.V., 2013. Climate Change in the South American Monsoon System: Present Climate and CMIP5 Projections. J. Clim. 26, 6660–6678. https://doi.org/10.1175/JCLI-D-12-00412.1

Joos, F., Spahni, R., 2008. Rates of change in natural and anthropogenic radiative forcing over the past 20,000 years. Proc. Natl. Acad. Sci. 105, 1425–1430. https://doi.org/10.1073/pnas.0707386105

Jouzel, J., Koster, R.D., Suozzo, R.J., Russell, G.L., 1994. Stable water isotope behavior during the last glacial maximum: A general circulation model analysis. J. Geophys. Res. 99, 25791. https://doi.org/10.1029/94JD01819

Kalnay, E., Kanamitsu, M., Kistler, R., Collins, W., Deaven, D., Gandin, L., Iredell, M., Saha, S., White, G., Woollen, J., Zhu, Y., Chelliah, M., Ebisuzaki, W., Higgins, W., Janowiak, J., Mo, K.C., Ropelewski, C., Wang, J., Leetmaa, A., Reynolds, R., Jenne, R., Joseph, D., 1996. The NCEP/NCAR 40-Year Reanalysis Project. Bull. Am. Meteorol. Soc. 77, 437–472. https://doi.org/10.1175/1520-0477(1996)077<0437:TNYRP>2.0.CO;2

Kaufman, D., 2004. Holocene thermal maximum in the western Arctic (0–180°W). Quat. Sci. Rev. 23, 529–560. https://doi.org/10.1016/j.quascirev.2003.09.007

Kim, S.-T., O'Neil, J.R., 1997. Equilibrium and nonequilibrium oxygen isotope effects in synthetic carbonates. Geochim. Cosmochim. Acta 61, 3461–3475. https://doi.org/10.1016/S0016-7037(97)00169-5

Kitoh, A., Endo, H., Krishna Kumar, K., Cavalcanti, I.F.A., Goswami, P., Zhou, T., 2013. Monsoons in a changing world: A regional perspective in a global context. J. Geophys. Res. Atmospheres 118, 3053–3065. https://doi.org/10.1002/jgrd.50258

Kleiven, H.F., Kissel, C., Laj, C., Ninnemann, U.S., Richter, T.O., Cortijo, E., 2008. Reduced North Atlantic Deep Water Coeval with the Glacial Lake Agassiz Freshwater Outburst. Science 319, 60–64. https://doi.org/10.1126/science.1148924

Klitgaard-Kristensen, D., Sejrup, H.P., Haflidason, H., Johnsen, S., Spurk, M., 1998. A regional 8200 cal. yr BP cooling event in northwest Europe, induced by final stages of the Laurentide ice-sheet deglaciation? J. Quat. Sci. 13, 165–169. https://doi.org/10.1002/(SICI)1099-1417(199803/04)13:2<165::AID-JQS365>3.0.CO;2-#

Kneller, M., Peteet, D., 1999. Late-Glacial to Early Holocene Climate Changes from a Central Appalachian Pollen and Macrofossil Record. Quat. Res. 51, 133–147. https://doi.org/10.1006/qres.1998.2026

Lawrence, T., Long, A.J., Gehrels, W.R., Jackson, L.P., Smith, D.E., 2016. Relative sea-level data from

southwest Scotland constrain meltwater-driven sea-level jumps prior to the 8.2 kyr BP event. Quat. Sci. Rev. 151, 292–308. https://doi.org/10.1016/j.quascirev.2016.06.013

LeGrande, A.N., Schmidt, G.A., Shindell, D.T., Field, C.V., Miller, R.L., Koch, D.M., Faluvegi, G., Hoffmann, G., 2006. Consistent simulations of multiple proxy responses to an abrupt climate change event. Proc. Natl. Acad. Sci. 103, 837–842. https://doi.org/10.1073/pnas.0510095103

Lenaerts, J.T.M., Le Bars, D., van Kampenhout, L., Vizcaino, M., Enderlin, E.M., van den Broeke, M.R., 2015. Representing Greenland ice sheet freshwater fluxes in climate models: GREENLAND FRESHWATER FORCING. Geophys. Res. Lett. 42, 6373–6381. https://doi.org/10.1002/2015GL064738

Li, Y.-X., Törnqvist, T.E., Nevitt, J.M., Kohl, B., 2012. Synchronizing a sea-level jump, final Lake Agassiz drainage, and abrupt cooling 8200years ago. Earth Planet. Sci. Lett. 315–316, 41–50. https://doi.org/10.1016/j.epsl.2011.05.034

Liebmann, B., Marengo, JoséA., 2001. Interannual Variability of the Rainy Season and Rainfall in the Brazilian Amazon Basin. J. Clim. 14, 4308–4318. https://doi.org/10.1175/1520-0442(2001)014<4308:IVOTRS>2.0.CO;2

Liebmann, B., Mechoso, C.R., 2011. THE SOUTH AMERICAN MONSOON SYSTEM, in: World Scientific Series on Asia-Pacific Weather and Climate. WORLD SCIENTIFIC, pp. 137–157. https://doi.org/10.1142/9789814343411_0009

Liebmann, B., Vera, C.S., Carvalho, L.M.V., Camilloni, I.A., Hoerling, M.P., Allured, D., Barros, V.R., Báez, J., Bidegain, M., 2004. An Observed Trend in Central South American Precipitation. J. Clim. 17, 4357–4367. https://doi.org/10.1175/3205.1

Ljung, K., Björck, S., Renssen, H., Hammarlund, D., 2008. South Atlantic island record reveals a South Atlantic response to the 8.2 kyr event. Clim. Past 4, 35–45. https://doi.org/10.5194/cp-4-35-2008

Marengo, J.A., Alves, L.M., Alvala, R.C.S., Cunha, A.P., Brito, S., Moraes, O.L.L., 2018. Climatic characteristics of the 2010-2016 drought in the semiarid Northeast Brazil region. An. Acad. Bras. Ciênc. 90, 1973–1985. https://doi.org/10.1590/0001-3765201720170206

Marson, J.M., Wainer, I., Mata, M.M., Liu, Z., 2014. The impacts of deglacial meltwater forcing on the South Atlantic Ocean deep circulation since the Last Glacial Maximum. Clim. Past 10, 1723–1734. https://doi.org/10.5194/cp-10-1723-2014

Matero, I.S.O., Gregoire, L.J., Ivanovic, R.F., Tindall, J.C., Haywood, A.M., 2017. The 8.2 ka cooling event caused by Laurentide ice saddle collapse. Earth Planet. Sci. Lett. 473, 205–214. https://doi.org/10.1016/j.epsl.2017.06.011

Meissner, K.J., Clark, P.U., 2006. Impact of floods versus routing events on the thermohaline circulation. Geophys. Res. Lett. 33, L15704. https://doi.org/10.1029/2006GL026705

Meissner, K.J., Weaver, A.J., Matthews, H.D., Cox, P.M., 2003. The role of land surface dynamics in glacial inception: a study with the UVic Earth System Model. Clim. Dyn. 21, 515–537. https://doi.org/10.1007/s00382-003-0352-2

Morioka, Y., Tozuka, T., Yamagata, T., 2011. On the Growth and Decay of the Subtropical Dipole Mode in the South Atlantic. J. Clim. 24, 5538–5554. https://doi.org/10.1175/2011JCLI4010.1

Morrill, C., Anderson, D.M., Bauer, B.A., Buckner, R., Gille, E.P., Gross, W.S., Hartman, M., Shah, A., 2013. Proxy benchmarks for intercomparison of 8.2 ka simulations. Clim. Past 9, 423–432. https://doi.org/10.5194/cp-9-423-2013

Morrill, C., Jacobsen, R.M., 2005. How widespread were climate anomalies 8200 years ago?: CLIMATE ANOMALIES 8200 YEARS AGO. Geophys. Res. Lett. 32, n/a-n/a. https://doi.org/10.1029/2005GL023536

Morrill, C., Ward, E.M., Wagner, A.J., Otto-Bliesner, B.L., Rosenbloom, N., 2014. Large sensitivity to freshwater forcing location in 8.2 ka simulations. Paleoceanography 29, 930–945. https://doi.org/10.1002/2014PA002669

Otto-Bliesner, B.L., Brady, E.C., Clauzet, G., Tomas, R., Levis, S., Kothavala, Z., 2006. Last Glacial Maximum and Holocene Climate in CCSM3. J. Clim. 19, 2526–2544. https://doi.org/10.1175/JCLI3748.1

Pacanowski, R.C., 1996. Documentation user's guide and reference manual (MOM2, Version 2) (Thecnical Report). GFDL Ocean Technical Report.

Pedro, J.B., Jochum, M., Buizert, C., He, F., Barker, S., Rasmussen, S.O., 2018. Beyond the bipolar seesaw: Toward a process understanding of interhemispheric coupling. Quat. Sci. Rev. 192, 27–46. https://doi.org/10.1016/j.quascirev.2018.05.005

Peltier, W.R., 2004. GLOBAL GLACIAL ISOSTASY AND THE SURFACE OF THE ICE-AGE EARTH: The ICE-5G (VM2) Model and GRACE. Annu. Rev. Earth Planet. Sci. 32, 111–149.

https://doi.org/10.1146/annurev.earth.32.082503.144359
Rahmstorf, S., Box, J.E., Feulner, G., Mann, M.E., Robinson, A., Rutherford, S., Schaffernicht, E.J., 2015. Exceptional twentieth-century slowdown in Atlantic Ocean overturning circulation. Nat. Clim. Change 5, 475–480. https://doi.org/10.1038/nclimate2554
Remenda, V.H., Cherry, J.A., Edwards, T.W.D., 1994. Isotopic Composition of Old Ground Water from Lake Agassiz: Implications for Late Pleistocene Climate. Science 266, 1975–1978. https://doi.org/10.1126/science.266.5193.1975
Rodrigues, R.R., Haarsma, R.J., Campos, E.J.D., Ambrizzi, T., 2011. The Impacts of Inter–El Niño Variability on the Tropical Atlantic and Northeast Brazil Climate. J. Clim. 24, 3402–3422. https://doi.org/10.1175/2011JCLI3983.1
Schmidt, G., Legrande, A., 2005. The Goldilocks abrupt climate change event. Quat. Sci. Rev. 24, 1109–1110. https://doi.org/10.1016/j.quascirev.2005.01.015
Seppä, H., Birks, H.J.B., 2001. July mean temperature and annual precipitation trends during the Holocene in the Fennoscandian tree-line area: pollen-based climate reconstructions. The Holocene 11, 527–539. https://doi.org/10.1191/095968301680223486
Seppä, H., Poska, A., 2004. Holocene annual mean temperature changes in Estonia and their relationship to solar insolation and atmospheric circulation patterns. Quat. Res. 61, 22–31. https://doi.org/10.1016/j.yqres.2003.08.005
Sévellec, F., Fedorov, A.V., Liu, W., 2017. Arctic sea-ice decline weakens the Atlantic Meridional Overturning Circulation. Nat. Clim. Change 7, 604–610. https://doi.org/10.1038/nclimate3353
Silva, S.F., Genz, F., Aguiar, W., Silva, N., Kiperstok, A., 2013. Avaliação da ocorrência de secas na Bahia utilizando o Índice de Precipitação Padronizada (SPI). Bahia Análise E Dados 23, 461–473.
Silva, V.B., Kousky, V., 2012. The South American Monsoon System: Climatology and Variability, in: Wang, S.-Y.S. (Ed.), Modern Climatology. InTech. https://doi.org/10.5772/38565
Smith, D.E., Harrison, S., Jordan, J.T., 2013. Sea level rise and submarine mass failures on open continental margins. Quat. Sci. Rev. 82, 93–103. https://doi.org/10.1016/j.quascirev.2013.10.012
Srokosz, M.A., Bryden, H.L., 2015. Observing the Atlantic Meridional Overturning Circulation yields a decade of inevitable surprises. Science 348, 1255575–1255575. https://doi.org/10.1126/science.1255575
Sterl, A., Hazeleger, W., 2003. Coupled variability and air-sea interaction in the South Atlantic Ocean. Clim. Dyn. 21, 559–571. https://doi.org/10.1007/s00382-003-0348-y
Stocker, T.F., Johnsen, S.J., 2003. A minimum thermodynamic model for the bipolar seesaw: THERMAL BIPOLAR SEESAW. Paleoceanography 18, n/a-n/a. https://doi.org/10.1029/2003PA000920
Streif, H., 2004. Sedimentary record of Pleistocene and Holocene marine inundations along the North Sea coast of Lower Saxony, Germany. Quat. Int. 112, 3–28. https://doi.org/10.1016/S1040-6182(03)00062-4
Swingedouw, D., Braconnot, P., Delecluse, P., Guilyardi, E., Marti, O., 2007. Quantifying the AMOC feedbacks during a 2×CO2 stabilization experiment with land-ice melting. Clim. Dyn. 29, 521–534. https://doi.org/10.1007/s00382-007-0250-0
Talley, L., 2013. Closure of the Global Overturning Circulation Through the Indian, Pacific, and Southern Oceans: Schematics and Transports. Oceanography 26, 80–97. https://doi.org/10.5670/oceanog.2013.07
Taschetto, A.S., Wainer, I., 2008. The impact of the subtropical South Atlantic SST on South American precipitation. Ann. Geophys. 26, 3457–3476. https://doi.org/10.5194/angeo-26-3457-2008
Taylor, K.E., Stouffer, R.J., Meehl, G.A., 2012. An Overview of CMIP5 and the Experiment Design. Bull. Am. Meteorol. Soc. 93, 485–498. https://doi.org/10.1175/BAMS-D-11-00094.1
Tedesco, M., Fettweis, X., 2012. 21st century projections of surface mass balance changes for major drainage systems of the Greenland ice sheet. Environ. Res. Lett. 7, 045405. https://doi.org/10.1088/1748-9326/7/4/045405
Thomas, E.R., Wolff, E.W., Mulvaney, R., Steffensen, J.P., Johnsen, S.J., Arrowsmith, C., White, J.W.C., Vaughn, B., Popp, T., 2007. The 8.2ka event from Greenland ice cores. Quat. Sci. Rev. 26, 70–81. https://doi.org/10.1016/j.quascirev.2006.07.017
Ullman, D.J., Carlson, A.E., Hostetler, S.W., Clark, P.U., Cuzzone, J., Milne, G.A., Winsor, K., Caffee, M., 2016. Final Laurentide ice-sheet deglaciation and Holocene climate-sea level change. Quat. Sci. Rev. 152, 49–59. https://doi.org/10.1016/j.quascirev.2016.09.014
van den Broeke, M.R., Enderlin, E.M., Howat, I.M., Kuipers Munneke, P., Noël, B.P.Y., van de Berg, W.J., van Meijgaard, E., Wouters, B., 2016. On the recent contribution of the Greenland ice

sheet to sea level change. The Cryosphere 10, 1933–1946. https://doi.org/10.5194/tc-10-1933-2016

Venegas, S.A., Mysak, L.A., Straub, D.N., 1997. Atmosphere–Ocean Coupled Variability in the South Atlantic. J. Clim. 10, 2904–2920. https://doi.org/10.1175/1520-0442(1997)010<2904:AOCVIT>2.0.CO;2

Venegas, S.A., Mysak, L.A., Straub, D.N., 1996. Evidence for interannual and interdecadal climate variability in the South Atlantic. Geophys. Res. Lett. 23, 2673–2676. https://doi.org/10.1029/96GL02373

Vera, C., Higgins, W., Amador, J., Ambrizzi, T., Garreaud, R., Gochis, D., Gutzler, D., Lettenmaier, D., Marengo, J., Mechoso, C.R., Nogues-Paegle, J., Dias, P.L.S., Zhang, C., 2006. Toward a Unified View of the American Monsoon Systems. J. Clim. 19, 4977–5000. https://doi.org/10.1175/JCLI3896.1

Wagner, A.J., Morrill, C., Otto-Bliesner, B.L., Rosenbloom, N., Watkins, K.R., 2013. Model support for forcing of the 8.2 ka event by meltwater from the Hudson Bay ice dome. Clim. Dyn. 41, 2855–2873. https://doi.org/10.1007/s00382-013-1706-z

Wainer, I., Prado, L.F., Khodri, M., Otto-Bliesner, B., 2015. Reconstruction of the South Atlantic Subtropical Dipole index for the past 12,000 years from surface temperature proxy. Sci. Rep. 4, 5291. https://doi.org/10.1038/srep05291

Wang, B., Biasutti, M., Byrne, M.P., Castro, C., Chang, C.-P., Cook, K., Fu, R., Grimm, A.M., Ha, K.-J., Hendon, H., Kitoh, A., Krishnan, R., Lee, J.-Y., Li, J., Liu, J., Moise, A., Pascale, S., Roxy, M.K., Seth, A., Sui, C.-H., Turner, A., Yang, S., Yun, K.-S., Zhang, L., Zhou, T., 2021. Monsoons Climate Change Assessment. Bull. Am. Meteorol. Soc. 102, E1–E19. https://doi.org/10.1175/BAMS-D-19-0335.1

Weaver, A.J., Eby, M., Wiebe, E.C., Bitz, C.M., Duffy, P.B., Ewen, T.L., Fanning, A.F., Holland, M.M., MacFadyen, A., Matthews, H.D., Meissner, K.J., Saenko, O., Schmittner, A., Wang, H., Yoshimori, M., 2001. The UVic earth system climate model: Model description, climatology, and applications to past, present and future climates. Atmosphere-Ocean 39, 361–428. https://doi.org/10.1080/07055900.2001.9649686

Weaver, A.J., Sedláček, J., Eby, M., Alexander, K., Crespin, E., Fichefet, T., Philippon-Berthier, G., Joos, F., Kawamiya, M., Matsumoto, K., Steinacher, M., Tachiiri, K., Tokos, K., Yoshimori, M., Zickfeld, K., 2012. Stability of the Atlantic meridional overturning circulation: A model intercomparison. Geophys. Res. Lett. 39, 2012GL053763. https://doi.org/10.1029/2012GL053763

Webster, P.J., Magaña, V.O., Palmer, T.N., Shukla, J., Tomas, R.A., Yanai, M., Yasunari, T., 1998. Monsoons: Processes, predictability, and the prospects for prediction. J. Geophys. Res. Oceans 103, 14451–14510. https://doi.org/10.1029/97JC02719

Wiersma, A.P., Renssen, H., Goosse, H., Fichefet, T., 2006. Evaluation of different freshwater forcing scenarios for the 8.2 ka BP event in a coupled climate model. Clim. Dyn. 27, 831–849. https://doi.org/10.1007/s00382-006-0166-0

Yang, H., Zhao, Y., Liu, Z., Li, Q., He, F., Zhang, Q., 2015. Heat Transport Compensation in Atmosphere and Ocean over the Past 22,000 Years. Sci. Rep. 5, 16661. https://doi.org/10.1038/srep16661

Yeung, N.K.H., Menviel, L., Meissner, K.J., Sikes, E., 2019. Assessing the Spatial Origin of Meltwater Pulse 1A Using Oxygen-Isotope Fingerprinting. Paleoceanogr. Paleoclimatology 34, 2031–2046. https://doi.org/10.1029/2019PA003599

Yu, Z., Eicher, U., 1998. Abrupt Climate Oscillations During the Last Deglaciation in Central North America. Science 282, 2235–2238. https://doi.org/10.1126/science.282.5397.2235

Zeebe, R.E., 1999. An explanation of the effect of seawater carbonate concentration on foraminiferal oxygen isotopes. Geochim. Cosmochim. Acta 63, 2001–2007. https://doi.org/10.1016/S0016-7037(99)00091-5

Zhang, L., Delworth, T.L., Zeng, F., 2017. The impact of multidecadal Atlantic meridional overturning circulation variations on the Southern Ocean. Clim. Dyn. 48, 2065–2085. https://doi.org/10.1007/s00382-016-3190-8

Zhou, J., Lau, K.-M., 2001. Principal modes of interannual and decadal variability of summer rainfall over South America. Int. J. Climatol. 21, 1623–1644. https://doi.org/10.1002/joc.700

Apêndice I - Material suplementar I do Capítulo VI

Supporting Information for

Magnitude of the 8.2 ka event freshwater forcing based on stable isotope modelling and comparison to future Greenland melting

Wilton Aguiar[1,*], Katrin J. Meissner[2], Alvaro Montenegro[3], Luciana F. Prado[4,5], Ilana Wainer[4], Anders E. Carlson[6], and Mauricio M. Mata[1]

[1]Laboratório de Estudos dos Oceanos e Clima, Instituto de Oceanografia, Universidade Federal do Rio Grande – FURG. Rio Grande, RS, 96203-900, Brazil.
[2]Climate Change Research Center and ARC Centre of Excellence for Climate Extremes, University of New South Wales, Sydney, Australia.
[3]Atmospheric Sciences Program, Department of Geography, The Ohio State University, Columbus, Ohio.
[4]Instituto Oceanografico, Universidade de Sao Paulo, Sao Paulo, 05508-120, Brazil.
[5]Instituto de Geociências, Universidade de Brasília, Brasília, 70297-400, Brazil.
[6]Oregon Glaciers Institute, Corvallis, OR, USA
*aguiar.wilton@gmail.com

Introduction

This supplementary material shows the location and details of cores used, gives specific information about the simulations, and the climate signals found for the 8.2 ka.

Reconstructed tracers

A total of 35 paleorecords were used to compare the Sea Surface Temperature (SST) and $\delta^{18}O$ with simulations, with five of the cores having high enough resolution to provide time series (Fig S1).

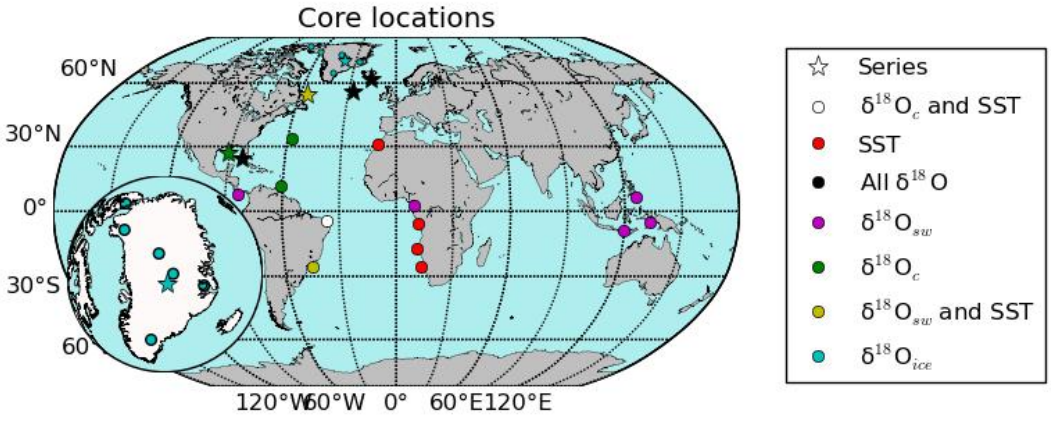

Figure S1. Location of cores used in this study. Circles are cores used in mean anomalies, while stars are cores used for time series analysis. The color legend is for both circles and stars. The cores in black also record SSTs. Drawn by Wilton Aguiar using Python 2.7 (https://www.python.org/download/releases/2.7/)

The mean proxy anomalies in SST, $\delta^{18}O_{sw}$, $\delta^{18}O_c$, $\delta^{18}O_{ice}$ were obtained from Morrill et al., (2013)[1], while the time series used are described in table S1. Mean simulated anomalies are calculated as the mean value of the tracer between 7.9 ka and 8.5 ka for values surpassing 2 standard deviations from the climatological mean for the early-Holocene. The climatological mean here is defined as the mean SST or $\delta^{18}O$ from 9 to 7 ka, with a hiatus between 8.5 ka and 7.9 ka to avoid redundancy. This mean anomaly calculation method is the same applied by Morrill et al. (2013)[1]. There are three species of foraminifera in the cores used to derive the time series: *Globorotalia inflata*, *Globigerina bulloides*, and *Globigerinoides ruber*. Both *Globigerina bulloide*s and *Globigerinoides ruber* occupy the mixed layer (upper 50 m) being appropriate sources of information for SST reconstructions. *Globorotalia inflata* migrates vertically up to 200 m, and calcifies within the seasonal thermocline, thus better representing sub-surface temperatures[2]. SST and $\delta^{18}O$ derived from *G. bulloides* and *G. rube*r were compared with the model SST and $\delta^{18}O$ in the uppermost layer (17 m). *G. inflata* derived SST and $\delta^{18}O$ were compared with the simulated tracers averaged between 82.5 m and 177.5m. $\delta^{18}O_{ice}$ in the Greenland Ice Sheet Project ice core[3] (GISP) was compared to the oxygen isotope ratio in the simulated surface ice at the same location in Greenland. Simulated tracer values from both the mean anomalies and timeseries are taken from the model latitudinal and longitudinal grid points closest to each core location.

University of Victoria Earth System Climate Model (UVic model)

Simulations were performed using the University of Victoria Earth System Climate Model version 2.9, with the addition of oxygen isotopes[11,12]. The UVic model is coupled with seven main components: vegetation, sea ice, sediment, atmosphere, land surface, and ocean components. The ocean component is the Modular Ocean Model Version 2, which has 3.6°x1.8° of longitudinal and latitudinal resolution, and comprises of 19 vertical levels with spacing ranging from 500 m in the deepest levels to 50 m at the surface[4].

Table S1. Time series locations and source cores.

Core	Latitude, Longitude	Source	Variables	Reference
GISP	72.6°N, 38.5°W	Ice	$\delta^{18}O_{ice}$	Grootes et al., (1997)[3]
RAPiD core	62.1°N, 17.8°W	G. *inflata*	$\delta^{18}O_c$ and $\delta^{18}O_{sw}$	Thornalley et al (2009)[5]
		G. *bulloides*	$\delta^{18}O_c$ and $\delta^{18}O_{sw}$	
Gardar Drift	57.4°N,27.9°W	G. *bulloides*	$\delta^{18}O_c$ and $\delta^{18}O_{sw}$	Elmore et al., (2014)[6]
Florida Strait	24.3°N,83.3°W	G. *ruber*	$\delta^{18}O_c$ and $\delta^{18}O_{sw}$	Schmidt et al., (2011)[7]
Gulf of Mexico	26.9°N,91.3°W	*G. ruber*	$\delta^{18}O_c$	Nuernberg et al., (2008)[8]
Labrador Sea	54.6°N,56.2°W	N. *pachyderma*	SST and $\delta^{18}O_{sw}$	Hoffman et al., (2012)[9]

A ten thousand years long equilibrium simulation was performed using 9 ka orbital parameters, i.e. eccentricity=0.0167, obliquity=23.45°, and $[CO_2]$=280 ppmv, and initial pre-industrial $\delta^{18}O_{sw}$ concentration, in order to assure full equilibrium of ocean parameters and circulation. All freshwater forcing simulations depart from the equilibrium run. Finally, the simulated time series of $\delta^{18}O_c$ were converted from $\delta^{18}O_{sw}$ and SST using the equation from Bemis et al., (1998)[10]:

$$\delta^{18}O_c \text{ (ppmv)} = \delta^{18}O_{sw} \text{ (ppmv)} + [T(^{o}C) - 13.2] /4.89$$

Statistics from hybrid experiments

Tables S2 and S3 present the values for the Root Mean Square Error (RMSE) and slopes () for part A and B experiments.

Table S2. Centered Root mean square errors and slopes () for the simulations in part A experiments. RMSEs closest to 0 and slopes closest to 1 are highlighted in red.

Part A experiments			$\delta^{18}O_{sw}$		$\delta^{18}O_c$		$\delta^{18}O_{ice}$		SST	
Short flux (SV)	Long flux (SV)	Simulation	RMSE		RMSE		RMSE		RMSE	
0.13	0.086	FW01	0.19	0.35	0.13	0.02	0.9	1.98	0.74	0.04
0.07		FW02	***0.07***	***1.1***	0.24	-0.26	0.64	4.98	0.70	1.57
0.19		FW03	***0.07***	***1.1***	0.27	-0.59	0.76	6.1	0.76	1.8
0.13	0.066	FW04	0.13	1.2	***0.11***	0.38	0.59	1.55	***0.40***	0.58
0.07		FW05	0.13	1.2	0.12	0.21	0.63	1.95	***0.47***	0.41
0.19		FW06	***0.12***	***1.1***	***0.09***	***0.63***	***0.30***	***0.9***	***0.42***	***0.79***
0.13	0.046	FW07	***0.12***	1.7	***0.11***	***1.1***	0.67	1.65	0.52	0.2
0.07		FW08	***0.12***	***1.1***	0.12	0.16	0.70	2.0	0.61	0.52
0.19		FW09	***0.12***	***1.08***	***0.10***	0.05	0.67	***0.8***	0.51	0.38
0.26	0.046	FW10	0.13	1.15	0.52	0.36	0.75	***1.1***	***0.46***	***1.2***
0.26	0.066	FW11	0.13	1.33	0.60	***1.2***	0.93	1.37	0.56	1.34
0.26	0.086	FW12	0.13	***1.05***	0.68	***1.2***	1.35	1.37	0.60	1.32

Table S3. Centered Root mean square errors and slopes () for the simulations in part B experiments. RMSEs closest to 0 and slopes closest to 1 are highlighted in red.

Part B Experiments			$\delta^{18}O_{sw}$		$\delta^{18}O_c$		$\delta^{18}O_{ice}$		SST	
Short flux (yrs)	Long flux (yrs)	Simulation	RMSE	Slope	RMSE	Slope	RMSE	Slope	RMSE	Slope
130		FW61	***0.12***	***1.1***	***0.09***	***0.63***	***0.30***	***0.9***	***0.42***	***0.79***
90		FW62	0.17	0.55	***0.10***	***0.75***	***0.53***	0.05	***0.46***	**0.67**
50	1000	FW63	***0.12***	***1.06***	***0.10***	0.43	***0.55***	1.41	***0.46***	**0.67**
130		FW64	0.17	0.73	***0.10***	0.51	***0.48***	***0.92***	***0.39***	***0.96***
90		FW65	0.20	0.56	0.14	0.26	0.69	2.51	***0.36***	***0.90***
50	600	FW66	0.21	0.37	***0.10***	0.17	0.82	2.46	***0.42***	0.52
130		FW67	0.19	0.82	0.13	0.36	***0.54***	2.28	***0.40***	01.03
90		FW68	0.20	0.52	0.14	0.10	0.69	2.25	***0.39***	0.58
50		FW69	0.21	0.17	***0.10***	0.05	0.92	1.4	0.60	0.21
	200	FW610	0.15	1.22	0.87	1.78	1.02	1.6	0.99	1.94
	600	FW611	0.16	1.35	0.98	02.03	1.00	1.52	1.18	2.15
300	1000	FW612	0.14	1.54	0.85	1.43	0.94	1.2	0.87	1.73

Freshwater Budget in simulation FW61

The anomalies in precipitation and river discharge for the simulation FW61 exhibit only negative values between 8.4 ka and 8.2 ka (Fig S2). The balance between precipitation, evaporation, and runoff over the North Atlantic (north of 30°N - Fig S2) yields a maximum freshwater anomaly of -0.015 Sv, and is thus six times lower than the low background flux (0.066 Sv) in FW61. Hence, no significant volume of freshwater is added or removed to/from the North Atlantic Ocean through the prognostic freshwater

budget in the model (i.e. simulated precipitation + simulated runoff - simulated evaporation), when compared with the forced freshwater anomalies (See Methods in the main manuscript).

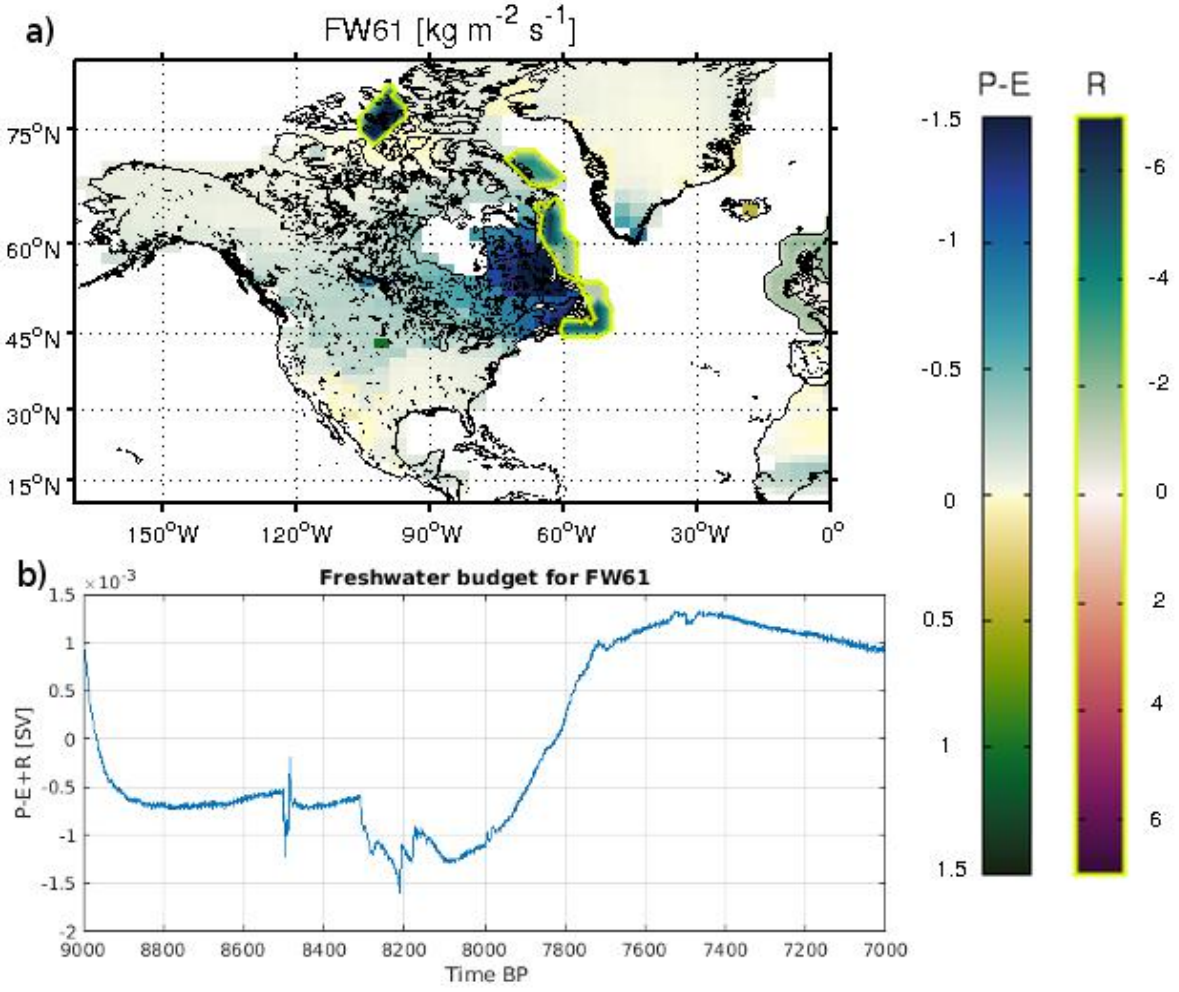

Figure S2. The North Atlantic freshwater budget in the North Atlantic and over North America. (a) The contour of anomalies in precipitation minus evaporation (P-E) and continental runoff discharge (R) in kg m^{-2} s^{-1}, calculated as the difference of the mean variable between 8.4 ka - 8.2 ka and between 9 ka - 7 ka. The colormaps inside the yellow contour represent the anomalies in river discharge, while the colormaps outside the yellow contours are for anomalies in P-E. (b) Anomalies of the freshwater budget in the North Atlantic (north of 30ºN: precipitation - evaporation + river runoff) in Sv, relative to the mean freshwater budget from 9ka - 7ka. Drawn by Wilton Aguiar using Matlab R2013a (https://www.mathworks.com/products/matlab.html)

Apêndice II - Material suplementar II do Capítulo VI

Below are the results from the Diebold-Mariano test in percentage of accepantance of H0 (%) for the part B experiments. Table 1 is for the $\delta^{18}O_c$ while 2 is for $\delta^{18}O_{sw.}$

Table 1. Confidence levels for accepting the h0 hypothesis that models have the same error - $\delta^{18}O_c$

	61	62	63	64	65	66	67	6	69	610	611	6	Mean %
61	x	10	90	60	5	5	5	5	5	90	15	1	
62	10	x	25	60	5	5	5	5	5	30	90	5	
63	90	25	x	45	20	15	20	1	15	80	25	1	
64	60	60	45	x	30	25	25	2	25	60	70	5	
65	5	5	20	30	x	15	15	1	15	10	1	1	
66	5	5	15	25	15	x	20	2	35	5	1	1	
67	5	5	20	25	15	20	x	1	15	10	1	1	
68	5	5	15	25	15	25	15	x	35	5	1	1	
69	5	5	15	25	15	35	15	3	x	5	1	1	
610	90	30	80	60	10	5	10	5	5	x	1	1	
611	15	90	25	70	1	1	1	1	1	1	x	1	
612	1	5	1	5	1	1	1	1	1	1	1	x	

19

Table 2. Confidence levels for accepting the h0 hypothesis that models have the same error - $\delta^{18}O_{sw}$

	61	62	63	64	65	66	67	68	69	610	611	612	
61	x	20	15	15	1	1	15	1	5	10	5	5	Mean %
62	20	x	20	20	5	5	5	5	10	10	5	5	
63	15	20	x	20	1	1	35	1	5	10	5	5	
64	15	20	20	x	10	10	10	10	10	10	5	5	
65	1	5	1	10	x	20	20	40	45	5	5	5	
66	1	5	1	10	20	x	20	45	25	5	5	5	
67	15	5	35	10	20	20	x	15	25	5	5	5	
68	1	5	1	10	40	45	15	x	80	5	5	5	
69	5	10	5	10	45	25	25	80	x	5	5	5	
610	10	10	10	10	5	5	5	5	5	x	5	5	
611	5	5	5	5	5	5	5	5	5	5	x	5	
612	5	5	5	5	5	5	5	5	5	5	5	x	

12

Apêndice III - Material suplementar I do Capítulo VII

Supplementary material to the paper *Freshwater forcing control on early-Holocene South American Monsoon*

Wilton Aguiar[a], Luciana Prado[b], Ilana Wainer[c], Zhengyu Liu[d], Alvaro Montenegro[d], Katrin J. Meissner[e], Mauricio M. Mata[a]

[a] *Laboratório de Estudos dos Oceanos e Clima, Instituto de Oceanografia, Universidade Federal do Rio Grande – FURG. Rio Grande, RS, 96203-900, Brazil*
[b] *Instituto de Geociencias,Universidade de Brasilia, Campus Darcy Ribeiro, Brasilia, Distrito Federal, 70910-900, Brazil*
[c] *Instituto Oceanografico da Universidade de Sao Paulo, Sao Paulo, 05508-120, Brazil*
[d] *Atmospheric Sciences Program, Department of Geography, The Ohio State University, Columbus, Ohio*
[e] *Climate Change Research Center, University of New South Wales, Sydney, Australia*

Appendix A. Derivation of the wind-driven isothermal depth

Consider a 1.5 layer model with a moving surface layer with density ρ_1 and width h_1 and a static deep layer with density ρ_2 and width h_2. The pressure over the isotherm in the boundary between layers is $P = \rho_0 \lambda h_1$ where $\lambda = (\rho_2 - \rho_1)/\rho_0$ and ρ_0 is a reference density. The vertical velocity at the surface is $w_0 = 0$. With the pressure equation and the vertical velocity conditions, the geostrophic system becomes:

$$v = (\lambda/f)\delta h_1/\delta x \tag{A.1}$$

$$u = -(\lambda/f)\delta h_1/\delta y \tag{A.2}$$

Email address: aguiar.wilton@gmail.com (Wilton Aguiar)

$$\int_z^0 \delta u dz/\delta x + \int_z^0 \delta v dz/\delta y = -w_z \tag{A.3}$$

The solution of equations A.1-3 gives:

$$h^2 = 2f^2 w_z (x - x_e)/\beta\lambda + H^2 \tag{A.4}$$

where $H^2 = h^2(x_e)$ is the isothermal depth in the eastern boundary. This value was measured in the easternmost South Atlantic cell of the model and is zonally constant, so it does not affect the isotherm inclination along the Atlantic. The parameter $(x - x_e)$ is the distance from the eastern boundary. The Ekman pumping was obtained by:

$$w_e = \nabla \times \tau/\rho_0 f + \beta\tau_x/\rho_0 f^2 \tag{A.5}$$

where τ and τ_x are the total and zonal wind stresses, respectively. The variable modulating A.4 is then the wind stress τ by changing the Ekman pumping.

Appendix B. UVic Simulation

This appendix presents additional information on the UVic model simulation. The convection depth in the model is shown in Fig B.1, and the AABW and NADW strengths in all the simulations are presented in Fig B.2.

Appendix C. South American Monsoons System and the South Atlantic Subtropical Dipole

The South American Monsoon System (SAMS) is a regime that marks an increase in precipitation over the Intertropical Convergence zone (ITCZ) and the South Atlantic Convergence Zone (SACZ) (Figure C.3). The ITCZ and SACZ are features of the SAMS. The ITCZ is a permanent feature with varying locations in the equatorial area due to warmer SSTs that follow the warmer hemisphere, while the SACZ is a summer feature characterized by moisture convergence from the Amazon basin to the Southeastern Atlantic. Its variability is one of the main controllers of precipitation over South America from the seasonal to interannual scales (Vera et al., 2006). The monsoonal

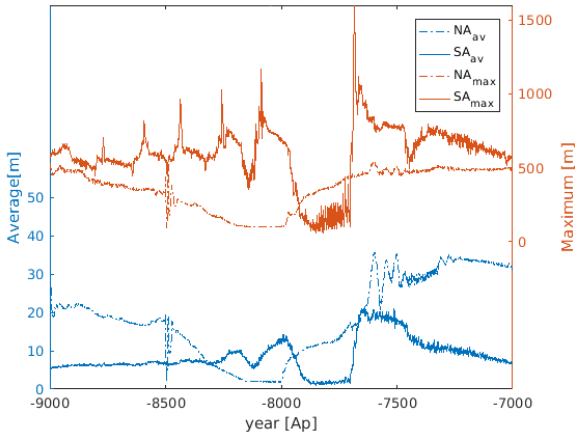

Figure B.1: Mean (—) and maximum (—) convection depth in the UVic freshwater forcing simulation over the North Atlantic (dashed line) and Southern Ocean within 60^{o}W and 20^{o}E (full line).

regime emerges from the seasonal southward anomaly in the tropical wind circulation, which then transports moisture in the southeast direction, most specifically towards northeastern Brazil. Moisture convergence occurs when the equatorial trade winds transport moisture from the ocean towards the Amazon basin. The onset of the SAMS regime starts in austral spring with the increase in atmospheric convection over the Amazon basin and expansion of the convection band towards northern Brazil (Nogués-Paegle and Mo, 1997). Although the SAMS precipitation signal is seasonal, interannual and decadal, strength variations are documented. A first source of inter-annual variability is the El Niño–Southern Oscillation (ENSO): Pacific SST anomalies induce anomalies in Walker cell circulation that cause upwards air motion over northeastern Brazil, enhancing precipitation (Ropelewski and Halpert, 1989). Second, the South Atlantic Subtropical Dipole (SASD) shifts the latitudinal band of moisture delivery to South America, enhancing or diminishing the precipitation strength in the northeastern region of the SAMS (Wainer et al., 2014). Anomalies in the wind speed can cause SST anomalies in the tropical South Atlantic of up to 0.3^{o}C, and periods with positive SST anomalies are then associated with intensified precipitation over the SACZ (Robertson and Mechoso, 2000). Bombardi et al. (2014) explain that tropical SST warming in the negative SASD phase displaces the SACZ towards the equator, increasing the convective precipitation in the coastal northeast

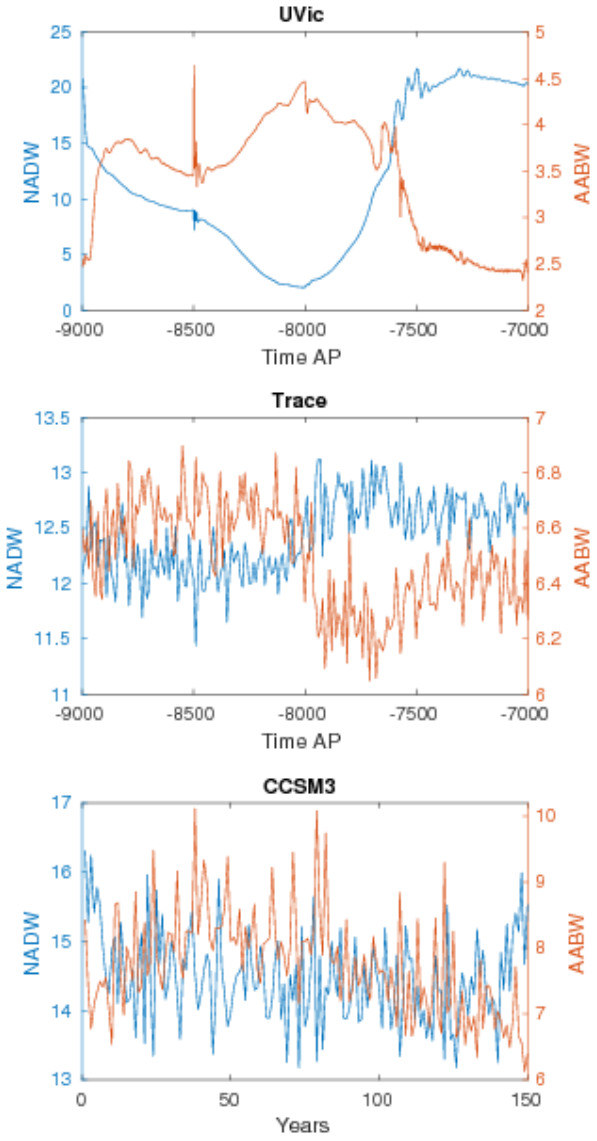

Figure B.2: North Atlantic Deep Water (NADW —) and Antarctic Bottom Water (AABW —) time series. NADW (AABW) strength was measured by the absolute maximum (minimum) overturning streamfunction in the North Atlantic (Southern Ocean).

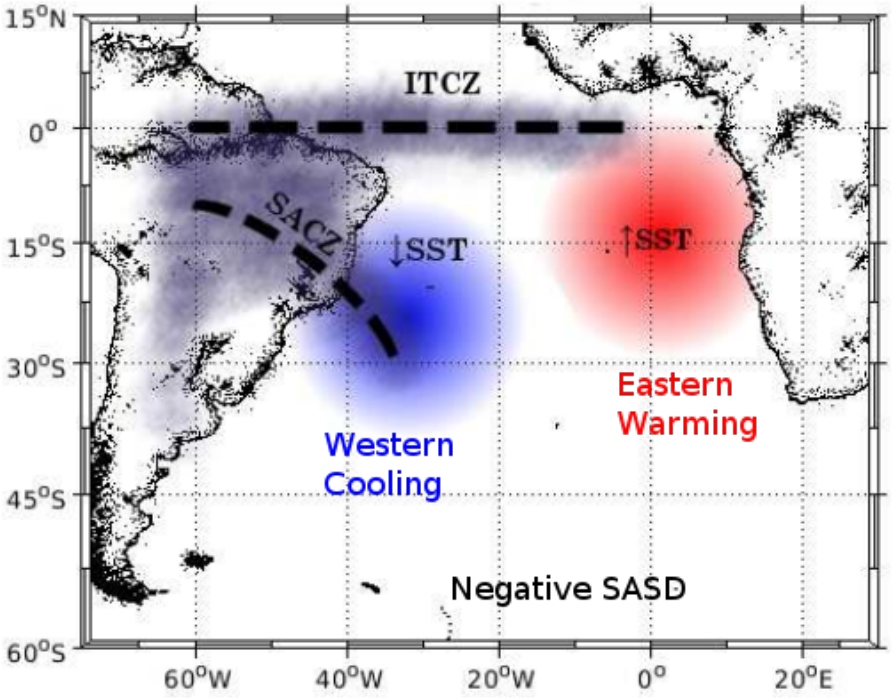

Figure C.3: Main patterns in the SASD and SAMS. The red and blue circles show regions of positive and negative sea surface temperature anomalies during the negative SASD phase. The smoky region shows the area affected by the SAMS. Dashed lines mark the Intertropical Convergence Zone (ITCZ) and the South Atlantic Convergence Zone (SACZ).

South America. This effect is complemented by stronger tropical moisture delivery to the atmosphere due to SST warming in negative SASD events, increasing moisture saturation in the tropics and precipitation (Wainer et al., 2014).

The SASD is a dipole-like pattern of SST anomalies in the South Atlantic, and in its negative (positive) phase, it exhibits positive (negative) anomalies in the northeast South Atlantic and the opposite in the southwest South Atlantic (Venegas et al., 1997). SASD pole anomalies start to develop during austral spring and reach their maximum values by the summer in an analogous evolution to the SAMS. In the present day, explanations for the dipole establishment lie in the southward movement of the subtropical high, changing the latent heat flux (Morioka et al., 2011), and Ekman heat

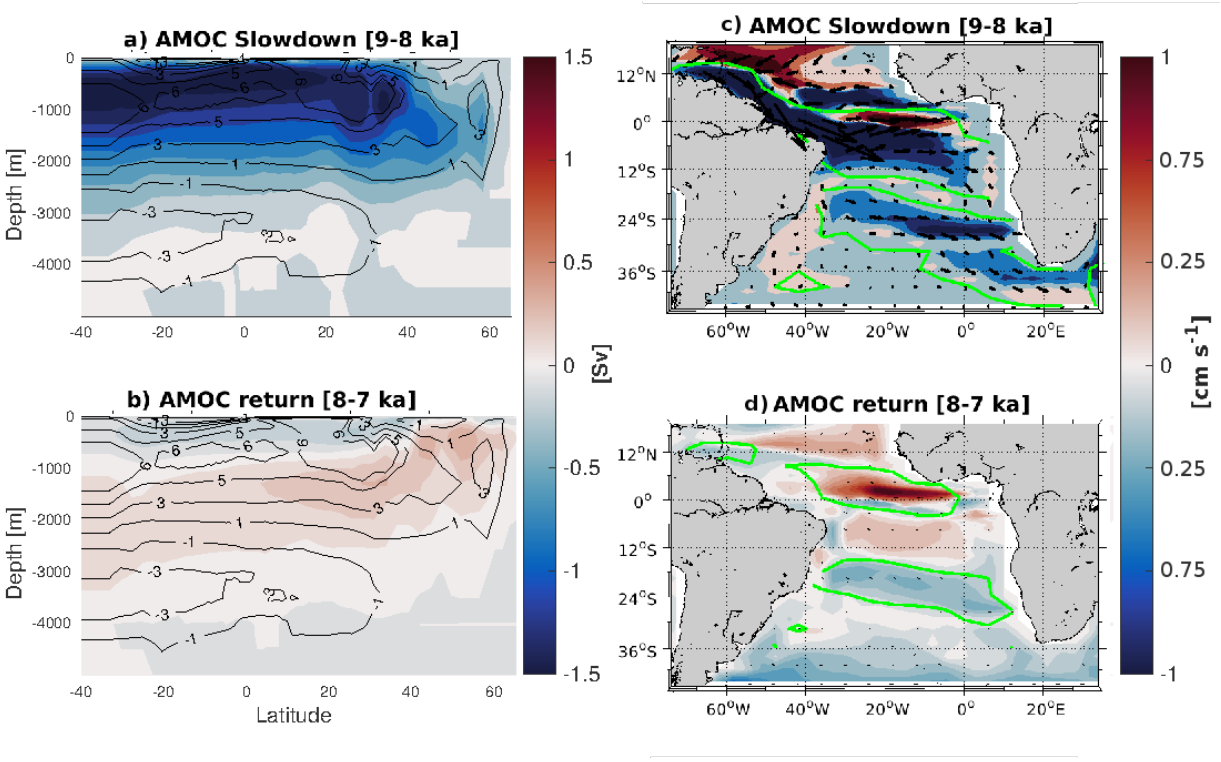

Figure C.4: Structure of the AMOC (a-b) and surface velocities (c-d) in the slowdown (a,c) and resumption phases (b,d) for the TraCE simulation. Contour values represent the overturning prior to the freshwater addition in TraCE (9.1 ka,a-b). Positive values denote clockwise circulation and negative anti-clockwise. Filled contours in a and b are the difference between mean overturning in the freshwater forcing period (9-8 ka) and 9.1 ka (a), and between the resumption phase (8-7 ka) and 9.1 ka (b). Arrows (colors) in c-d are the surface velocity anomalies vectors (magnitudes) in the slowdown and return phase. Surface circulation anomalies are relative to 9.1 ka mean circulation. Green contours marks regions with velocity anomalies bigger than 0.1 cm s^{-1}.

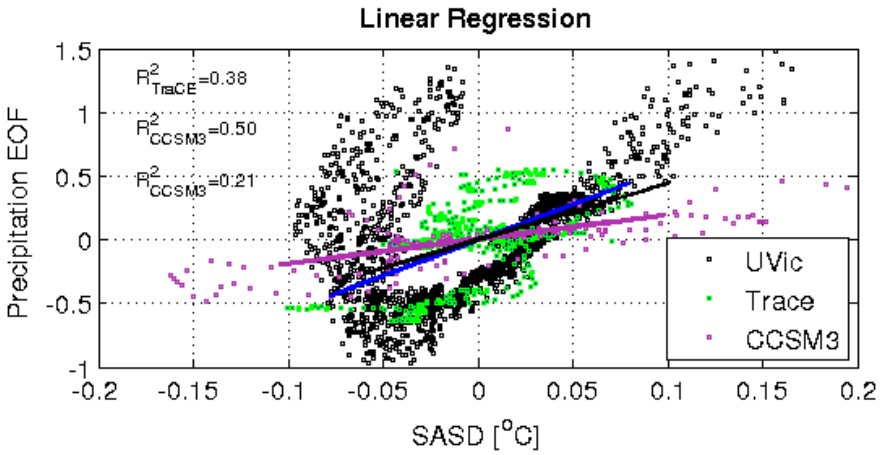

Figure C.5: Linear regression between the SAMS precipitation EOF and the SASD index in all three models. Determination coefficient for each simulation are on the left-side of the plot.

transport (Sterl and Hazeleger, 2003), with a higher contribution from the first.

Appendix D. Overturning Structure

The structure of the AMOC in the TraCE simulation shows that the upper cell of the overturning weakens by1.5 Sv. While the overturning slows, the zonal surface ocean velocities decrease in the South Atlantic (Fig C4,c). In the resumption phase, the overturning in the upper cell intensifies above 9.1 ka values and the NADW deepens below 2500 m (Fig C4,b - upper 1000-3000 m).

References

Bombardi, R., Carvalho, L., Jones, C., 2014. Simulating the influence of the South Atlantic dipole on the South Atlantic convergence zone during neutral ENSO. Theoretical and Applied Climatology doi:10.1007/s00704-013-1056-0.

Morioka, Y., Tozuka, T., Yamagata, T., 2011. On the Growth and Decay of the Subtropical Dipole Mode in the South Atlantic. Journal of Climate 24, 5538–5554. URL: https://doi.org/10.1175/2011JCLI4010.1, doi:10.1175/2011JCLI4010.1.